UNIVERSITY
OF TASMANIA

PRO-ACTIVE ACOUSTIC NOISE REDUCTION FOR MAGNETIC RESONANCE IMAGING SCANNERS

by

James M Jackson, BSc (Hons)

School of Mathematics & Physics

Submitted in fulfilment of the requirements for the
Degree of Doctor of Philosophy.

University of Tasmania, November 2012.

I declare that this thesis contains no material which has been accepted for a degree or diploma by the University or any other institution, except by way of background information and duly acknowledged in the thesis, and that, to the best of my knowledge and belief, this thesis contains no material previously published or written by another person, except where due acknowledgement is made in the text of the thesis.

Signed: _____
James M Jackson

Date: 8/11/2012

Signed: _____
James M Jackson

Date: 8/11/2012

Abstract

Large acoustic noise generated by magnetic resonance imaging (MRI) scanners pose significant problems for a patient undergoing a scan, in addition to attending medical staff. A heightened sense of anxiety, difficulty communicating with medical staff, and mild irritation through to acute discomfort are all results of the large noise amplitude produced during the scanning process.

Gradient coils are a component of MRI hardware that have been found to be the major contributor of acoustic noise and are thus the subject of this thesis. A gradient coil is required to produce a homogeneous linear field to excite nuclei in a predictable manner so that clear images can be obtained. A feature of gradient coils is that they must be switched on and off repeatedly during the imaging process. This switching generates large Lorentz forces on the chamber, which causes the chamber to deform and promotes a pressure wave inside the chamber that can be heard as acoustic noise. The problem becomes one of designing current winding patterns on the gradient coil that produce a specified linear field and have a reduced simulated acoustic noise output. This problem is studied in detail and is accomplished using a Tikhonov regularisation process.

This thesis looks directly at theoretical methods to actively reduce simulated acoustic noise during the MRI scanning process. Pro-active noise reduction, in this work, is achieved by reducing the deflection of the gradient coil, which leads to the design of quiet gradient coils. Beginning with a relatively simple one dimensional radial coil deformation model and requiring a high level of linearity of the gradient field, designs for the current windings on the gradient coils are produced. In this first model a comparatively small reduction of 0.6 dB was attained; however, previous work was extended to account for realistic switching sequences. Next, a more sophisticated three dimensional deflection model was considered,

which produced a similar small level of noise reduction, but nonetheless substantial insight into the physical process behind the generation of noise was obtained. Finally, a robust technique for designing very quiet gradient coils, reducing the noise by 49 dB, was achieved by abandoning the requirement that the gradient coil produce a homogeneous linear field. It is only through sacrificing field linearity that such significant gains become achievable. Typically a severely nonlinear gradient field would result in unusable images. However, through the use of a phantom image technique described later, high quality images are theoretically recoverable.

Acknowledgments

First and foremost I would like to thank my primary supervisor Dr Michael Brideson. His great personality, continued support, mathematical expertise, volleyball skills and guidance throughout my studies at UTas have made him a pleasure to work with. Another big thank you must also go to my co-supervisor, Professor Larry Forbes, whose endless passion and enthusiasm has been inspiring for me to learn from. Together their advice, constructive criticism and ongoing efforts have made this long privileged journey a thoroughly enjoyable one.

Next I must thank Kain Chambers, my office mate for the past few years. He has ensured it has been an entertaining stint if not always a productive one. I would also like to thank all the remaining staff and postgraduate students in the School of Maths and Physics and in particular Karen Bradford and Dr Kym Hill for all their assistance. The atmosphere created by the friendly staff and students makes the maths and physics department an inspiring place to work.

Also, I would like to thank the examiners for their constructive comments. This thesis has been enhanced by the added content due to their suggested alterations.

Finally, I would like to thank my family, girlfriend and friends. Their love and support has kept me on track and made the whole experience not only pleasurable but absolutely fantastic.

I have no idea what the future holds but the lessons I have learnt along the way, not only about science and research but also from my amazing Sophy have given me a strong foundation to fall upon. I'm thoroughly glad I undertook this enriching, challenging and at times gruelling program.

I wish to dedicate this work to the memory of my father, Peter Jackson, and my great friend, Andrew Conlan.

List of Publications

Throughout my doctoral studies I have produced three papers in different stages of production.

Tikhonov Regularization Approach to Acoustic Noise Reduction in an Asymmetric, Self-Shielded MRI Gradient Coil
By James Jackson, Michael Brideson, Larry Forbes and Stuart Crozier
(Published)

An Extended Deformation Model and Pressure Wave Analysis for a Gradient Coil in an MRI Application
By James Jackson, Michael Brideson, Larry Forbes and Stuart Crozier
(Submitted)

Could Image Processing Enable Reduced Acoustic Noise during MRI Scans?
By James Jackson, Larry Forbes, Peter While and Michael Brideson
(Published)

Statement of Co-Authorship

The following people and institutions contributed to the publication of the work undertaken as part of this thesis:

Paper 1: Tikhonov Regularization Approach to Acoustic Noise Reduction in an Asymmetric, Self-Shielded MRI Gradient Coil
By James Jackson (60%), Michael Brideson (25%), Larry Forbes (14%) and Stuart Crozier (1%)

Paper 2: An Extended Deformation Model and Pressure Wave Analysis for a Gradient Coil in an MRI Application
By James Jackson (65%), Michael Brideson (25%), Larry Forbes (9%) and Stuart Crozier (1%)

Paper 3: Could Image Processing Enable Reduced Acoustic Noise during MRI Scans?
By James Jackson (50%), Larry Forbes (30%), Peter While (15%) and Michael Brideson (5%)

Details of the Authors roles:

Michael Brideson: contributed with mathematical assistance, and refinement and presentation of manuscripts
Larry Forbes: contributed with motivation and formulation of ideas
Peter While: contributed with specialised advice and assistance in coding
Stuart Crozier: contributed with general guidance

We the under signed agree with the above stated "proportion of work undertaken" for each of the above published (or submitted) peer-reviewed manuscripts contributing to this thesis:

Signed: _____ _____

Dr Michael Brideson
Supervisor
School of Mathematics
& Physics
University of Tasmania

Prof John Dickey
Head of School
School of Mathematics
& Physics
University of Tasmania

Date: Nov 8, 2012

TABLE OF CONTENTS

List of Symbols

a	primary coil radius
b	shield coil radius
L	length of coil (subject to context)
c_1	larger of the interior target radii
c_2	smaller of the interior target radii
c_3	external target radii to force shielding
h	coil thickness
r_M	midpoint coil radius
p, q	dimensionless constants that specify the asymmetry of the target field
E	Young's modulus of the coil
ν	Poisson's ratio of the coil
G	Shear modulus of the coil
Λ	Lamé coefficient of the coil
ρ_c	density of the coil (copper)
$\mathbf{B}$	magnetic induction field
$\mathbf{H}$	magnetic field strength
B_{Z0}	primary magnet field strength
B_{grad}	gradient field strength (mT/m)
B_{TF}, H_{TF}	'target field' note: it is always in the z-component of the field
^{P}	(superscript) denotes primary coil
^{S}	(superscript) denotes shield coil
Ψ	stream function
j_θ	azimuthal current density
j_z	axial current density
ρ_r	resistivity of coil

f_s	switching function
ω	switching frequency
W_0, W_k, X_k	known Fourier coefficients of switching function
τ	'charge up' time of switching function (suject to context)
T	period of switching function
t_1	half time spent 'on' of switching function
λ	regularization parameter
λ_U	coil deflection regularization parameter
λ_P	primary winding smoothing regularization parameter
λ_S	shield winding smoothing regularization parameter
λ_{Power}	power regularization parameter
u_r, u_θ, u_z	coil displacement/deflection components in respective directions
v_θ, v_z	coil velocity components in respective directions
p_{A1}	pressure perturbation
ρ_{A0}	density of air
p_{ref}	reference air pressure
c_{A0}	speed of sound
$V(t)$	flow rate out of coil
ω_L	Larmor frequency
$\boldsymbol{\mu}$	magnetic moment
$\mathbf{L}$	angular momentum
τ	torque (subject to context)
γ	gyromagnetic radius
G_s, G_ϕ, G_f	gradient pulse sequences
β	figure of merit (for gradient coils)
δ	gradient field homogeneity
η	gradient coil efficiency
L	gradient coil inductance (subject to context)
∇^2	Laplacian operator
$\nabla\cdot$	divergence operator
$\nabla\times$	curl operator
$\ell\{\}$	Laplace Transform operator

Chapter 1

Introduction, Background, and Theory

1.1 Introduction

Magnetic resonance imaging (MRI) is a widely employed technique in the fields of spectroscopy and medical imaging. Using an MRI scanner is considered to be the leading way to image soft tissue in the human body due to its high sensitivity to several tissue parameters. Other advantages of using MR imaging are that it is non-invasive and uses non-harmful non-ionising radiation, unlike x-rays. The cost involved in a typical MRI scanner can be upwards of US $1 million, with maintenance costing several hundred thousand dollars a year. A need to have efficient and effective scanners is enhanced by these economic factors and other medical and comfort issues discussed in detail later.

1.2 A Brief History of MRI

A summary of the history of the physics, construction and testing which led to the development of the modern MRI scanner is presented. This section is only intended to account for a few of the milestones and accomplishments involved. A significantly more complete and comprehensive discussion can be found in the Encyclopaedia of Nuclear Magnetic Resonance by Grant *et al.* [43]. However, the major developments are shown to acknowledge the achievements of those involved and to provide a historical context for this thesis.

Central to the phenomenon of relaxation is the concept of 'spin' which was first proposed by Pauli in 1925 (see Eisberg and Resnick [25]). He later formulated the mathematical properties of spin and Dirac incorporated these into his quantum mechanical description of the atom; see Thaller [102]. Particles with spin can possess a magnetic dipole moment; the moment will precess with a frequency, ω_L, proportional to the strength of an external magnetic field. This relationship is readily attributed to Larmor and is the fundamental concept behind spatial encoding in MRI. Interestingly, Larmor used the precessional frequency as the basis for a reference frame transformation [67] to explain the Zeeman effect. In so doing, Larmor postulated that Zeeman's results and J. J. Thomson's cathode ray observations were both due to electrons, an as yet formally unidentified particle. In MRI the Larmor relation is usually spoken of in conjunction with protons, the discovery of which came twenty years after Larmor's proposition on electron precession.

Apart from the quantum mechanical description of the atom, the development of MRI would not have proceeded without magnets capable of producing appropriate fields. Early magnets had stray fields and unwanted heating among other

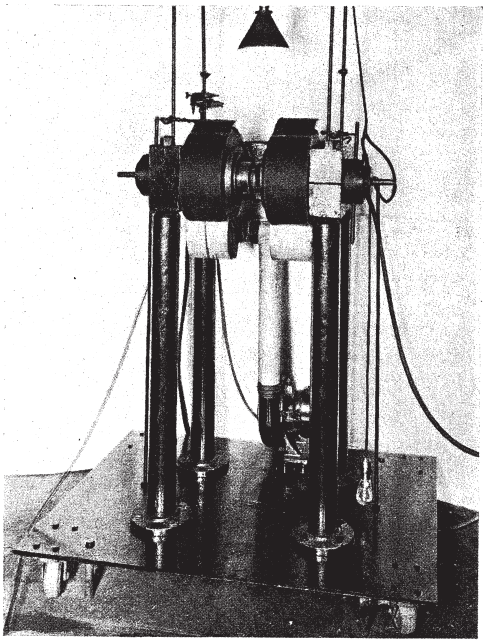

Figure 1.1: A photo of an early magnet designed by Shaw in 1931.

problems. Shaw [99] (with aid in design and construction from Phipps) in 1931 built a magnet which addressed these issues. The magnet pictured in figure 1.1 was carefully constructed and designed to produce significant improvements on other magnets of its time that were used for analysing magnetic properties of atoms. Improvements in field homogeneities came steadily from simple coil geometries. McKeehan (see [81, 82]) summarised a variety of commonly known wire patterns which produce uniform magnetic fields. He credits Braunbek as the first person to expand most effectively the Helmholtz coil to multiple loops, using only 3 loop pairs to attain a field homogeneous through to the 12th order.

In 1938, Rabi *et al.* [95] detailed the apparatus used by his group to obtain the first NMR signals from a molecular beam containing isotopes of Lithium. The apparatus was composed of magnets and coils producing three types of magnetic fields: (1) a homogeneous static field, (2) a gradient field, and (3) a radiofrequency (rf) oscillating field. Although they were both known to Rabi, the groups of Pur-

cell and Bloch worked independently on the development of NMR, approaching it from two entirely different perspectives. Purcell's group considered magnetic resonance in terms of quantum transitions [94] whilst Bloch's group saw magnetic resonance as a reorientation of magnetic moments with respect to an external magnetic field [8]. Both men had their research interrupted by war effort obligations but it also influenced their coming research. Post-war, both groups removed the molecular beam and turned their attention to discovering magnetic resonance in bulk matter. It wasn't until Bloch and Purcell met in 1946 that both groups realised that despite their different perspectives, they were exploring the same phenomenon; see Rigden [96]. Together, in 1952 they shared the Nobel Prize in physics for their efforts.

Magnetic resonance studies quickly gained in popularity in many Physics laboratories with research groups exploring the phenomenon in a variety of bulk matter. Most groups adopted the combination of magnetic fields used by the Purcell and Bloch groups but the delivery of the fields varied among groups. For all groups though, to maximise the signal-to-noise ratio, magnetic field accuracy was paramount. In a 1968 review article on limitations in magnetic resonance, Hill and Richards [51] indicated that field homogeneity of the order of a few parts in 10^9 - 10^{10} were required for a static field of about 2 T. Traditionally, electromagnets and permanent magnets were used to produce fields up to 2.5 T; for fields above 2.5 T newly introduced superconducting electromagnets were favoured. Homogeneity was primarily controlled with high quality geometrical design and construction. In 1951, Garrett [36] presented a technique for designing coil systems based on zonal harmonics and composed of circular filaments, cylindrical or plane circular current sheets, and thick solenoids of rectangular or notched section. Such coil designs could be used to produce constant fields and gradient fields. Also very

useful were field-correcting coils, such as the planar windings described by Golay [39] and patented by Anderson [3], Nelson [90], and Golay [40, 41]. Many of these coils were designed to sit on the magnet poles and some were designed to excite a particular spherically shaped harmonic field.

In the 1950s, the NMR research of Carr - a doctoral student of Purcell - enabled larger samples, improved signal-to-noise ratio, and a new method for measuring relaxation times [16, 17]; this work is often credited as producing the first MR image in one dimension. Despite this, research continued into improvements in NMR techniques and it was not until the late 1960s that MR imaging research became prominent. Damadian, in 1970, was the first to conduct experiments involving relaxation times using human tissue. The experiments showed that using MRI was particularly useful for distinguishing between normal and cancerous tissue. In 1972 Damadian [21] patented the first MRI scanner used for medical purposes. The scanner comprised an arrangement of magnets (along with other hardware) sufficiently homogeneous at one point in space to image a human chest in 4.5 hours to within 1 cm resolution. He named this technique FONAR, for field focusing NMR. Damadian also founded the FONAR Corporation in 1978 and the company produced the first commercial scanner in 1980.

Earlier on, in 1973, Lauterbur [68], and Mansfield and Grannell [78] independently showed that the application of MRI in medicine was capable of producing good quality two dimensional images of water filled structures, e.g. the human body, and MRI began (see Filler [27]) in its modern sense.

In 1977, Garroway, Grannell and Mansfield [37] introduced a slice selection imaging technique, in which one plane could be 'scanned' at a time to build an image. Following them, Ernst [26] in 1977 developed the 'two dimensional Fourier Transform' (2DFT) imaging technique (discussed later), where the sample is both phase

and frequency encoded. He named this process 'NMR Fourier Zeugmatography' and it now forms the basis of all modern imaging techniques.

The process which is commonly called MRI today had several different names in its founding years. Respective researchers called the process: spin mapping, spin imaging, magnetic resonance tomography, NMR Fourier zeugmatography and NMR imaging. To avoid the perception of using harmful radiation, 'nuclear' was dropped from the title and 'magnetic resonance imaging' become the accepted term.

With the invention of superconducting magnets, advanced engineering techniques and the application of sophisticated mathematical techniques, MRI scanners today achieve much better resolution and faster scanning times than their earlier counterparts. Many other design issues have now been considered, mostly concerning patient safety and comfort, but the perfect MRI scanner has not yet been developed.

1.3 The Physics behind MRI

This thesis primarily concentrates on the design of gradient coils (a component of MRI hardware to be discussed later). To put the design issues involved with gradient coils into context it is important to have a basic knowledge of how an MR image is formed. A more comprehensive derivation of the physics behind MRI can be found in several texts including Kuperman [64], Haacke *et al.* [45], Hornak [52], NessAiver [91], Vlaardingerbroek and den Boer [109], and Jin [60].

The properties of subatomic particles are fundamentally governed by quantum mechanics. However, a semi-classical model presented by Bloch (which is consid-

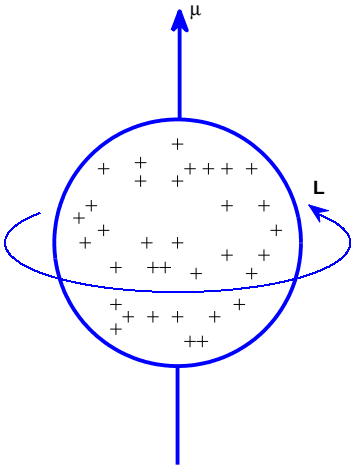

Figure 1.2: Each proton has an associated magnetic dipole field, $\boldsymbol{\mu}$, generated from its charge rotating with angular momentum $\mathbf{L}$.

erably simpler to understand) gives an adequate description of the phenomena involved with NMR.

1.3.1 Spin

All subatomic particles possess a quantum mechanical property called spin. A proton, for example, can be considered as a sphere with positive charge distributed throughout its volume and rotating about its own axis at high speed. The charge distribution inside the proton leads to a net flow of charge about its rotating axis, thus producing a small magnetic field. This magnetic field is termed the magnetic dipole moment, $\boldsymbol{\mu}$, of the proton. The rotating mass also leads to an angular momentum $\mathbf{L}$. Figure 1.2 depicts this classical physics model of the proton.

A nucleus constitutes a collection of protons and neutrons bound together forming a rotating system. This rotating system therefore has a net angular momentum

and a net magnetic moment, $\boldsymbol{\mu}$, which is the sum of all magnetic dipoles from each particle in the nucleus. The relationship between these two properties is given by

$$\boldsymbol{\mu} = \gamma \mathbf{L}, \tag{1.1}$$

where γ is the gyromagnetic ratio and is determined empirically; see Gadian [35]. The gyromagnetic ratio is specific to each nucleus and is a measure of its NMR sensitivity. For Hydrogen (^1H) the gyromagnetic ratio is experimentally determined to be $\gamma/2\pi = 42.58$ MHz/T. This relatively high γ value for ^1H is due in part to the the ^1H nucleus being 'shielded' by only one electron. Hydrogen is particularly useful for clinical MRI due to the large content of water (H_2O) and fat ($-CH_2-$) in the human body and its high NMR sensitivity.

A pair of protons considered as an isolated system must satisfy a non-degenerate state as described by Pauli (see Eisberg and Resnick [25]). This means one proton will be spin 'up' and the other will be spin 'down'. The terms 'up' and 'down' are not literal terms but terms that denote opposite states. Only certain nuclei posses a non-zero magnetic moment and these nuclei are characterised by having an odd number of protons or neutrons (or both). One unpaired proton/neutron will always be present in such nuclei, which leads to an unbalanced dipole moment. It is solely these nuclei that are susceptible to NMR effects.

1.3.2 NMR Response of Hydrogen

The response of a hydrogen atom in the presence of a magnetic field can be modelled by considering the moment of the nucleus. In the presence of an external magnetic field (typically taken to align in the z-direction and denoted by $\mathbf{B}_{Z0}$) a

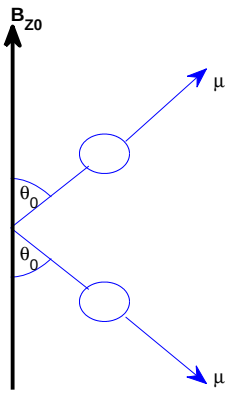

Figure 1.3: A proton's magnetic moment aligns in one of two states in the presence of an external magnetic field.

proton's magnetic moment will precess at an angle θ_0 to the magnetic field. The two states a proton can attain correspond to the magnetic moment's z-component aligning either parallel (in the $+z$-direction) or anti-parallel (in the $-z$-direction) to the external field; see figure 1.3. Importantly, a proton with its z-component of the magnetic moment aligning parallel to the external field is in a lower energy state. The difference in energy between the lower and higher energy states is proportional to the strength of the external field and is given by

$$\Delta E = 2\mu_z B_{Z0}.$$

This is known as the Zeeman effect and can be seen in figure 1.4.

When a proton flips between energy states it emits or absorbs a photon with energy equal to the difference between the two states. The emitted/absorbed photon is an electromagnetic (EM) wave of determinable frequency, ν. Bohr was the first to describe the relation between the frequency of the absorbed/emitted photon

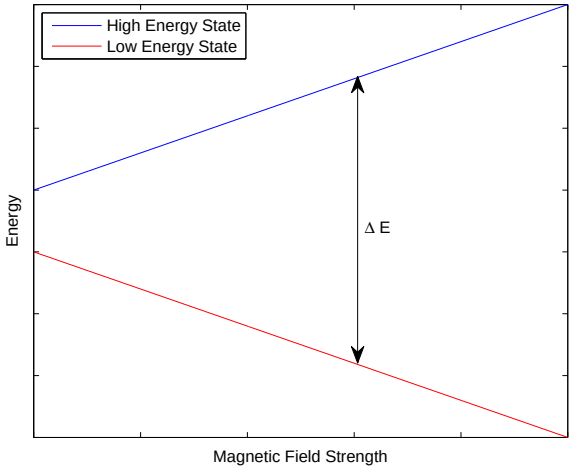

Figure 1.4: The Zeeman effect describes a growing energy gap between parallel and anti-parallel states for a larger applied magnetic field.

and the magnetic field strength; see Levitt [69]. Through the Bohr relation,

$$\nu = \frac{2\mu_z}{h} B_{Z0},$$

we see that $2\mu_z/h$ is constant for a particular nuclei, and therefore the frequency of the exchanged photon is proportional only to the strength of the external magnetic field.

Now we consider the effect of the $\mathbf{B}_{Z0}$ field on the magnetic moment of the hydrogen nucleus. Using equation (1.1), the motion of the magnetic moment can be determined by assuming an initial state and considering the torque on the nucleus. Taking the initial state of the magnetic moment to be $\boldsymbol{\mu}(0) = \mu_{x0}\hat{\boldsymbol{x}} + \mu_{y0}\hat{\boldsymbol{y}} + \mu_{z0}\hat{\boldsymbol{z}}$ and using the classical definitions of torque given by

$$\boldsymbol{\tau} = \frac{d\mathbf{L}}{dt}, \quad \text{and} \quad \boldsymbol{\tau} = \boldsymbol{\mu} \times \mathbf{B}, \tag{1.2}$$

we combine equations (1.1) and (1.2) to get

$$\frac{d\boldsymbol{\mu}}{dt} = \gamma\left(\boldsymbol{\mu} \times \mathbf{B}\right). \tag{1.3}$$

This yields a system of 3 linear equations for μ_x, μ_y, and μ_z. Under the sole presence of the $\mathbf{B}_{Z0}$ field, the vector equation (1.3) expands in each component to the system

$$\begin{aligned} \frac{d\mu_x}{dt} &= \gamma\mu_y B_{Z0} \\ \frac{d\mu_y}{dt} &= -\gamma\mu_x B_{Z0} \\ \frac{d\mu_z}{dt} &= 0. \end{aligned} \tag{1.4}$$

The first two coupled equations of (1.4) can be transformed into two second order decoupled linear ordinary differential equations. The solution of system (1.4) subject to the given initial condition is known to be

$$\boldsymbol{\mu}(t) = \left(\mu_{x0}\cos\left(\omega t\right) + \mu_{y0}\sin\left(\omega t\right)\right)\hat{\boldsymbol{x}} + \left(\mu_{y0}\cos\left(\omega t\right) - \mu_{x0}\sin\left(\omega t\right)\right)\hat{\boldsymbol{y}} + \mu_{z0}\hat{\boldsymbol{z}}. \tag{1.5}$$

This describes the magnetic moment of the nucleus precessing around the $+z$-axis (the direction of the applied magnetic field) with frequency ω. The frequency of precession, ω, is given by the Larmor frequency where

$$\omega = \omega_0 = \gamma B_{Z0}, \tag{1.6}$$

in this case. The Larmor relation states that the precessional frequency is proportional to the strength of the external magnetic field. It can be shown that the linear frequency of precession, $f = 2\pi\omega_0$, is the same as the frequency of the photon absorbed or emitted, ν, when the proton flips between low energy and

high energy states (see Jin [60] p7 for a derivation).

1.3.3 NMR Response of a Bulk Sample

In the absence of an external magnetic field a paramagnetic bulk material has no net magnetisation. All the particles are randomly aligned resulting in no net moving charge. Once a magnetic field is applied, all the nuclei in the sample either align parallel or anti-parallel to the applied field. A small majority of the nuclei will align parallel with the $\mathbf{B}_{Z0}$ field, which assumes a lower energy state. Summing all the magnetic moments contained in the sample material yields a magnetisation vector, $\mathbf{M}$, given by

$$\mathbf{M} = (N_\alpha - N_\beta)\, n\mu_z \hat{\boldsymbol{z}},$$

where N_α and N_β denote the probabilities that a particular nucleus is found in the parallel or anti-parallel state respectively, and n denotes the number of particles in the material. As the majority of the protons' magnetic moments will align with the $\mathbf{B}_{Z0}$ field, the magnetisation vector will point in the $+z$-direction. However, the components of the magnetic moments in the x and y-directions are still randomly aligned, thus giving a net magnetisation of zero in the transverse plane. The magnetisation vector (constituting the sum of magnetic moments in the sample) satisfies the same linear differential equation system as the magnetic moment vector for individual nuclei (refer to (1.3)),

$$\frac{d\mathbf{M}}{dt} = \gamma \mathbf{M} \times \mathbf{B}. \tag{1.7}$$

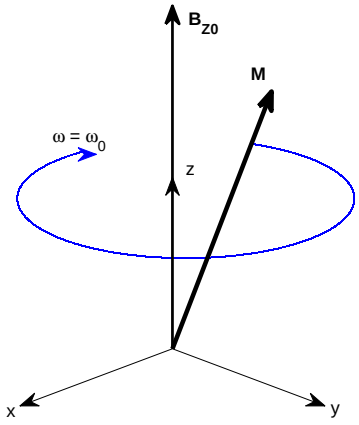

(a) Stationary frame (Undashed coordinates)

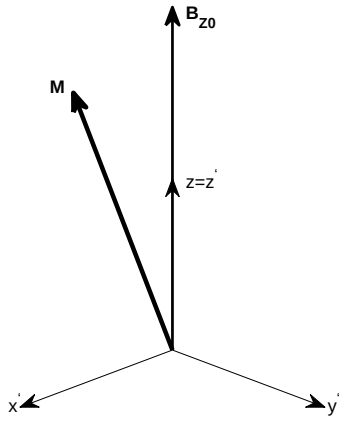

(b) Rotating frame (Dashed coordinates)

Figure 1.5: (a) The magnetisation vector precessing around the $+z$-axis in the laboratory (undashed coordinates) frame of reference. (b) The same magnetisation vector viewed in the rotating frame of reference (dashed coordinates). Here, $\mathbf{M}$ appears stationary.

Assuming at some instant that $\mathbf{M}$ is tilted so that $\mathbf{M} = M_{x0}\hat{\boldsymbol{x}} + M_{z0}\hat{\boldsymbol{z}}$, gives a similar solution for $\mathbf{M}$ as solving (1.3) for $\boldsymbol{\mu}$ subject to the specified initial state (refer to (1.5)). Hence

$$\mathbf{M} = M_{x0}\left(\cos\left(\omega_0 t\right)\hat{\boldsymbol{x}} - \sin\left(\omega_0 t\right)\hat{\boldsymbol{y}}\right) + M_{z0}\hat{\boldsymbol{z}}. \tag{1.8}$$

Analogous to the magnetic moment case, (1.8) describes the magnetisation vector precessing around the $+z$-axis with frequency ω_0 in a clockwise direction. By making a transformation of coordinates, the magnetisation vector can be viewed as stationary in a new rotating reference system. Defining a rotating reference system such that

$$\begin{aligned}
\hat{\boldsymbol{x}}' &= \cos\left(\omega_r t\right)\hat{\boldsymbol{x}} - \sin\left(\omega_r t\right)\hat{\boldsymbol{y}}, \\
\hat{\boldsymbol{y}}' &= \sin\left(\omega_r t\right)\hat{\boldsymbol{x}} + \cos\left(\omega_r t\right)\hat{\boldsymbol{y}}, \\
\hat{\boldsymbol{z}}' &= \hat{\boldsymbol{z}},
\end{aligned}$$

leads to

$$\mathbf{M} = M_{x0}\hat{\boldsymbol{x}}' + M_{z0}\hat{\boldsymbol{z}}', \tag{1.9}$$

when the reference frame is rotating with frequency $\omega_r = \omega_0$. Figure 1.5 depicts the motion of $\mathbf{M}$ in the stationary and dashed coordinate systems when the reference frame is rotating at the Larmor frequency corresponding to the primary magnetic field. This new (dashed) coordinate system provides a useful reference frame for analysing the motion of the magnetisation vector under the influence of an oscillating transverse magnetic field, discussed next.

1.3.4 RF pulse effects

With the sample in the presence of the static $\mathbf{B}_{Z0}$ field, it can be assumed that at any instant and in either frame, $\mathbf{M} = M_0\hat{\boldsymbol{z}}$. The sample is now ready to be irradiated with a transverse RF (radiofrequency) pulse from which the effect on the magnetisation vector will be sought. With the RF pulse taken to be an oscillating linearly polarised field in the x-direction and denoted by $\mathbf{B}_1$, we may write

$$\mathbf{B}_1 = B_1 \cos(\omega_1 t)\hat{\boldsymbol{x}}.$$

This representation of the RF field can be broken down into two circularly polarised fields of equal magnitude, i.e. $\mathbf{B}_1 = 1/2\mathbf{B}_{CW} + 1/2\mathbf{B}_{ACW}$, where $\mathbf{B}_{CW}$ denotes a clockwise rotating field and $\mathbf{B}_{ACW}$ denotes an anti-clockwise rotating field. The form of the clockwise and anti-clockwise fields written in the laboratory frame are given below:

$$\begin{aligned} \mathbf{B}_{CW} &= B_1 \left(\cos(\omega_1 t)\hat{\boldsymbol{x}} - \sin(\omega_1 t)\hat{\boldsymbol{y}}\right) \\ \mathbf{B}_{ACW} &= B_1 \left(\cos(\omega_1 t)\hat{\boldsymbol{x}} + \sin(\omega_1 t)\hat{\boldsymbol{y}}\right). \end{aligned}$$

The advantage of using the rotating reference frame now becomes clear. Setting the frequency of the rotating reference frame to match the frequency of the oscillating RF field, $\omega_r = \omega_1$, we obtain

$$\mathbf{B}_1 = \frac{1}{2}\mathbf{B}_{CW} = \frac{1}{2}B_1\hat{\boldsymbol{x}}',$$

where it can be shown that the contribution of the $\mathbf{B}_{ACW}$ field is negligible when $\omega_1 = \omega_r = \omega_0$ (see Jin [60] p15).

Considering the equation of motion for the magnetisation vector (1.7) reformulated in the rotating reference frame we obtain

$$\frac{\delta \mathbf{M}}{\delta t} = \gamma \mathbf{M} \times \mathbf{B}_{eff}, \tag{1.10}$$

where $\mathbf{B}_{eff}$ denotes the effective magnetic field constituting the sum of the primary field and the x-directed RF field. Confining ourselves to the rotating frame momentarily, the effective magnetic field takes the form

$$\mathbf{B}_{eff} = \frac{B_1}{2}\hat{\boldsymbol{x}}' + \left(B_{Z0} - \frac{\omega_1}{\gamma}\right)\hat{\boldsymbol{z}}', \tag{1.11}$$

based on the assumption that the effects from $\mathbf{B}_{ACW}$ are negligible. Equation (1.11) demonstrates that when $\omega_1 = \omega_0$ the effective magnetic field will lie solely in the transverse plane ($\mathbf{B}_{eff} = B_1/2\hat{\boldsymbol{x}}'$) and rotate such that it keeps pace with the rotating coordinate axes.

The resulting motion of the magnetisation vector follows from previous analysis and leads us to the conclusion that the magnetisation will precess around the transverse rotating effective field with frequency $\omega_{eff} = \gamma B_1/2$.

When the frequency of the RF pulse matches the Larmor frequency associated with the primary magnetic field (i.e. when $\omega_1 = \omega_0$) there are two effects on $\mathbf{M}$. Firstly, some magnetic moments in the sample will be encouraged to 'flip' to the higher energy state. Since there was an initial imbalance of spins aligned in the $+z$-direction, this first effect will reduce the magnitude of M_z. Secondly, an RF pulse in the x-direction will force the magnetic moments of each nucleus to align with the $\mathbf{B}_{eff}$ field (an $\hat{\boldsymbol{x}}'$-directed field), establishing coherence and producing a non-zero net transverse component to the magnetisation vector. These two effects in combination will have an observer in the stationary frame viewing the

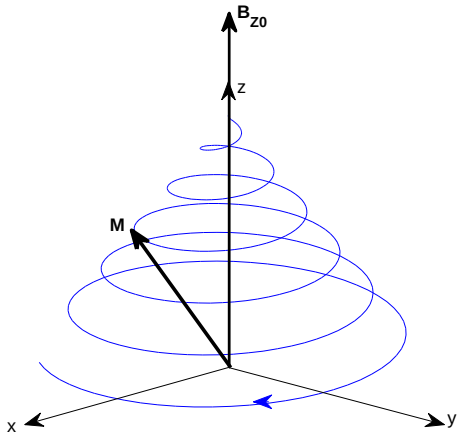

(a) Stationary frame (Undashed coordinates)

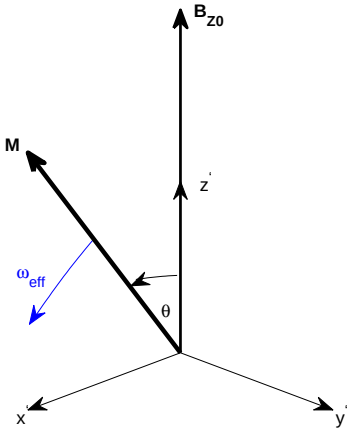

(b) Rotating frame (Dashed coordinates)

Figure 1.6: (a) Motion of the magnetisation vector in the stationary frame. A transverse RF pulse of frequency $\omega_1 = \omega_0$ will cause the magnetisation vector to spiral from the $+z$-axis towards the transverse plane. (b) Motion of the magnetisation vector in the rotating frame. The magnetisation vector will tilt over towards the xy-plane, when an RF pulse is applied in the x-direction.

magnetisation vector spiral from the $+z$-axis downwards to the transverse plane. Correspondingly, in the rotating frame an observer will see the magnetisation vector tilt further away from the $+z$-axis until it lies in the transverse plane. This motion is termed nutation and is depicted in figures 1.6(a) and 1.6(b).

Being able to control the angle of deviation of the magnetisation vector from the $+z$-axis is important for image formation. The flip angle, θ, is dependent on both the duration of the RF pulse, T, and the strength of the effective field B_1, and is simply given by

$$\theta = \frac{1}{2}\gamma B_1 T. \tag{1.12}$$

The time taken to perturb the magnetisation vector to the xy-plane ($\theta = \pi/2$ rad) is therefore given by $T_{90} = \pi/\gamma B_1$ and is commonly described as a 90 degree pulse. A typical RF sequence will be a combination of RF pulses that rotate the magnetisation vector 90 degrees and 180 degrees from the vertical.

1.3.5 Relaxation

This classical model suggests that once the RF pulse is removed, the magnetisation vector will continue to rotate in the transverse plane. However, experiments show that the magnetisation vector will spiral back to align with the $+z$-axis after the RF pulse is removed and $\mathbf{M} = M_0\hat{\boldsymbol{z}}$ once more. The restoration of the magnetisation vector happens on two time scales, T_1 and T_2. After the RF pulse, some nuclei emit a photon of frequency ω_0 and 'flip' back to the lower energy state to restore thermal equilibrium. This process is termed 'longitudinal relaxation' and is denoted by time scale T_1. The second time scale, T_2, refers to 'transverse relaxation' (or 'spin-spin relaxation'), and is the time taken for the magnetic mo-

ments in the transverse direction of each nuclei to lose coherence and randomly align, yielding no net magnetisation in the transverse direction. It is these two processes (which both involve emissions of photons) that are 'observed' by an RF receiver.

Transverse relaxation is a result of field inhomogeneities and mutual effects from each magnetic moment. The term 'spin-spin' relaxation is often used as it is the spins of neighbouring nuclei that mutually affect each other. Due to unavoidable field inhomogeneities, two nuclei next to each other will be experiencing a slightly different magnetic field strength e.g. $B_{Z0} + \Delta B_{Z0}$ compared with B_{Z0}. This difference in field strength will cause nuclei next to each other to precess at slightly different rates, which over time leads to complete decoherence.

The mathematical model used to describe this phenomenon requires a semi-classical form of the Bloch equations and necessarily includes mutual effects between nuclei. We are familiar with the fact that $\mathbf{M}$ satisfies the same differential equations as $\boldsymbol{\mu}$ and as such the model for $\mathbf{M}$, in component form, extends system (1.4) to include mutual interactions of neighbouring nuclei.

$$\frac{dM_x}{dt} = \gamma B_{Z0} M_y - \frac{M_x}{T_2} \tag{1.13}$$

$$\frac{dM_y}{dt} = -\gamma B_{Z0} M_x - \frac{M_y}{T_2} \tag{1.14}$$

$$\frac{dM_z}{dt} = \frac{M_0 - M_z}{T_1}. \tag{1.15}$$

In the simple case of a 90 degree RF pulse being removed, the magnetisation vector initially lies in the transverse plane and at some instant is given by $\mathbf{M}(0) = M_0\hat{\boldsymbol{x}}$. The solution to equations (1.13) - (1.15) subject to this initial state are given

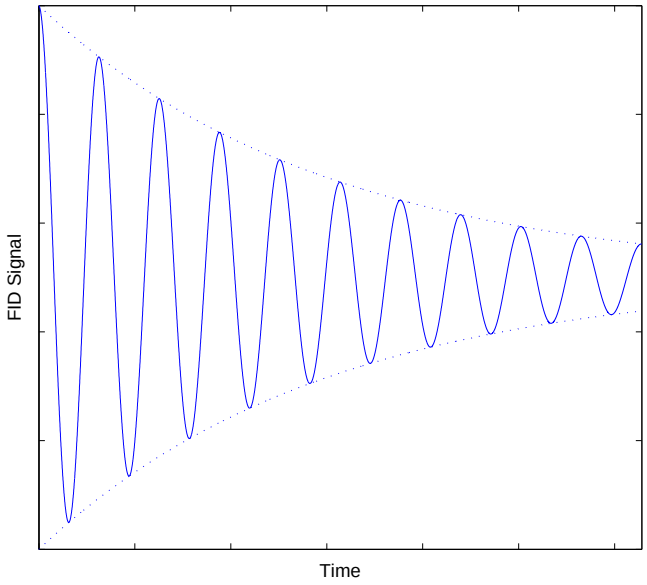

Figure 1.7: An exponentially damped oscillating wave modelling the decay of the magnetisation vector in the transverse direction. This is known as free induction decay (FID).

below:

$$\begin{aligned} M_x(t) &= M_0 e^{-t/T_2} \cos(\gamma B_{Z0} t) \\ M_y(t) &= -M_0 e^{-t/T_2} \sin(\gamma B_{Z0} t) \\ M_z(t) &= M_0 \left(1 - e^{-t/T_1}\right). \end{aligned}$$

The z-component of $\mathbf{M}$ can be seen to grow in magnitude over time until $M_z = M_0$ once more. The solutions for M_x and M_y are exponentially damped oscillating waves dependent on the transverse relaxation time constant. Via Faraday's law, if an RF receiver coil is aligned in the transverse direction, a current will be induced in the coil due to the change in magnetisation during the relaxation process. This induced current, referred to as transverse field free induction decay (FID), represents the signal for NMR (figure 1.7). Together the intensity of the

recorded FID and estimates of T_1 and T_2 discriminate between different tissue types of a sample under investigation.

1.3.6 Spatial Encoding and Slice Selection

The step from NMR spectroscopy to MRI requires the inclusion of gradient coils. Their purpose is to superimpose a known inhomogeneity on top of the primary magnetic field in order to spatially encode the imaging region. A gradient coil must provide unambiguous spatial information about the region being imaged and is typically designed to produce a linear field for this reason. A nucleus exposed to a slightly stronger magnetic field will precess faster, in accord with the Larmor relation. Given a three dimensional sample to be imaged, it is necessary to excite nuclei over a volume centred around a chosen plane. This can be achieved by applying a gradient field in combination with an RF pulse. For the purpose of illustration, we choose a z-gradient centred around z_0 to be our 'slice selection' gradient (denoted by G_s) and apply it across the sample. (This means we are exciting nuclei over several xy-planes centred around $z = z_0$.) The z-gradient (denoted by G_z) is defined to be spatially linear and when added to the primary field produces a total field

$$\begin{aligned} B &= B_{Z0} + G_z z \\ \Rightarrow \omega_L &= \gamma \left(B_{Z0} + G_z z \right). \end{aligned}$$

This last equation is a direct result of the Larmor relation (1.6). It states that, relative to z_0, nuclei located at larger z-positions will precess faster and nuclei at smaller z-positions will precess slower.

A result of Maxwell's equations in quasi-static form in a source free region of

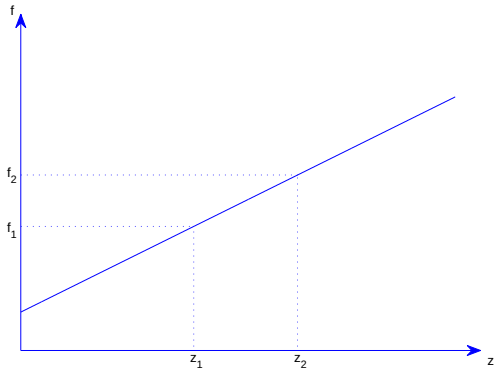

(a) Spatial encoding using a linear z-gradient can be seen to associate a unique precessional frequency with each z-location.

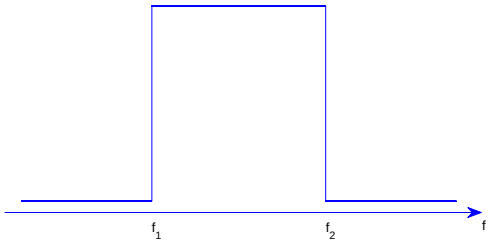

(b) A square wave of frequency bandwidth $\Delta f = |f_2 - f_1|$

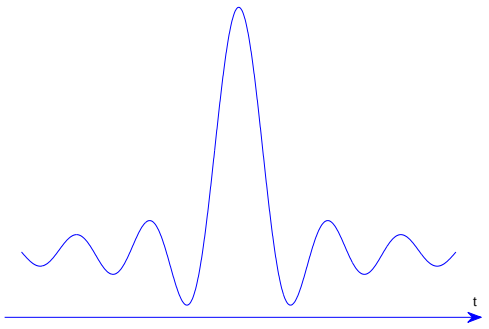

(c) A *sinc* wave in time with frequency bandwidth Δf

Figure 1.8: Figure (a) demonstrates (through the Larmor relation) how the application of a z-gradient frequency encodes a slice. Figure (b) is a square wave of frequencies corresponding to the ones excited by the z-gradient in the slice of thickness Δz. The Fourier Transform of the square wave (figure (b)) gives a *sinc* wave in time, figure (c). Thus to only excite nuclei in the slice of thickness Δz we need to use a *sinc* form RF pulse of determinable bandwidth.

space is that a 'linear' field must be accompanied by a transverse component. The effects (and derivation of the effects) of this concomitant field are discussed in Haacke *et al.* [45] p849 and are shown to have a negligible effect on the Larmor frequency for large primary field strengths.

We wish to excite nuclei over a specific range of z-locations, i.e. from $z_1 \leq z \leq z_2$, where $\Delta z = |z_2 - z_1|$ and $z_0 = (z_1 + z_2)/2$, by using a z-gradient and an RF pulse. The task is to determine the time form of the RF pulse that will excite only the nuclei over the desired range. Figure 1.8(a) shows that each z-location corresponds to a unique precessional frequency after the application of a z-gradient. Thus, the application of an RF pulse that produces a square wave in the frequency domain (figure 1.8(b)) will excite only the nuclei located from z_1 to z_2. Determination of the time form of the RF pulse required to produce the square wave in the frequency domain simply involves taking its Fourier Transform. This gives the well known *sinc* function as the envelope of the RF pulse (where $sinc(t) = \sin(t)/t$) in time; as shown in figure 1.8(c). A *sinc* function notionally has an infinite domain, which is obviously impractical for real applications, so in practice an RF signal has a truncated *sinc* envelope. The *sinc* envelope (of frequency bandwidth Δf) is usually truncated to approximate a Gaussian envelope, which also has a simple Fourier Transform. This unavoidable truncation of the ideal *sinc* pulse, however, does lead to non-rectangular slice profiles.

1.3.7 Image Construction Techniques

To acquire data for image formation, slice selection and spatial encoding must happen in the x, y, and z-directions. The operation of the x and y-gradients is similar to that presented for the z-gradient in section 1.3.6. The manner in which

the collection of gradient coils is switched on and off is dependent on the choice of image reconstruction technique, of which there are two major categories: back projection and Fourier Transform.

Chronologically, the first technique developed was termed 'back projection', referring to the way that images are created by the intersection of data projected back along contributing paths. We first select our slice by applying, for example, a z-gradient followed by an RF *sinc* pulse with the appropriate bandwidth; thus only nuclei in the z-direction from z_1 to z_2 are excited and precess in cohesion. To frequency encode the z-slice, we then apply a transverse gradient, for example an x-gradient, momentarily after the z-gradient and associated RF pulse. The x-gradient has a similar effect to that of the z-gradient, where the total magnetic field is now given by $B = B_{Z0} + G_x x$ with the magnitude of $G_z > G_x$. When the x-gradient is applied another RF *sinc* pulse with associated Larmor frequency is applied and the FID is recorded. The term 'readout gradient' (denoted by G_f) is used to describe the x-gradient in this case, as it is the FID associated with the x-gradient that is recorded. This process is then repeated at an angle ϕ to the x-axis. This is done by using combinations of x and y-gradients with $G_\phi = G_x \cos\phi$ and $G_\phi = G_y \sin\phi$. All the FID information (corresponding to each ϕ specification) is the data that leads to an image being constructed. Figure 1.9 presents one example of the switching sequences required to construct an image using a back projection imaging technique.

The back projection technique is, however, very sensitive to inhomogeneities in the gradient and primary fields and so was discarded in favour of the Two Dimensional Fourier Transform (2DFT) method (which forms the basis of modern imaging techniques; see Bernstein *et al.* [5]). Back projection uses frequency encoding to gain spatial information about a sample. In contrast, the 2DFT method, in

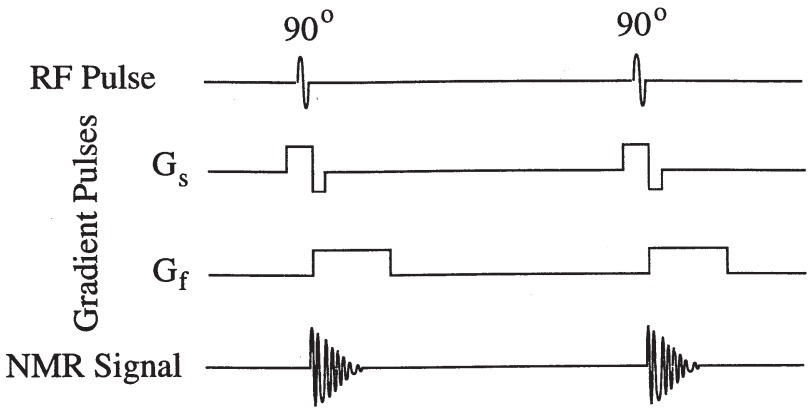

Figure 1.9: A pictorial description of the pulses required to perform a back projection image. This image was taken from Jin [60] p34.

addition to using frequency encoding, also uses phase encoding. The technique begins in the same fashion as for back projection, by applying a z-gradient to excite the nuclei in the xy-space from z_1 to z_2. Next, a y-gradient (the phase encoding gradient, denoted by G_ϕ) is applied to the sample. Considering nuclei solely in one xy-plane, the nuclei in the $+y$-space will precess faster and gain a positive accumulated phase difference. Similarly, nuclei in the $-y$-space will lag behind the nuclei in the $+y$-space. Typically, after the edge nuclei achieve a phase difference of 180 degrees the y-gradient pulse is halted. All nuclei in the xy-plane are now experiencing the same magnetic field and hence precess at the same rate; however, an induced phase shift has occurred in the y-direction. The x-gradient is now applied to frequency encode the sample in the x-direction, similar to the 'back projection' technique. Each nucleus in the xy-plane now has a unique frequency and phase of precession. This precessional information is detected by the RF receiver (repeated for different ϕ values) and, as in the previous case, this data leads directly to an image. A typical 2DFT pulse sequence can be seen in figure 1.10. The pulsing sequence the gradient coil undergoes plays an important role in the amount of noise heard and is considered in this thesis in chapter 2 (but not

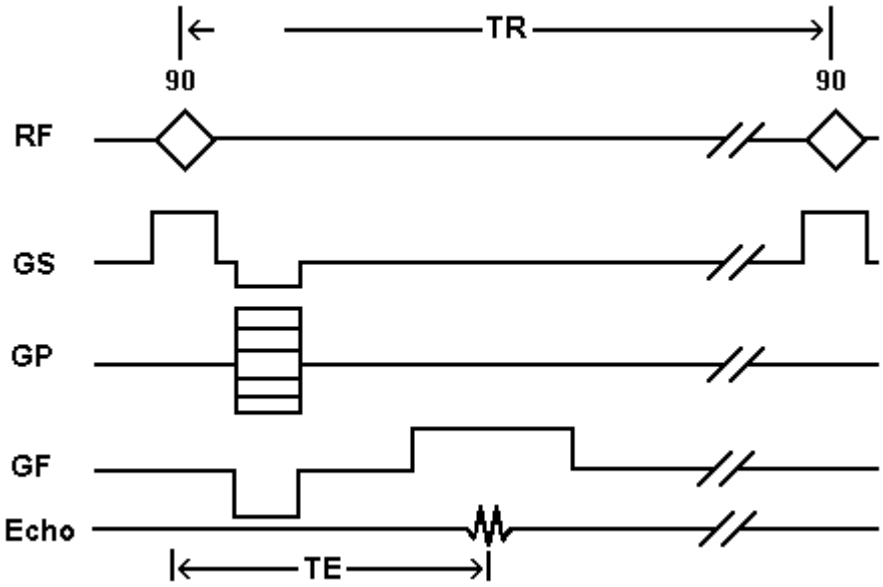

Figure 1.10: A depiction of the pulse sequences required to form an image using a Gradient Echo Two Dimensional Fourier Transform technique. This image was taken from http://www.mritutor.org/mritutor/gre.htm

explored fully).

1.4 Basic Coil Patterns

The importance of magnets capable of producing high quality gradient fields was outlined in section 1.2 and we now discuss the magnetic fields produced by some fundamental winding patterns. This is a good starting point because MRI hardware components have winding patterns that generally consist of a complex combination of basic winding patterns arranged around a cylindrical former. The magnetic field produced by any current carrying conductor can be calculated from the Biot - Savart law, a derivation of which appears in appendix B. When the current carrying conductor is composed of discrete wires, the Biot-Savart Law

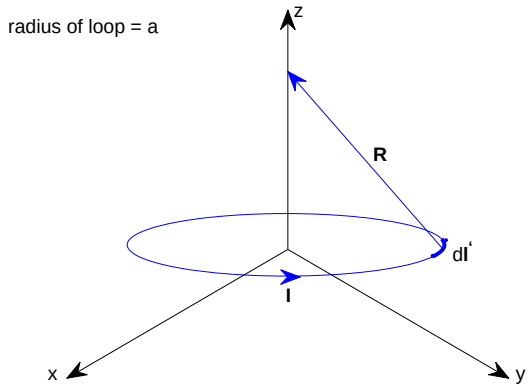

Figure 1.11: The coordinate system and geometry adopted for a current carrying loop, with radius a, centred at $x = y = z = 0$, carrying amperage I.

takes the form (see appendix B)

$$\mathbf{B}(\mathbf{r}) = \frac{\mu_0 I}{4\pi} \int_C \frac{d\mathbf{l}' \times \mathbf{R}}{R^3} \tag{1.16}$$

where μ_0 is the relative permeability of free space, I is the current travelling through the loop, $d\mathbf{l}'$ is an infintesimal length of the coil and R is the distance from the coil to the point where the field is to be calculated. Standard practice is to only consider the z-component of the magnetic field because the primary magnet (aligned with the z-axis) dominates all other fields required for MRI by several orders of magnitude; see Jin [60].

Let us first consider the field produced by a circular loop of wire. This will be of particular practical interest for a conventional cylindrically shaped MRI scanner. With the loop located in the xy-plane and centered at the origin, equation (1.16) gives

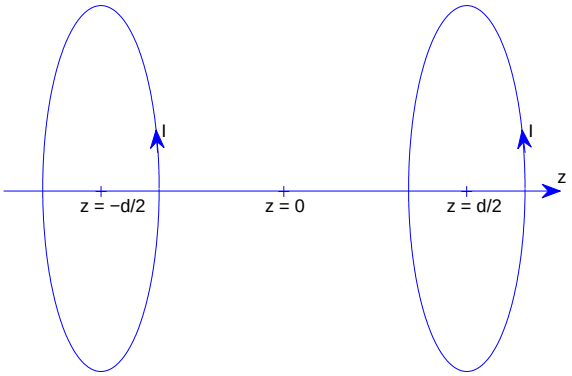

Figure 1.12: A Helmholtz Coil configuration. A Helmholtz coil produces a more homogeneous constant field when the loop separation is set to the loops' radius, i.e. setting $d = a$.

$$B_z(0,0,z) = \frac{\mu_0 I a^2}{2\left(z^2 + a^2\right)^{3/2}}, \tag{1.17}$$

for the z-component of the magnetic field along the z-axis. The field off the z-axis has a significantly more complex form involving complete elliptic integrals of the first and second kind (see Jin [60]) but this is not discussed further here.

1.4.1 Helmholtz Coil

The simplest combination of coil windings that leads to a constant magnetic field is the Helmholtz coil. A Helmholtz coil consists of two identical circular loops, of equal radius $r = a$, carrying the same current I, spaced symmetrically about the z-axis, at $z = \pm d/2$, as seen in figure 1.12. The magnetic field produced by this coil is evaluated simply from (1.17) as the sum of fields produced from each loop

independently, thus giving

$$B_{Helm}(z) = \frac{\mu_0 I a^2}{2\left[(d/2-z)^2+a^2\right]^{3/2}} + \frac{\mu_0 I a^2}{2\left[(d/2+z)^2+a^2\right]^{3/2}}. \tag{1.18}$$

Expanding B_{Helm} as a Taylor series about $z = 0$, we can asses the homogeneity of the field by looking at the lowest order contaminating term. Due to the symmetric nature of the Helmholtz coil, all odd derivatives of B_{Helm} are zero at $z = 0$; thus B_{Helm} can be expressed by an even power series expansion. Considering the second derivative of B_{Helm}

$$\frac{d^2 B_{Helm}}{dz^2} = \frac{3\mu_0 I a^2}{2}\left[\frac{4(d/2-z)^2-a^2}{[(d/2-z)^2+a^2]^{7/2}} + \frac{4(d/2+z)^2-a^2}{[(d/2+z)^2+a^2]^{7/2}}\right],$$

we see that B''_{Helm} vanishes at $z = 0$ for $d = a$. Thus, by positioning the current loops a distance $d = a$ apart the Helmholtz coil will produce a significantly more homogeneous field about $z = 0$. The field produced by the Helmholtz coil is now constant through to the third power of z, and thus B_{Helm} can be written as

$$B_{Helm}(z) = B_z(0) + O\left((z/d)^4\right).$$

A graph of the field B_{Helm} produces on the z-axis around $z = 0$ is given in figure 1.13. An important point to remember is that the expression for B_{Helm} is only computed along the z-axis. Thus, the Helmholtz coil only produces a (relatively) constant field along the line $x = y = 0$. However, using Maxwell's equations, it can be shown that a field producing small variations along one axis will have small variations at a slight distance off the axis as well; see Haacke *et al.* [45]. Thus, the magnetic field emanating from a Helmholtz coil is relatively constant over a small volume around $z = 0$.

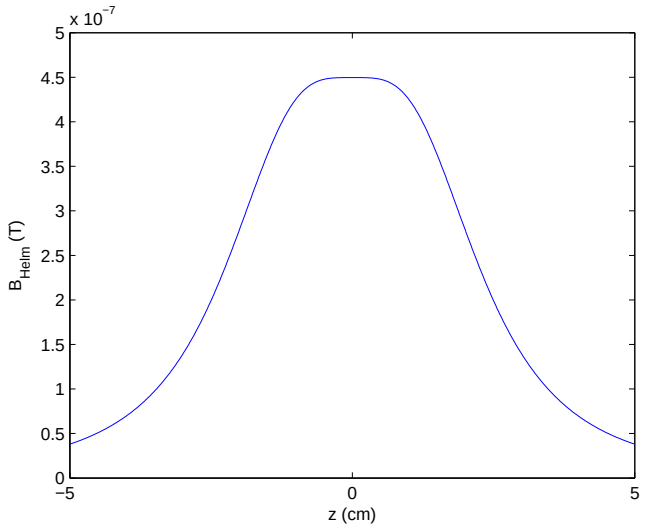

Figure 1.13: The field produced by a Helmholtz coil carrying current 1 A, with loop radius $a = 2\,\text{cm}$, along the z-axis. Note the field is relatively constant around $z = 0$.

1.4.2 Maxwell Coil

A Maxwell coil (depicted in figure 1.14)) is identical to a Helmholtz coil except the currents flowing in each loop oppose each other. Hence, the field created by a Maxwell coil is analogous to the Helmholtz field with the sign reversed in the second term of (1.18), giving

$$B_{Max}(z) = \frac{\mu_0 I a^2}{2\left[(d/2 - z)^2 + a^2\right]^{3/2}} - \frac{\mu_0 I a^2}{2\left[(d/2 + z)^2 + a^2\right]^{3/2}}. \tag{1.19}$$

Considering a Taylor series expansion of B_{Max} about $z = 0$ we see (as opposed to the Helmholtz coil) all even derivatives vanish. Thus, a Maxwell coil produces a linear field contaminated with higher order odd terms. Looking at the third derivative of B_{Max}

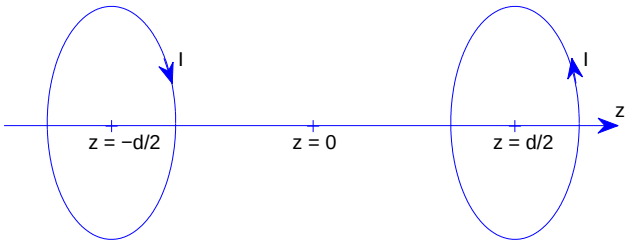

Figure 1.14: A Maxwell Coil configuration. The linearity of the field produced by a Maxwell Coil is improved when the separation of the loops is required to satisfy $d = \sqrt{3}a$.

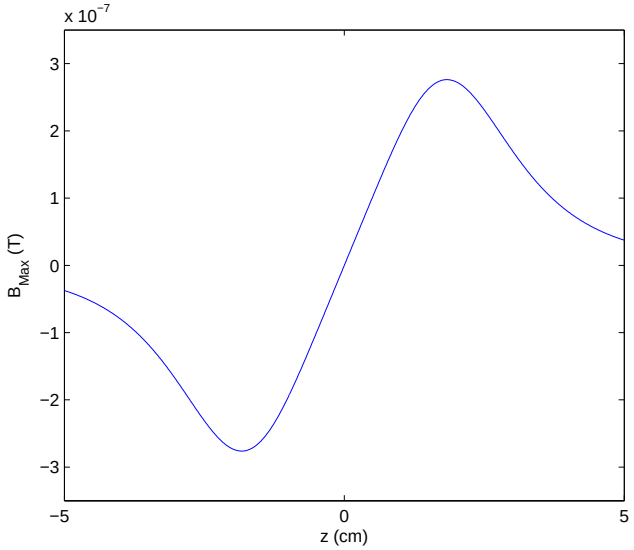

Figure 1.15: The magnetic field emanating from a Maxwell Coil arrangement with current 1 A in each loop. Each loop has radius $a = 2\,\text{cm}$ and the field is calculated along the line $x = y = 0$. Note the field is relatively linear in the neighbourhood around $z = 0$.

$$\frac{d^3 B_{Max}}{dz^3} = \frac{15\mu_0 I a^2}{2} \times \left[\frac{4(d/2-z)^3 - 3a^2(d/2-z)}{\left[(d/2-z)^2+a^2\right]^{9/2}} + \frac{4(d/2+z)^3 - 3a^2(d/2+z)}{\left[(d/2+z)^2+a^2\right]^{9/2}} \right],$$

we note by shifting the z-location of the wire loops to $d = \sqrt{3}a$, we can eliminate the third order derivative at $z = 0$. This produces a homogeneous linear field through to fourth order, i.e.

$$B_{Max}(z) = B_z^{'}(0)z + O\left[(z/d)^5\right].$$

The field produced by a Maxwell coil along the z-axis is given in figure 1.15.

In the case of either the Helmholtz or Maxwell coil, improvements in homogeneity can be made simply by increasing the number of loop pairs. An increase to three coil pairs (arranged at different z-locations, carrying different amounts of current and allowing for different radii) can produce a constant field through to twelfth order; see Weinstock *et al.* [113], in the case of the Helmholtz coil arrangement.

1.4.3 Golay Coil

Another commonly desired field used in MRI is a linearly varying field in a transverse direction of the B_z field. To produce a transverse gradient, a form of Golay (or 'double-saddle') coil is used (methods for deriving these patterns can be found in articles by Romeo and Hoult [97]). Placing a wire with current flowing in the $-x$-direction will produce a linear variation of the B_z field in the y-direction. More wires aligned in the $-x$-direction will increase the strength of the gradient field and (similarly with the Helmholtz and Maxwell coils) if placed precisely, can improve the homogeneity of the field as well. If four wires are placed as shown in

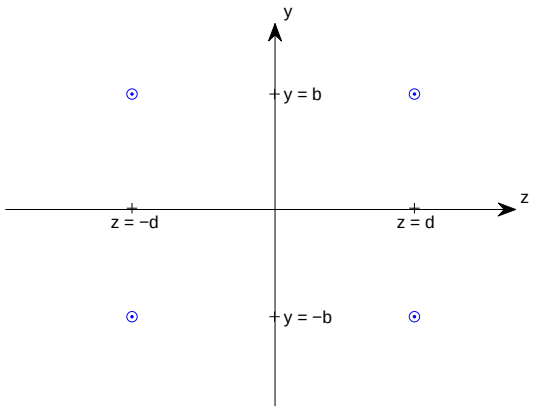

Figure 1.16: One particular discrete wire arrangement that produces a y-gradient in the z-component of the magnetic field (B_z). The four wires are located at $y = \pm b$ and $z = \pm d$ respectively and have current flowing in the $-x$-direction. A circle with a dot denotes current flowing out of the page.

figure 1.16, the magnetic field is calculated to be

$$B_{Golay}(0, y, z) = \frac{\mu_0 I}{2\pi} \frac{b - y}{(b - y)^2 + (d - z)^2}. \tag{1.20}$$

The $B_z(y)$ gradient field can be made more homogeneous (about $y = 0$) by arranging windings accordingly to eliminate the third derivative of (1.20) with respect to z. Specifying the positions of the wires required to make the third derivative of B_{Golay} zero is done, typically, by giving the opening angle of the wires in the x-direction, and the angles the inner and outer arcs make from the z-axis (see Jin [60] p90 for a depiction of inner and outer arc angles). One practical example, found by Mansfield and Morris [80], is having angles of 22.5° and 67.5° for the inner and outer arcs from the z-axis respectively. Combinations of Golay coils are used in practice to achieve the requisite level of homogeneity (see Romeo and Hoult [97]). Picturing the four wires in figure 1.16 wound around a cylindrical shell yields the inner arcs of figure 1.17. To close the current loops, wires are

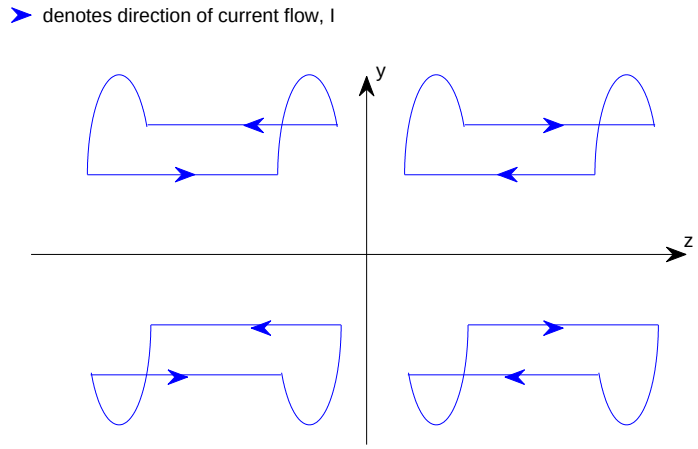

Figure 1.17: A basic winding pattern that produces a transverse gradient field in B_z. This winding pattern is referred to as a Golay coil.

simply added running in the z-direction by noting that they will not affect the B_z field in the y-direction. In addition, the outer arcs are far enough from the centre of the coil not to affect significantly the field from the inner arcs. Therefore, only the current in the inner arcs produces the y-gradient in a Golay coil. A Golay coil is typically inefficient for this reason. An x-gradient coil is created simply by rotating a y-gradient Golay coil 90 degrees about the z-axis.

1.5 Hardware

An MRI scanner conventionally consists of four main types of magnets arranged concentrically on a cylindrical shell. The four types of magnets are the primary magnet, gradient coils, shim coils, and RF coils, each to be discussed further. Along with the magnets, a fibreglass housing, cooling pipes, receivers, a spectrometer, patient monitoring systems, power supplies, a computer and a supporting

bed are assembled together to complete the scanner. An overview of the role each magnet plays will be given in the following subsections to put design concerns into context; detailed descriptions can be found in Vlaardingerbroek and den Boer [109], McRobbie *et al.* [83], Brown *et al.* [12], and Jin [60].

1.5.1 The Primary Magnet and Shim Coils

The primary magnet is responsible for producing a strong, homogeneous, constant magnetic field inside the chamber. In most texts, and in our model, the primary magnet's field (denoted by $\mathbf{B}_{Z0}$) is chosen to align in the z-direction, which points down the length of the chamber. For all forms of NMR imaging a strong $\mathbf{B}_{Z0}$ field is essential to align the nuclei and generate a large net magnetisation in the sample, which is obviously desirable for imaging. Modern clinical scanners have a typical primary field strength of 0.5 - 3 tesla (T).

The homogeneity required from the primary magnet's field depends on the intent of application. For medical imaging, the homogeneity typically needs to be on the order of a few parts per million (ppm) for the primary magnet system. As an example, an average 1.5 T magnet should have a field inhomogeneity on the order of 5 ppm over a volume of $0.5\,a$ (where a is the radius of the cylinder); see Haacke *et al.* [45]. Fluctuations over time in the field's strength can also be a problem. Importantly, the primary magnet is required to produce a stable time-independent magnetic field.

There are two simple coil structures that are used to produce a constant homogeneous field. One structure is the Helmholtz coil mentioned previously and the other is a solenoidal design, in which tightly wrapped loops of wire around a cylindrical shell produce a constant field along the central line of the shell. In theory,

an infinitely long solenoid produces a perfectly homogeneous magnetic field. For practical use, however, a solenoid long enough to generate the required level of homogeneity is very restricting to a patient and claustrophobic effects become more significant. Neither the Helmholtz or solenoidal coil structures can produce fields of sufficient homogeneity for modern scanners, so the addition of other coils is needed.

A brief description of shimming, shielding and the types of magnets available to create a primary magnet is given. The relevance of these three factors are discussed in terms of primary magnet construction; however, all of these issues are applicable to all forms of MRI coil hardware.

Shimming: It is rare to engineer a magnet with a field uniform enough for imaging purposes on its own. However, a sufficiently uniform field can be achieved through the use of shim coils. Specifically, one shim coil is designed to correct for one non-homogeneous component of the primary magnet. Analysing the primary magnet's field using spherical harmonics allows a decomposition of the field into homogeneous and non-homogeneous components. Targeting specific non-homogeneous components, e.g. $Z3$, or $XY2$, a shim coil can be designed to correct for this term. An array of shim coils, each targeted to correct for one undesired non-homogeneous component, is built on top of the primary magnet coil. Together, the primary magnet and shim coils in combination produce a field which meets the homogeneity criteria required for imaging.

Shielding: The large magnetic fields produced by the primary magnet are obviously not confined to within the MRI chamber. Stray external fields pose problems for staff working near a scanner and possible dangers arise if the fields extend be-

yond the room within which the scanner is housed. In addition, if a magnet is unshielded, the volume encompassed by the magnetic fields may be significant and with space a premium in hospitals this can be very costly. The need to minimise external fields is clearly of significance.

Two standard ways of shielding exist: passive and active shielding; see Jin [60]. Passive shielding uses solid lumps of iron to 'absorb' stray magnetic fields. The iron is built into the machine or into the walls of the room enclosing the scanner. Typically, passive shielding is not very effective and the homogeneity of the primary magnet is also affected and must be re-evaluated, with additional shims possibly being needed. Active shielding, however, requires another coil at a larger radius with current that opposes the flow of current in the primary magnet. The sum of the associated magnetic fields of the primary and shield coil will actively cancel, producing a significantly reduced external magnetic field. A negative result is that shielding will reduce the strength of the net field inside the chamber, so a higher current is required on both coils. Generally over twice the amount of current is required to produce a field inside the chamber of the same strength as an unshielded coil; see Haacke *et al.* [45]. The initial costs of shielding a primary coil may be large, but for superconducting magnets it is no more expensive to run and the ease of installation often makes up for the initial expense. The vast majority of modern scanners are actively shielded.

Types of Primary Magnets: Primary magnets typically have three standard designs: permanent, resistive or superconducting; refer to Hashemi *et al.* [47]. Each magnet has its own advantages and disadvantages, to be discussed briefly. Permanent magnets have the benefits of being cheap to build and run, and typically have low fringe fields external to the shell. A drawback of the per-

manent magnet design is that it is made of a ferromagnetic material and cannot be switched off easily, but the main disadvantage of a permanent magnet is that it produces a relatively low strength field. Resistive magnets are formed from wires wound around a cylindrical shell in the form of many Helmholtz pairs. A large current is forced through the wires, which causes the coil to heat up and become inefficient. The cost involved in the construction of a resistive magnet is relatively cheap; however, operating expenses associated with large current are generally quite high. Superconducting magnets produce very homogeneous, stable, strong magnetic fields (upwards of 4 T). They are designed similarly to resistive magnets but are cooled to temperatures of around 4.3 K using a liquid helium bath. At low temperatures there is effectively no resistance in the wires, which avoids the heating problem of resistive magnets. Costs involved with constructing a superconducting magnet are high but running costs are low providing the system stays cooled. Of the three types of main magnets, in modern MRI, superconducting magnets are the magnet of choice.

1.5.2 RF Coils

An RF coil is designed to excite nuclei in a sample into a coherent precession, so that the magnetisation vector can be tilted precisely. For an RF coil to be effective it is therefore required to produce a homogeneous $\mathbf{B}_1$ field and send a pulse with a narrow bandwidth centred around the corresponding Larmor frequency. A properly designed RF coil will thus excite nuclei over a specified range of spatial locations of length proportional to the bandwidth of the RF pulse. Then, upon removal of the RF pulse, the excited nuclei undergo an FID process. The FID is recorded by the RF coil and forms the data for image construction.

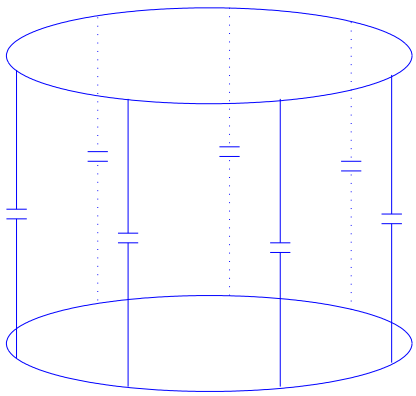

Figure 1.18: One schematic (low pass) RF birdcage coil.

Typically there are two types of RF coils used in scanners. One for emitting an RF signal, to tilt the magnetisation vector, and the other to receive the signal of the excited nuclei (the FID). The role of both RF coils can be accomplished by the one magnet; however, separate requirements are desired for both the transmitting and receiving coils respectively. A transmitting RF coil primarily is required to produce a homogeneous $\mathbf{B}_1$ field. The tilt angle of the magnetisation vector is directly proportional to the strength of the magnetic field (refer to equation (1.12)); thus, to excite the magnetisation vector precisely, the $\mathbf{B}_1$ field must be homogeneous. The major requirement of the receiving RF coil is that it has a high signal to noise ratio in order to obtain a clear signal.

One distinct difference between RF coils and all other coils discussed in this section is that the RF coil produces a high frequency time dependent magnetic field. Although a gradient coil is switched on and off, it produces a static field over time intervals of time 'on', whereas an ideal RF pulse has an amplitude described by a *sinc* envelope in time (refer to subsection 1.3.6). Another difference the RF

coil possesses between the former mentioned coils is that it points perpendicular to the primary magnet. The main magnetic field is typically aligned in the z-direction, and gradient and shim coils produce gradients (and fields of higher order) in components of the B_z field; by contrast, the RF field is directed in a transverse direction. This property gives the RF coil a very distinct design; refer to figure 1.18. The birdcage design was invented in 1982 by GE Medical Systems (see Hayes [48] for a more detailed history of the development of the birdcage coil). A birdcage coil forms a volume resonator and consists of capacitors in combination with distributed 'leg' inductance. The capacitors allow electrical energy to be stored external to the patient which is advantageous for both safety and efficiency.

An added efficiency for RF coils can be achieved through using quadrature coils. Quadrature coils produce and receive a circularly polarised field which gains an extra factor of $\sqrt{2}$ in efficiency (this result is derived in Jin [60]).

1.5.3 Gradient Coils

Many factors are involved with the design of gradient coils; see Turner [108]. Texts such as Jin [60] and Liang *et al.* [71] provide an in-depth analysis of gradient coil design, and an overview is given in a recent instructional paper by Hidalgo-Tobon [50].

The role of a gradient coil is to spatially encode the imaging region by giving a unique frequency and phase to each nucleus in the imaging region, as described in subsection 1.3.6. Thus, the field generated by a gradient coil must give unambiguous information about a nucleus's location. For this reason all gradient fields must be monotonic and this also suggests why a linear field is typically the design

of choice. The required homogeneity over the RF excitation range is less than that of other magnets involved in an MRI scanner, with deviations of around 5% being acceptable for most medical imaging scenarios.

The strength of the field produced by a gradient coil is significant and a typical value lies from 20 - 100 mT/m for clinical imaging; see Callaghan [13]. It is of critical importance that the inhomogeneity of the primary magnet is sufficiently small so as not to affect the function of the gradient coils. Taking a superconducting magnet of strength 4 T, it now becomes clear why such a primary magnet needs a field inhomogeneity of only a few parts per million.

Three of the biggest practical concerns involved with gradient coil design are its homogeneity (denoted by δ and is given by a percentage), efficiency (denoted by η with units of mT/Am), and inductance (denoted by L with units of Henry). These quantities are dependent on each other and through optimising one, the others typically will be negatively affected. Turner [108] derived a figure of merit, β, for a gradient coil, given as

$$\beta = \frac{\eta^2}{L\sqrt{\delta}}, \tag{1.21}$$

where the larger β is, the 'better' the gradient coil is. In equation (1.21) the inductance is denoted by L and the efficiency, η, is defined to be the strength of the gradient divided by the current passed through the coil. Also in equation (1.21), δ can have various definitions; however, Turner proposed that δ take the form

$$\delta = \frac{1}{V}\int\int\int_V \left[\frac{B_{observed} - B_{TF}}{B_{TF}}\right]^2 dV.$$

B_{TF} in the above expression is the 'target field' (or desired/requisite field) which

has been specified and is to be replicated by the gradient field.

The importance of the three terms η, δ, and L is immediately apparent. A smaller δ implies the field is more homogeneous, which leads to the formation of a sharper image. A reduction in L (techniques for reducing L can be seen in the article by Chronik and Rutt [19], and Turner [107]) means there is less stored energy in the coil (hence, the coils can be switched on and off faster), and an increase in η is obviously desirable for economic reasons.

Gradient coils are required to switch on and off, as described in subsection 1.3.6. Fast switching is used to reduce scanning time; however, fast switching can induce eddy currents which affect all fields in the proximity of the coil. An unwanted changing magnetic field will induce an unwanted electric field, which in turn induces another unwanted magnetic field leading to greater field inhomogeneities. Another problem with fast switching times is that eddy currents can be induced in a patient; see Glover [38]. This is termed peripheral nerve stimulation (PNS) and can range from a patient twitching, to potentially dangerous scenarios involving a patient's heart being stimulated. As such, safety guidelines have been put in place and a limiting ramp rate of $20\,\mathrm{T/s}$ has been set by the National Health and Medical Research Council in 1991 [88].

Another difficulty associated with operating MRI scanners that affects around 30% of patients is dealing with claustrophobia; see Fishbain *et al.* [28]. Loud noises combined with being confined to a small space for a long time leads to a number of patients requiring comforting or even sedation. To lessen claustrophobic effects, novel geometries have been created to give a more open sensation. Planar coils have been manufactured specifically to counter this problem, with success. Typically either square planar or circular planar geometries are used and both can produce adequate levels of field homogeneity. A drawback of planar

scanners is that planar main magnets have not been developed with desirably high field strengths and active sheilding.

Designing Gradient Coils: Here we discuss methods for mathematically designing gradient coils. Determining a magnetic field produced by a current simply involves applying the Biot - Savart Law; however, determining the current required to produce a given magnetic field is considerably more difficult. The problem is known to be very ill-conditioned and can be conceptually grasped because many different current distributions can produce very similar magnetic fields. The problem, therefore, has no unique solution. Hadamard [46] in 1932 qualified three characteristics for a problem to be ill-posed, one of them being non-existence of a unique solution.

There are two classes of manufactured gradient coils, involving 'discrete winding patterns' and 'distributed winding patterns'. Helmholtz and Maxwell coils (mentioned in subsections 1.4.1 and 1.4.2) are examples of coils with discrete winding patterns because the windings occupy set curves in space and are not flexible to move. They have the benefit of being simple to design and construct, and produce adequately homogeneous fields. For extremely homogeneous fields many windings may need to be placed very close to each other and consist of many turns. This leads to heating, inefficiency, and high cost. Also gradient coils that are made of discrete wires lack the ability to be customised with advantageous properties (such as low inductance). This is a major benefit of using distributed current windings and why we adopt such models throughout this thesis for gradient coil design.

Hoult [53] used a discrete wire approach and specified magnetic field points at locations z_m in order to generate the required winding pattern. Describing wire n

as having a z-location of z_n and carrying current I_n, Hoult's approach amounted to solving

$$\sum_{n=1}^{N} A_{mn} I_n = B_{TF}(z_m)$$

for the current I_n. Simple inversion of A_{mn} (by using Gaussian elimination or other methods) leads to highly oscillatory winding pattern solutions that are generally not buidable. This is because of the high sensitivity of input data (resulting in the ill-conditioned nature of the matrix A_{mn}), and other techniques such as regularisation must be used.

Distributed windings, on the other hand, do not occupy discrete positions and are assumed to be described by some current density $\mathbf{j}(\phi, z)$ which effectively utilises the whole surface of the coil. For a cylindrical geometry $\mathbf{j}$ has an axial and azimuthal component and hence $\mathbf{j}$ can be written as $\mathbf{j} = j_\phi \hat{\boldsymbol{e}}_\phi + j_z \hat{\boldsymbol{e}}_z$. Several methods have been developed to determine a suitable current density, $\mathbf{j}$, that will produce a given magnetic field over the imaging volume; such as Turner [108], Chronik and Rutt [19] and Forbes and Crozier [32, 33] to suggest a few. One robust design method was presented by Fisher *et al.*[29] that concerned themselves with designing a z-gradient that could optimise several design parameters at once. They developed a genetic algorithm whereby optimising a cost function allowed the spacing of each current loop to vary while keeping each loop the same radius and requiring a constant current applied to each loop. Importantly the 'buildability' of the coil was incorporated in the algorithm by accounting for the physical constraints of loop thickness and wire spacing.

A common way to determine a distributed winding pattern that produces a given

magnetic field is to use a least squares approach. Minimising ϵ where

$$\epsilon = \int_{-L}^{L} (B_z(z) - B_{TF}(z))\, dz, \tag{1.22}$$

B_z denotes the z-directed magnetic field and B_{TF} denotes the 'target field' in the z-direction, leads (similarly to Hoult's method) to an ill-conditioned system for $\mathbf{j}$. Several approaches can be taken to condition the system but the most popular choice is Tikhonov regularisation [104, 105]. Tikhonov regularisation involves adding constraints to improve conditioning of the system. Adding a smooth quadratic constraint allows the solution of a unique optimum in the form of a linear block matrix equation. Each term added has an associated penalty weighting factor, which, when increased, adds weight to that term. If we take, for example, minimising inductance as an added constraint, many current distributions will produce the required field but significantly fewer coils have minimum inductance as well. Any number of constraints (regularisation terms) can be added to increase conditioning of the system. The problem then becomes a balancing act between the weighting factors. Increasing the penalty weighting factors takes the emphasis off reproducing the target field but does reduce the inductance (in this example) and increase the conditioning of the system to allow a stable and unique solution.

Perhaps the most famous method for solving the inverse problem was developed by Turner and is called the 'target field method' [106]. Turner's paper in 1986 demonstrates a technique using Fourier transforms to derive the current on a cylindrical shell that produces a desired interior field. A brief overview of Turner's procedure follows. Turner begins by expressing the magnetic field using Green's

functions

$$B_z(r,\phi,z) = -\frac{\mu_0 a}{2\pi}\sum_{m=-\infty}^{\infty}\int_{-\infty}^{\infty} k e^{im\phi}e^{ikz} j_\phi^m(k) K_m^{'}(ka) I_m(kr) dk, \tag{1.23}$$

where $j_\phi^m(k)$ is the Fourier transform of the azimuthal current density component (as yet unknown) given by

$$j_\phi^m(k) = \frac{1}{m}\int_{-\infty}^{\infty}\int_{-\pi}^{\pi} j_\phi(\phi,z) e^{-im\phi} e^{-ikz} d\phi dz.$$

Turner next specifies a desired field at radius c (where $c < a$) called the 'target field', denoted by $B_{TF}(c,\phi,z)$. Returning to equation (1.23) and taking the inverse Fourier Transform we get

$$j_\phi^m(k) = \frac{-1}{\mu_0 a}\left[\frac{B_z^m(c,k)}{kK_m^{'}(ka)I_m(kc)}\right], \tag{1.24}$$

where $B_z^m(c,k)$ is the Fourier Transform of the target field, B_{TF}, and I and K are Modified Bessel functions of the first and second kind respectively. By using the continuity equation

$$\nabla \cdot \boldsymbol{j} = 0,$$

a relation in Fourier space between the two components of current density may be derived, and takes the form

$$j_z^m(k) = \frac{-m}{ka} j_\phi^m(k). \tag{1.25}$$

Turner has now completely specified the current density required to produce the target field (at $r = c$). The current density distribution can be determined simply by taking the inverse Fourier Transform of $j_\phi^m(k)$ and subsequently $j_z^m(k)$. Controlling the flow of current on the conducting cylinder is attained through

accurate placement of impediments (etchings) whose location is determined by analysis of the corresponding stream function (see Pissanetzky [93]).

A particularly useful result of this approach is that the actual field produced inside the target field radius (i.e. B_z for $r < c$) resembles the target field. More explicitly, the azimuthal component of B_z for $r < c$ is the *same* as the ϕ-dependence of B_{TF} ($= B_z(c, \phi, z)$), and the variations in r and z are *similar* to those specified in the target field.

One drawback to Turner's method is that it produces windings of notionally infinite length. Turner overcame this problem by multiplying the transformed current density, $j_\phi^m(k)$, by an exponential function (e.g. $t(k) = e^{-2k^2h^2}$, where h is a free parameter adjusted for each application) to force $j_\phi^m(k)t(k) \to 0$ as $k \to \infty$. He termed this process 'apodization'. Further advantages of Turner's approach can be taken if the desired gradient has the form

$$B_z(c, \phi, z) = G_z z g(z), \qquad \text{where} \quad g(z) = \left[1 + \left(\frac{z}{d}\right)^6\right]^{-1},$$

which, for $d = 1.7a$ implies that $g(z) \approx 1$. In this case, $g(z)$ has a convenient and commonly known Fourier Transform. Turner's method is practical for designing x and y-gradients as well.

Geometry, Lorentz Forces and Acoustic Noise: Once the current densities for each gradient coil have been determined, they are placed in combination as schematically shown in figure 1.19. This diagram gives a simple but accurate representation of the geometric nature of one gradient coil set consisting of only the primary coils. In practice, six gradient coils are used in a modern MRI scanner: one x, y, and z-primary gradient set and their respective shields; see

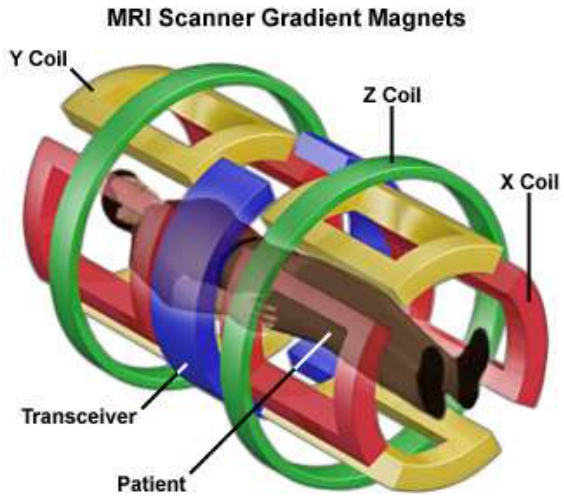

Figure 1.19: A schematic representation of an MRI scanner allayed around a patient. Only the primary set of gradient coils has been shown. This picture was taken from an online article written by Coyne with scientific advice from Grant [20].

Mansfield and Chapman [75] for some designs. Shielding a gradient coil is similar to shielding a primary magnet, with active shielding being the preferred method. The current windings on the shield are thus intended to oppose the windings of the primary coil.

Predominantly, this thesis is concerned with reducing the acoustic noise produced by a gradient coil. Acoustic noise levels of up to 130+ dB have been recorded (see Mansfield *et al.* [79]), which is typically where the threshold of pain begins. Noise is generated acoustically as a direct result of the Lorentz forces acting on the coil. Current flowing on the gradient coils and the field the coil is immersed in (the primary magnet's field) leads to a Lorentz force given by

$$\mathbf{F} = \mathbf{j} \times \mathbf{B}.$$

The reduction of noise can be classified into two categories. The first seeks to reduce the noise actively, by designing winding patterns that lead to quiet coils,

and the second involves reducing the noise passively, through damping effects. Active acoustic reduction typically involves minimising (or balancing) the Lorentz forces on the gradient coil, and was proposed by Mansfield *et al.* [77]; see also Chapman and Bowtell [18], and Bowtell and Peters [10]. Passively quiet coils involve methods such as wearing ear phones and adding absorbent material to the walls to soak up excess noise and minimise vibration. Edelstein *et al.* [23] mounted a thin copper layer to the gradient coil system to reduce deflection and noise by up to 25 dB.

Balancing the force solely has been accomplished (to a certain extent) by Labros *et al.* [65] and Alsop *et al.* [2] without the consideration of noise effects. Mechefske *et al.* [84, 87] took a gradient coil insert and developed a finite element model that matched their observed results of noise production. They concluded that the generated noise from an MRI scanner primarily comes from the gradient coils distorting in the radial direction. Other attempts to reduce noise have been made by Mansfield *et al.* [76], Wang and Mechefske [111, 112], and Yao *et al.* [116, 117].

Preliminary work has been done by Forbes *et al.* [30] to design quiet gradient coils. They were able to simulate acoustic noise (using a Tikhonov approach) but the winding patterns generated were, from an engineering point of view, unable to be constructed due to large sections of the coil requiring dense opposing windings.

The remainder of this thesis furthers the investigation of simulated pro-active acoustic noise reduction using a Tikhonov regularisation approach. Chapter 2 describes the geometry and physics of our shielded gradient coil and then extends the work of Forbes *et al.* [30] in several ways. The first major extension is made by considering a more general switching sequence and the second is a detailed investigation of resonance effects. A regularisation method is presented for attending to the ill-conditioned nature of the inverse problem. As well, constraints are added

to achieve an optimised noise output, while maintaining sufficient homogeneity of the field. Chapter 3 builds on chapter 2 by considering a complete 3D coil deflection model. The effects of a coil deforming in the azimuthal and longitudinal directions are considered as well as their role in simulated noise production. A technique to reduce simulated acoustic noise levels drastically is presented in chapter 4. Resulting from the regularisation process, a large noise reduction can be obtained at the expense of field homogeneity. The inhomogeneous field produced is then processed using the 'phantom technique' described in Forbes *et al.* [31] to restore image quality. Finally, chapter 5 gives concluding remarks based on all that has preceded.

Chapter 2

Tikhonov Regularisation Approach for Designing Reduced Acoustic Noise Gradient Coils

2.1 Introduction

The primary requisite of any gradient coil system is that it must produce a linear field inside the target region (discussed in section 1.5.3). This chapter demonstrates a way to produce a sufficiently linear field for a gradient coil application while attempting to minimizing its acoustic noise output. The ill-conditioned matrix problem (arising from the lack of a unique current distribution that produces a specified magnetic field) is solved using Tikhonov regularisation with additional penalty terms aimed at minimizing the simulated noise generated. Other aspects considered in the model presented in the chapter are the smoothness of the current winding patterns and shielding the coil.

The switching of the gradient coils generates large Lorentz forces on the coil which cause the chamber to distort; the distortion promotes a pressure wave inside the chamber giving rise to acoustic noise. We have therefore taken the approach of minimizing the noise of the gradient coil through minimizing the deflection of the coil. This is accomplished by adding a displacement term in the regularisation process.

Yao *et al.* [116] confirmed that the primary source of acoustic noise is the vibration of the inner wall of the gradient chamber. Simulation results from their finite element model matched accurately with their experimental noise measurements from a gradient coil insert. They found that if the primary frequency of the switching function was close to a resonant vibration frequency of the coil, then large amplitude noise will be heard. The shape of the switching sequence has also been shown to be a factor in noise production; see Ichiki *et al.* [54].

Forbes *et al.* [30] presented a closed form solution to the mathematical problem of reducing the simulated acoustic noise generated by a gradient coil. These authors concentrated on the 'ramp-up' section of the switching function, using a cubic spline to take the magnetic field from 'off' to permanently 'on'. In the present chapter we extend the work of Forbes *et al.* [30] by factoring in the periodic nature of switching functions. We model the switching function as a full Fourier series, thereby permitting the generation of any number of periodic switching sequences. The time-dependent elastic motion of the coils (particularly when the period of switching is comparable to the time taken for an elastic wave to move along the coil) now become significant. We address this directly in this chapter and show how simulated acoustic effects result from resonance behaviour at certain switching frequencies.

In this chapter a standard framework for the following chapters is established.

Firstly, the geometrical model is discussed, along with a derivation of the distributed current flowing on the gradient coil. Next, the switching of the gradient coils (which plays a large role in the production of acoustic noise) is detailed. The foundation of the coil deflection and pressure wave models is presented next, and the solution process follows. Finally results are presented and conclusions are drawn.

The material presented in this chapter has been published as the paper [57]: J. Jackson, M. Brideson, L. Forbes, and S. Crozier. Tikhonov Regularization Approach to Acoustic Noise Reduction in an Asymmetric, Self-Shielded MRI Gradient Coil. *Concepts in Magn Reson B Magn Reson Eng*, 37B(3): 167-79, 2010.

2.2 The Geometry

A typical whole body gradient coil system is composed of a solid (e.g. fibre-glass reinforced epoxy) cylindrical housing in which is embedded a plurality of cylindrical layers including copper sheets for the x, y, and z primary coils, cooling pipes, insulation, and more copper sheets for the x, y, and z shield coils. In pursuing an analytical solution we have simplified the system to consider one primary-shield pair at a time, and ignore cooling, insulation, and non-copper housing. As such, the self-shielded gradient coil system is modelled as a solid cylindrical copper shell having an associated Young's modulus, $E = 1.3 \times 10^{10}\,\mathrm{Nm}^{-2}$ and Poisson's ratio, $\nu = 0.2$. The cylindrical shell has length $2L$ and thickness h. The primary windings lie at the interior radius a, and the shield windings lie at the external radius $b = a + h$. The midpoint radius $r_M = a + h/2$ will be the reference radius used in most computations to follow.

As the axis of the cylinder is horizontal, the standard Cartesian and cylindrical coordinate systems are rotated to match the geometry, as depicted in figure 2.1. The origin is positioned at the centre of the cylinder, such that the coil extends over the interval $-L \leq z \leq L$.

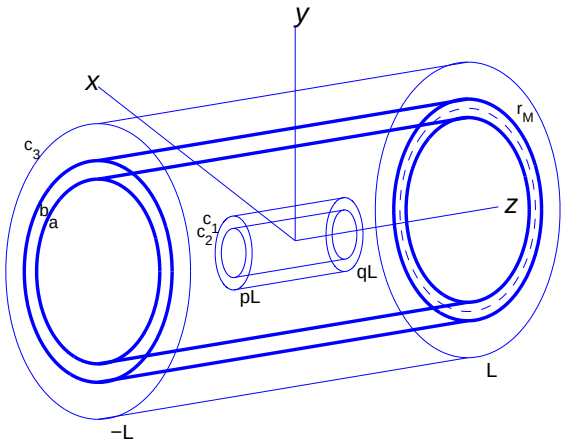

Figure 2.1: Schematic diagram of the self-shielded coil system and the target field regions. The dashed line indicates the midpoint of the primary and shield coil radius, $r_M = a + h/2$.

Three target cylinders of different length and radius have been specified, and are shown in figure 2.1. The two interior target cylinders form the basis for specifying the target field inside the DSV and the exterior cylinder is to force shielding. In this model each of the internal target cylinders is aligned co-axially with the main chamber and can be located asymmetrically with respect to the length of the coil. The asymmetrical nature is taken into account by defining the target fields on the interval $pL \leq z \leq qL$, where $-1 < p < q < 1$ and p and q are dimensionless constants. Defining asymmetrical target fields allows imaging of a region not centrally located within the chamber. As a special case, when $p = -q$, we have a symmetrical target field design.

A desired target field is specified on the surface of the target cylinders of radius

c_1 and c_2 to ensure the DSV has the appropriate gradient form. A shielding coil is included in this design, and for it to be effective, the target magnetic field is set to zero on the surface of the cylinder of radius c_3. An approach for shielding a gradient coil is put forth by Mansfield and Chapman [74]. Each primary and shield combination is designed to effectively cancel out stray fields external to the coil. Their model shifts each primary and shield current loop pair to roughly oppose each other, and thus minimize the external magnetic field.

2.3 Formulation

The mathematical design of the coil system is in common with Forbes *et al.* [30]. The magnetic induction field $\mathbf{B}$ can be found at any field point in space by use of the Biot-Savart Law. We assume the current to flow on both the inner and outer surfaces of the coil and define any current density as $\mathbf{j}(\theta', z') = j_\theta(\theta', z')\hat{\boldsymbol{e}}_\theta + j_z(\theta', z')\hat{\boldsymbol{e}}_z$. The induction field is related to the magnetic field by the equation $\mathbf{B} = \mu_0\mathbf{H}$, where μ_0 is the relative permeability of free space. We are primarily interested in the z component of the magnetic field,

$$\begin{aligned} H_z(r,\theta,z) \;=\; & -\frac{a}{2\pi}\int_{-L}^{L}\int_{0}^{2\pi} \frac{[r\cos(\theta'-\theta)-a]\, j_\theta^P(\theta',z') \quad d\theta' dz'}{[a^2+r^2-2ar\cos(\theta'-\theta)+(z'-z)^2]^{\frac{3}{2}}} \\ & -\frac{b}{2\pi}\int_{-L}^{L}\int_{0}^{2\pi} \frac{[r\cos(\theta'-\theta)-b]\, j_\theta^S(\theta',z') \quad d\theta' dz'}{[b^2+r^2-2br\cos(\theta'-\theta)+(z'-z)^2]^{\frac{3}{2}}} \;. \end{aligned} \tag{2.1}$$

In this expression j_θ^P and j_θ^S (Am^{-1}) are the respective azimuthal current density components on the primary and shield windings. These terms are related to j_z^P and j_z^S (the axial component of the current density) through the continuity equation $\mathrm{div}\,\mathbf{j}^P = 0$ on $r = a$ (and similarly on $r = b$ for the shielded case). It

follows from Carlson *et al.* [15] that both components of the primary and shield current densities can be obtained from stream functions Ψ^P and Ψ^S through $\mathbf{j} = \nabla \times (\Psi\,\hat{\mathbf{n}})$. For the primary coil, Forbes *et al.* [30] argued that the stream functions take the following form:

$$\begin{aligned}\Psi^P(\theta, z) \;&=\; -\sum_{n=1}^{N} \frac{2L}{n\pi} P_{0n}^P \cos\left(\frac{n\pi(z+L)}{2L}\right) \\ &+\quad \sum_{m=1}^{M}\sum_{n=1}^{N} \frac{2L}{n\pi}\left[P_{mn}^P \cos(m\theta) + Q_{mn}^P \sin(m\theta)\right] \sin\left(\frac{n\pi(z+L)}{2L}\right).\end{aligned} \tag{2.2}$$

A similar expression exists for the shield stream function $\Psi^S(\theta, z)$ with the corresponding coefficients P_{0n}^S, P_{mn}^S and Q_{mn}^S.

The azimuthal current density components required in equation (2.1) can be found from $j_\theta^P = \partial\Psi^P/\partial z$, giving

$$\begin{aligned}j_\theta^P(\theta, z) \;&=\; \sum_{n=1}^{N} P_{0n}^P \sin\left(\frac{n\pi(z+L)}{2L}\right) \\ &+\quad \sum_{m=1}^{M}\sum_{n=1}^{N} \left[P_{mn}^P \cos(m\theta) + Q_{mn}^P \sin(m\theta)\right] \cos\left(\frac{n\pi(z+L)}{2L}\right).\end{aligned} \tag{2.3}$$

The procedure to determine the primary Fourier coefficients P_{0n}^P, P_{mn}^P, Q_{mn}^P and their respective shield equivalents P_{0n}^S, P_{mn}^S and Q_{mn}^S will be described in section 2.7.

2.4 Switching Function

Each gradient coil is repeatedly being switched on and off for imaging purposes. Switching sequences are determined by the application and can be quite varied.

Our design requires switching functions representable by a Fourier series,

$$f_s(t) = W_0 + \sum_{k=1}^{K} W_k \cos\left(\frac{2\pi kt}{T}\right) + X_k \sin\left(\frac{2\pi kt}{T}\right),$$

with the coefficients W_0, W_k and X_k determined using the Euler equations. We consider two switching patterns. The first models the transition between on and off states with linear functions, and the second models the transition with modified cosine functions.

2.4.1 Ramp Wave

The Ramp Wave (dashed line, figure 2.2) is defined to be piecewise linear and continuous across a period T,

$$f_{s_{ramp}}(t) = \begin{cases} 0, & 0 < t \leq t_1 \\ \frac{1}{\tau}(t - t_1), & t_1 < t \leq t_1 + \tau \\ 1, & t_1 + \tau < t \leq 3t_1 + \tau \\ \frac{1}{\tau}(3t_1 - t) + 2, & 3t_1 + \tau < t \leq 3t_1 + 2\tau \\ 0, & 3t_1 + 2\tau < t \leq 4t_1 + 2\tau = T\ . \end{cases} \tag{2.4}$$

The time taken from $t = 0$ to the moment that 'charge up' begins is t_1, and the time taken to 'charge up' is τ. The 'charge down' process is symmetric so that the gradient coil spends equal time 'off' and 'on'. More specifically, the coil is on for $2t_1$ seconds, off for $2t_1$ seconds, and in between is charging up or down for τ seconds. By varying the two time scales, τ and T (the rise time and the length of the pulse respectively), any number of piecewise-linear switching patterns can be created.

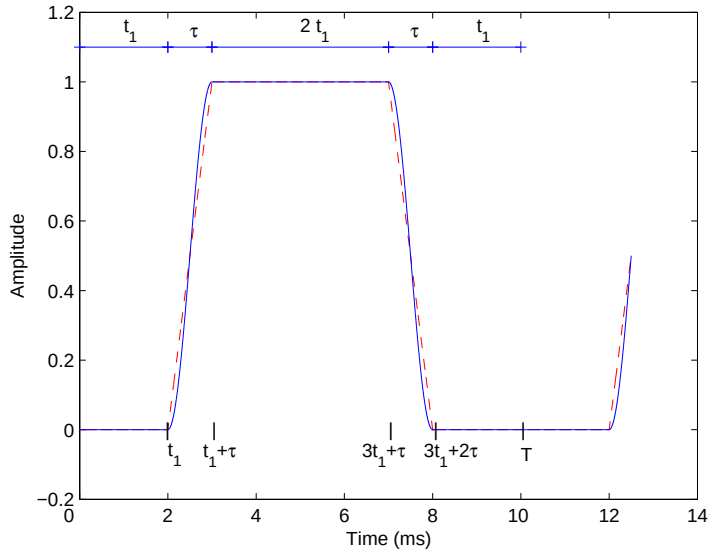

Figure 2.2: Ramp wave (dashed line) and Cosine wave (solid line) switching functions for $\tau = 0.001\,\mathrm{s}$ ($\omega = 6.28 \times 10^3\,\mathrm{Hz}$) and $T = 0.01\,\mathrm{s}$.

We define the fundamental frequency of the switching function as $\omega = 2\pi/\tau$. The time scale τ determines the cutoff frequency for quasi-stationary conditions. If $\tau < 0.11\,\mu\mathrm{s}$ or correspondingly if $\omega > 60$ MHz, phase retardation becomes important. Our assumed charge up time is $\tau = 1$ ms, ensuring ω is several orders of magnitude below the critical frequency. This relatively small value for ω allows us to assume a quasi-stationary system and make use of time independent forms for Maxwell's equations and the continuity equation.

2.4.2 Cosine Wave

A shortcoming of the Ramp wave definition is that it does not ensure continuity of the first derivative. To aid understanding of the behaviour of the coil system we defined a second switching function (solid line, figure 2.2) having continuity in the first derivative through modified cosine functions in the transition regions between the magnetic field being 'fully on' and 'fully off':

$$f_{s_{cosine}}(t) = \begin{cases} 0, & 0 < t \leq t_1 \\ \frac{1}{2}\left[1 + \cos\left(\frac{\pi}{\tau}(t - t_1 - \tau)\right)\right], & t_1 < t \leq t_1 + \tau \\ 1, & t_1 + \tau < t \leq 3t_1 + \tau \\ \frac{1}{2}\left[1 + \cos\left(\frac{\pi}{\tau}(t - 3t_1 - \tau)\right)\right], & 3t_1 + \tau < t \leq 3t_1 + 2\tau \\ 0, & 3t_1 + 2\tau < t \leq 4t_1 + 2\tau = T\ . \end{cases} \tag{2.5}$$

With convergence in mind, the Fourier series coefficients for the 'cosine' switching function will decay as $1/k^3$ compared with $1/k^2$ (see Kreyszig [62] section 10.2) for the 'ramp' switching function.

2.5 Coil Deflection

To calculate the deformation of the cylindrical shell by Lorentz forces, it is necessary to consider the Cauchy momentum equations which are highly non-linear even for Hookean materials. We have adopted a simplified version of the Cauchy equations of elasticity, cited in Boresi and Chong [9] p262, giving the linearised form proposed by Forbes *et al.* [30]:

$$\rho_c \frac{\partial^2 \mathbf{u}}{\partial t^2} = \frac{1}{h}(\mathbf{j} \times \mathbf{B}) + (\Lambda + G)\nabla(\nabla \cdot \mathbf{u}) + G\nabla^2 \mathbf{u}. \tag{2.6}$$

Here, G and Λ are Lamé coefficients determined from the Young's modulus and Poisson's ratio of the coil material. The self-shielded gradient coil system we are simulating comprises two thin conducting copper sheets firmly attached to an intermediary insulating layer. For simplicity of computation, the cylindrical coil system will be treated as a homogeneous copper shell having density $\rho_c =$

$8.99 \times 10^3\,\mathrm{kgm}^{-3}$. For all coil deflection calculations that follow we use a reference radius located at the midpoint between the primary and shield coils at radius $r_M = (a+b)/2$. Thus, our MRI scanner is moddeled as a vibrating 'thin walled' cylinder of radius $r = r_M$.

In keeping with the geometry, the displacement vector is defined in cylindrical coordinates as $\mathbf{u} = u_r\hat{\boldsymbol{e}}_r + u_\theta\hat{\boldsymbol{e}}_\theta + u_z\hat{\boldsymbol{e}}_z$. Using a small displacement approximation and assuming angular independence in u_θ and u_z, only the radial component u_r of the displacement vector is retained after the vector operations in (2.6).

A major distinction between this work and the work of Forbes *et al.* [30] is in the specification of the switching function. In the work by Forbes *et al.* [30], only a single switching event was considered, in which there was a rapid rise from zero to maximum current in a short time. The elastic response of the coil was supposed to be virtually instantaneous so that the second derivative on the left hand side of (2.6) was ignored in a quasi-static theory. However, in the present work, the switching function is periodic, and the second-order time derivative in (2.6) can not be ignored. Hence, the partial differential equation that models the time dependent deflection of the radial component u_r becomes

$$\rho_c \frac{\partial^2 u_r}{\partial t^2} + \frac{1}{r_M^2}(\Lambda + 2G)u_r - G\nabla^2 u_r = \frac{2B_{Z0}}{h}(j_\theta^P + j_\theta^S)\, f_s(t)\,. \tag{2.7}$$

Here, B_{Z0} denotes the strength of the background magnetic field in which the coil is immersed and is assumed to be static and uniform. The azimuthal and longitudinal deflection components u_θ and u_z have been ignored in this one-dimensional theory of deformation.

2.6 Pressure Waves and Noise

2.6.1 Pressure Wave and Boundary Conditions

To calculate the noise inside the chamber generated by the Lorentz forces it is necessary to determine the response of the air to the movement of the inner wall. The governing equations are conservation of mass, conservation of momentum and the isentropic gas relation as stated in the work of Forbes *et al.* [30]. The isentropic gas equation relates the pressure of the air inside the chamber, p_A, to the density of air inside the chamber, ρ_A. We follow the same linearisation process as outlined in Forbes *et al.* [30] to arrive at a wave equation for the pressure perturbation p_{A1} involving the isentropic sound speed c_{A0},

$$\frac{\partial^2 p_{A1}}{\partial t^2} \;=\; c_{A0}^2 \nabla^2 p_{A1}. \tag{2.8}$$

There are no initial conditions to consider as we assume the coil has been running long enough to render any initial effects insignificant.

To solve (2.8) for p_{A1}, we use u_r from (2.7) and the inner wall boundary condition

$$\frac{\partial p_{A1}}{\partial r} = -\rho_{A0} \frac{\partial^2 u_r}{\partial t^2} \qquad \text{on} \quad r = a. \tag{2.9}$$

Equation (2.9) requires the air inside the chamber to move with the inner wall of the gradient coil. The inner wall deflecting in the radial direction changes the interior volume of the gradient coil, which promotes the pressure wave. We assume our pressure wave is representable by a Fourier series and is thus repeated periodically in z, modelling an infinite length vibrating coil. Our infinite length pressure wave assumption ignores the open ended boundary conditions at $z = \pm L$,

imposed by our explicit finite length coil model. A method for accommodating open boundary conditions is described in the work of Shao and Mechefske [98], but is ignored in this chapter for simplicity.

2.6.2 Noise Level

Once the pressure perturbation, p_{A1}, has been calculated, the sound pressure level (SPL) inside the chamber can be estimated using

$$\mathrm{SPL} = 20 \log_{10} \left(\frac{|p_{A1}|}{p_{ref}} \right), \tag{2.10}$$

where the noise level is measured in decibels (dB(A)) and p_{ref} is taken to be $2 \times 10^{-5}\,\mathrm{Nm}^{-2}$. An objective A-weighted sound pressure level has been adopted as our weighting scale throughout this thesis to provide a common reference frame for all quoted noise levels.

2.7 Solution Process

2.7.1 Coil Deflection

Using the $\hat{\boldsymbol{e}}_\theta$-directed component of the primary coil current density in equation (2.3) and the equivalent expression for the shield coil current density, equation (2.7) can be solved for the radial displacement, u_r. We assume $u_r(\theta, z, t) = F(t)U_r(\theta, z)$, that is, the product of a static radial coil deflection $U_r(\theta, z)$, and a periodic temporal function $F(t)$. The temporal function is defined so that it can

be represented with an even Fourier series,

$$F(t) = \gamma_0 + \sum_{k=1}^{K} \gamma_k \cos\left(\frac{2\pi k t}{T}\right)$$

(similar in form to $f_s(t)$ but with different coefficients). It is useful to assume that the static coil deflection component has the form:

$$\begin{aligned} U_r(\theta, z) &= \sum_{n=1}^{N} A_{0n} \sin\left(\frac{n\pi(z+L)}{2L}\right) \\ &+ \sum_{m=1}^{M}\sum_{n=1}^{N} [A_{mn}(\cos m\theta) + B_{mn}\sin(m\theta)] \cos\left(\frac{n\pi(z+L)}{2L}\right). \end{aligned}$$

The expanded form for u_r becomes

$$\begin{aligned} u_r(\theta, z, t) &= \sum_{n=1}^{N} A_{0n0} \sin\left(\frac{n\pi(z+L)}{2L}\right) \\ &+ \sum_{m=1}^{M}\sum_{n=1}^{N} A_{mn0} \cos(m\theta) \cos\left(\frac{n\pi(z+L)}{2L}\right) \\ &+ \sum_{m=1}^{M}\sum_{n=1}^{N} B_{mn0} \sin(m\theta) \cos\left(\frac{n\pi(z+L)}{2L}\right) \\ &+ \sum_{n=1}^{N}\sum_{k=1}^{K} A_{0nk} \cos(k\omega t) \sin\left(\frac{n\pi(z+L)}{2L}\right) \\ &+ \sum_{m=1}^{M}\sum_{n=1}^{N}\sum_{k=1}^{K} A_{mnk} \cos(k\omega t)\cos(m\theta) \cos\left(\frac{n\pi(z+L)}{2L}\right) \\ &+ \sum_{m=1}^{M}\sum_{n=1}^{N}\sum_{k=1}^{K} B_{mnk} \cos(k\omega t)\sin(m\theta) \cos\left(\frac{n\pi(z+L)}{2L}\right) \end{aligned} \tag{2.11}$$

where $A_{mnk} \equiv \gamma_k A_{mn}$, $B_{mnk} \equiv \gamma_k B_{mn}$ $\forall$ m, n, k, and γ_k are the Fourier coefficients of the periodic temporal function $F(t)$ above. This six-termed expression is substituted into equation (2.7) and solved for the six coefficients by equating linearly independent terms. The coefficients are found in terms of the known coefficients W_0, W_k, and X_k (defining the temporal function) and P^P_{0n}, P^S_{0n}, P^P_{mn},

P^S_{mn}, Q^P_{mn}, and Q^S_{mn} (which are the spatial Fourier coefficients but are as yet still unknown). The relationship between coefficients can be shown to be

$$\begin{aligned}
A_{0n0} &= \frac{2B_{Z0}W_0(P^P_{0n}+P^S_{0n})}{h\left(\frac{1}{r_M^2}(\Lambda+2G)+G\left(\frac{n\pi}{2L}\right)^2\right)} \\
A_{0nk} &= \frac{2B_{Z0}W_k(P^P_{0n}+P^S_{0n})}{h\left(\frac{1}{r_M^2}(\Lambda+2G)-k^2\omega^2\rho_c+G\left(\frac{n\pi}{2L}\right)^2\right)} \\
A_{mn0} &= \frac{2B_{Z0}W_0(P^P_{mn}+P^S_{mn})}{h\left(\frac{1}{r_M^2}(\Lambda+2G)+m^2\frac{G}{r_M^2}+G\left(\frac{n\pi}{2L}\right)^2\right)} \\
A_{mnk} &= \frac{2B_{Z0}W_k(P^P_{mn}+P^S_{mn})}{h\left(\frac{1}{r_M^2}(\Lambda+2G)-k^2\omega^2\rho_c+m^2\frac{G}{r_M^2}+G\left(\frac{n\pi}{2L}\right)^2\right)} \\
B_{mn0} &= \frac{2B_{Z0}W_0(Q^P_{mn}+Q^S_{mn})}{h\left(\frac{1}{r_M^2}(\Lambda+2G)+m^2\frac{G}{r_M^2}+G\left(\frac{n\pi}{2L}\right)^2\right)} \\
B_{mnk} &= \frac{2B_{Z0}W_k(Q^P_{mn}+Q^S_{mn})}{h\left(\frac{1}{r_M^2}(\Lambda+2G)-k^2\omega^2\rho_c+m^2\frac{G}{r_M^2}+G\left(\frac{n\pi}{2L}\right)^2\right)} .
\end{aligned} \tag{2.12}$$

2.7.2 The Residual

The underdetermined nature of the problem precludes us from inverting the first kind integral equations in (2.1) to solve for unique j^P_θ and j^S_θ based on a desired H_z field. Instead, we consider a least squares approach to solve for the six sets of coefficients P^P_{0n}, P^S_{0n}, etc. We begin by substituting the Fourier series expressions for j^P_θ and j^S_θ into equation (2.1), arriving at the following reduced form for H_z

$$\begin{aligned}
H_z(r,\theta,z) &= -\sum_{n=1}^{N}\left(P^P_{0n}U_{0n}(r,z;a)+P^S_{0n}U_{0n}(r,z;b)\right) \\
&- \sum_{m=1}^{M}\sum_{n=1}^{N}\left[P^P_{mn}\cos(m\theta)+Q^P_{mn}\sin(m\theta)\right]U_{mn}(r,z;a) \\
&- \sum_{m=1}^{M}\sum_{n=1}^{N}\left[P^S_{mn}\cos(m\theta)+Q^S_{mn}\sin(m\theta)\right]U_{mn}(r,z;b).
\end{aligned} \tag{2.13}$$

The introduced coefficients U_{0n} and U_{mn} $(m \geq 1)$ are given below and are evaluated numerically using a 2D trapezoidal quadrature rule. They are

$$\begin{aligned} U_{0n}(r,z;a) &= \frac{a}{\pi}\int_{-L}^{L}\int_{0}^{\pi} \frac{\left[r\cos\theta' - a\right]\sin\left(\frac{n\pi(z'+L)}{2L}\right)\, d\theta' dz'}{\left[a^2+r^2-2ar\cos\theta'+(z-z')^2\right]^{3/2}} \\ U_{mn}(r,z;a) &= \frac{a}{\pi}\int_{-L}^{L}\int_{0}^{\pi} \frac{\left[r\cos\theta' - a\right]\cos(m\theta')\cos\left(\frac{n\pi(z'+L)}{2L}\right)\, d\theta' dz'}{\left[a^2+r^2-2ar\cos\theta'+(z-z')^2\right]^{3/2}} \,. \end{aligned}$$

The primary goal in our least squares approach is to match the target field at the inner radii c_1 and c_2, and give a null field at the external radius c_3. Defining residual terms as

$$\begin{aligned} &E_j(P^P_{0n}, P^S_{0n}, P^P_{mn}, P^S_{mn}, Q^P_{mn}, Q^S_{mn}) \quad = \\ &\int_{pL}^{qL}\int_{-\pi}^{\pi} \left[H_{TF}(c_j,\theta,z) - H_z(c_j,\theta,z)\right]^2 c_j\, d\theta\, dz, \qquad j = 1,2 \end{aligned} \tag{2.14}$$

where H_{TF} is our specified field or 'Target Field', and the external residual term as

$$E_3(P^P_{0n}, P^S_{0n}, P^P_{mn}, P^S_{mn}, Q^P_{mn}, Q^S_{mn}) = \int_{-L}^{L}\int_{-\pi}^{\pi} H_z^2(c_3,\theta,z)\, c_3\, d\theta\, dz\,, \tag{2.15}$$

we minimise the residuals with respect to the coefficients. Note that for E_3 we are only minimizing the z-directed magnetic field, as it has been demonstrated by Forbes and Crozier [34] that H_r and H_θ also are relatively small. In these three residual terms, H_z is calculated from equation (2.13).

These three terms alone do not improve the conditioning of the system, so we impose further restrictions. We are interested in minimizing the acoustic noise within the chamber, so minimizing the coil's deflection is an obvious choice for a

penalty regularisation term:

$$F_1(P_{0n}^P, P_{0n}^S, P_{mn}^P, P_{mn}^S, Q_{mn}^P, Q_{mn}^S) = \int_0^T \int_{-L}^{L} \int_{-\pi}^{\pi} u_r^2(\theta, z, t)\, r_M d\theta\, dz\, dt. \quad (2.16)$$

Here, we are concentrating on a reduction in the average acoustic noise level by reducing the average coil deflection over one period ($t \in [0, T]$). Also, following While *et al.* [114], we add extra penalty terms involving the curvature of the winding patterns on the primary and shield coils; these are

$$F_2(P_{0n}^P, P_{mn}^P, Q_{mn}^P) = \int_{-L}^{L} \int_{-\pi}^{\pi} |\nabla^2 \Psi^P(\theta, z)|^2\, a\, d\theta\, dz \quad \text{on } r = a, \quad (2.17)$$

$$F_3(P_{0n}^S, P_{mn}^S, Q_{mn}^S) = \int_{-L}^{L} \int_{-\pi}^{\pi} |\nabla^2 \Psi^S(\theta, z)|^2\, b\, d\theta\, dz \quad \text{on } r = b, \quad (2.18)$$

where the stream functions Ψ^P and Ψ^S, are found from equation (2.2). The functionals (2.14) - (2.18) are combined to form a total residual error functional for the coefficients P_{0n}^P, P_{0n}^S, P_{mn}^P, P_{mn}^S, Q_{mn}^P, and Q_{mn}^S of the form

$$R = E_1 + E_2 + E_3 + \lambda F_1 + \lambda_P F_2 + \lambda_S F_3\,. \quad (2.19)$$

The regularisation parameters λ, λ_P, and λ_S behave like Lagrange multipliers in optimisation problems, and their optimum values are determined by numerical experimentation. The Tikhonov regularisation method does not prescribe a way of finding λ, λ_P, and λ_S, and so these are found empirically; see Delves and Mohamed [22]. Each nonnegative parameter adds influence to its associated integral and impacts on the goodness-of-fit of the fields through E_1, E_2 and E_3. Each functional is quadratic in nature and this process is referred to as Tikhonov regularisation by Neittaanmaki *et al.* [89]. To optimise our system with respect to the unknown

Fourier coefficients, we require a simultaneous solution to

$$\begin{aligned} &\frac{\partial R}{\partial P_{0n}^P} = 0, \quad \frac{\partial R}{\partial P_{mn}^P} = 0, \quad \frac{\partial R}{\partial Q_{mn}^P} = 0, \\ &\frac{\partial R}{\partial P_{0n}^S} = 0, \quad \frac{\partial R}{\partial P_{mn}^S} = 0, \quad \frac{\partial R}{\partial Q_{mn}^S} = 0, \\ &\qquad \text{for} \quad n = 1, ..., N, \quad m = 1, ..., M. \end{aligned} \tag{2.20}$$

Each of the $4MN + 2N$ equations in (2.20) is linear in the Fourier coefficients (because each functional is quadratic in the Fourier coefficients). This system is most easily solved in block matrix form. For example, when considering a y-gradient we are only concerned with the Q_{1n}^P and Q_{1n}^S coefficients, and the block matrix equation, for each n, reduces to

$$\begin{bmatrix} G_{1y}^{aa} & G_{1y}^{ab} \\ G_{1y}^{ba} & G_{1y}^{bb} \end{bmatrix} \begin{bmatrix} Q_{1n}^P \\ Q_{1n}^S \end{bmatrix} = \begin{bmatrix} H_{1y}^a \\ H_{1y}^b \end{bmatrix} . \tag{2.21}$$

The components of the square block matrix are

$$\begin{aligned} G_{1y}^{aa} &= \int_{pL}^{qL} \left(U_{1n}^2(c_1, z; a)\, c_1 + U_{1n}^2(c_2, z; a)\, c_2 \right)\, dz + \int_{-L}^{L} U_{1n}^2(c_3, z; a)\, c_3\, dz \\ &+ \lambda\, r_M \frac{8\pi L B_{Z0}^2 W_0^2}{\omega h^2 \left(\frac{1}{r_M^2} (\Lambda + 2G) + \frac{G}{r_M^2} + G \left(\frac{n\pi}{2L} \right)^2 \right)^2} \\ &+ \lambda\, r_M \sum_{k=1}^{K} \frac{4\pi L B_{Z0}^2 W_k^2}{\omega h^2 \left(\frac{1}{r_M^2} (\Lambda + 2G) - k^2 \omega^2 \rho_c + \frac{G}{r_M^2} + G \left(\frac{n\pi}{2L} \right)^2 \right)^2} \\ &+ \lambda_P \left(\frac{n\pi}{2L} + \frac{2L}{n\pi a^2} \right)^2 La \ , \end{aligned}$$

$$
\begin{aligned}
G_{1y}^{ab} &= G_{1y}^{ba} \\
&= \int_{pL}^{qL} \left(U_{1n}(c_1,z;a)U_{1n}(c_1,z;b)\,c_1 + U_{1n}(c_2,z;a)U_{1n}(c_2,z;b)\,c_2\right)\,dz \\
&+ \int_{-L}^{L} U_{1n}(c_3,z;a)U_{1n}(c_3,z;b)\,c_3\,dz \\
&+ \lambda\, r_M \frac{8\pi L B_{Z0}^2 W_0^2}{\omega h^2\left(\frac{1}{r_M^2}\left(\Lambda+2G\right)+\frac{G}{r_M^2}+G\left(\frac{n\pi}{2L}\right)^2\right)^2} \\
&+ \lambda\, r_M \sum_{k=1}^{K} \frac{4\pi L B_{Z0}^2 W_k^2}{\omega h^2\left(\frac{1}{r_M^2}\left(\Lambda+2G\right)-k^2\omega^2\rho_c+\frac{G}{r_M^2}+G\left(\frac{n\pi}{2L}\right)^2\right)^2}\ ,
\end{aligned}
$$

$$
\begin{aligned}
G_{1y}^{bb} &= \int_{pL}^{qL} \left(U_{1n}^2(c_1,z;b)\,c_1 + U_{1n}^2(c_2,z;b)\,c_2\right)dz + \int_{-L}^{L} U_{1n}^2(c_3,z;b)\,c_3\,dz \\
&+ \lambda\, r_M \frac{8\pi L B_{Z0}^2 W_0^2}{\omega h^2\left(\frac{1}{r_M^2}\left(\Lambda+2G\right)+\frac{G}{r_M^2}+G\left(\frac{n\pi}{2L}\right)^2\right)^2} \\
&+ \lambda\, r_M \sum_{k=1}^{K} \frac{4\pi L B_{Z0}^2 W_k^2}{\omega h^2\left(\frac{1}{r_M^2}\left(\Lambda+2G\right)-k^2\omega^2\rho_c+\frac{G}{r_M^2}+G\left(\frac{n\pi}{2L}\right)^2\right)^2} \\
&+ \lambda_S \left(\frac{n\pi}{2L}+\frac{2L}{n\pi b^2}\right)^2 Lb\ , \\
H_{1y}^{a} &= -\int_{pL}^{qL} \frac{H_{max}}{c_1}\left(U_{1n}(c_1,z;a)\,c_1^2 + U_{1n}(c_2,z;a)\,c_2^2\right)\,dz\ , \\
H_{1y}^{b} &= -\int_{pL}^{qL} \frac{H_{max}}{c_1}\left(U_{1n}(c_1,z;b)\,c_1^2 + U_{1n}(c_2,z;b)\,c_2^2\right)\,dz\ .
\end{aligned}
$$

Other regularisation terms were considered, however, they were not carried out in the optimised system. Considering a maximum radial displacement penalty function (by use of an absolute value metric for example) has the potential to reduce the loud acoustic noises heard during the scanning process but different regularisation techniques would need to be employed.

A natural question to ask at this stage is why not minimise the acoustic noise directly? Why minimise the deflection which leads to a reduced pressure pertur-

bation which then leads to a reduced acoustic noise output? This approach can certainly be taken. Adding a regularisation term relating to the SPL (found in equation (2.10)) in residual system (2.19) would accomplish this goal. However, due to the logarithmic definition of the SPL this would not yield a quadratic term in the Fourier coefficients and a non-Tikhonov regularisation method would need to be used to condition the system adequately.

A drawback of the Tikhonov regularisation process is the unavoidable trial and error nature of the solution process. Essentially, the method becomes a game whereby searching for λ values does not yield a unique optimum, or even a prescribe a direction to head in for the next set of λ choices. Techniques involving SVD or iterative methods (see Liu and Han [73]) present theoretically elegant solution procedures for illconditioned problems of this sort of nature but were not considered here.

2.7.3 Pressure Wave and Acoustic Noise

With the boundary condition (2.9) in mind, we assume that the air pressure inside the chamber has the following form:

$$\begin{aligned} p_{A1}(r,\theta,z,t) &= \sum_{n=1}^{N} E_{0n0}(r)\sin\left(\frac{n\pi(z+L)}{2L}\right) \\ &+ \sum_{m=1}^{M}\sum_{n=1}^{N} E_{mn0}(r)\cos(m\theta)\cos\left(\frac{n\pi(z+L)}{2L}\right) \\ &+ \sum_{m=1}^{M}\sum_{n=1}^{N} F_{mn0}(r)\sin(m\theta)\cos\left(\frac{n\pi(z+L)}{2L}\right) \\ &+ \sum_{n=1}^{N}\sum_{k=1}^{K} E_{0nk}(r)\cos(k\omega t)\sin\left(\frac{n\pi(z+L)}{2L}\right) \\ &+ \sum_{m=1}^{M}\sum_{n=1}^{N}\sum_{k=1}^{K} E_{mnk}(r)\cos(k\omega t)\cos(m\theta)\cos\left(\frac{n\pi(z+L)}{2L}\right) \\ &+ \sum_{m=1}^{M}\sum_{n=1}^{N}\sum_{k=1}^{K} F_{mnk}(r)\cos(k\omega t)\sin(m\theta)\cos\left(\frac{n\pi(z+L)}{2L}\right). \end{aligned} \tag{2.22}$$

Substituting into the wave equation (2.8) and comparing linearly independent terms, we deduce expressions for E_{0n0}, E_{mn0}, ... , F_{mnk}. Considering only E_{0n0} and E_{mnk}, for brevity, we obtain the modified Bessel equations

$$\begin{aligned} \frac{1}{r}\frac{\partial}{\partial r}\left(r\frac{\partial E_{0n0}}{\partial r}\right) - \frac{n^2\pi^2}{4L^2}E_{0n0} &= 0, \\ \frac{1}{r}\frac{\partial}{\partial r}\left(r\frac{\partial E_{mnk}}{\partial r}\right) - \left(\frac{m^2}{r^2} + \frac{n^2\pi^2}{4L^2} - \frac{k^2\omega^2}{c_{A0}^2}\right)E_{mnk} &= 0. \end{aligned}$$

These lead to solutions for E_{0n0} and E_{mnk} involving modified Bessel functions of order 0 and m respectively,

$$E_{0n0} = m_{0n0} I_0 \left(r \frac{n\pi}{2L} \right), \tag{2.23}$$

$$E_{mnk} = m_{mnk} I_m \left(r \sqrt{\frac{n^2\pi^2}{4L^2} - \frac{k^2\omega^2}{c_{A0}^2}} \right). \tag{2.24}$$

Here, the notation $I_m(x)$ denotes the modified Bessel function of the first kind of order m following notation from Abramowitz and Stegun [1].

With the coefficients expressed as in (2.23) and (2.24), the expanded form of (2.22) can now be substituted into the left hand side of the boundary condition (2.9). On the right hand side, we substitute (2.11), giving

$$\begin{aligned} \frac{\partial p_{A1}}{\partial r} &= \rho_{A0} \sum_{n=1}^{N} \sum_{k=1}^{K} k^2\omega^2 A_{0nk} \cos(k\omega t) \sin\left(\frac{n\pi(z+L)}{2L} \right) \\ &+ \rho_{A0} \sum_{m=1}^{M} \sum_{n=1}^{N} \sum_{k=1}^{K} k^2\omega^2 A_{mnk} \cos(k\omega t) \cos(m\theta) \cos\left(\frac{n\pi(z+L)}{2L} \right) \\ &+ \rho_{A0} \sum_{m=1}^{M} \sum_{n=1}^{N} \sum_{k=1}^{K} k^2\omega^2 B_{mnk} \cos(k\omega t) \sin(m\theta) \cos\left(\frac{n\pi(z+L)}{2L} \right). \end{aligned}$$

Again, equating linearly independent terms gives a reduced form for each coefficient. In the case of the E_{0n0} and E_{mnk}, we have

$$\begin{aligned} \frac{\partial E_{0n0}(r)}{\partial r} &= 0 \quad \text{on } r = a, \\ \frac{\partial E_{mnk}(r)}{\partial r} &= \rho_{A0} k^2\omega^2 A_{mnk} \quad \text{on } r = a. \end{aligned}$$

Finally, the general expression for the pressure wave inside the chamber is

$$\begin{aligned} p_{A1}(r,\theta,z,t) &= \sum_{n=1}^{N}\sum_{k=1}^{K} \rho_{A0}k^2\omega^2 \frac{A_{0nk}I_0(rT_{nk})}{T_{nk}I_0'(aT_{nk})}\cos(k\omega t)\sin\left(\frac{n\pi(z+L)}{2L}\right) \\ &+ \sum_{m=1}^{M}\sum_{n=1}^{N}\sum_{k=1}^{K} \rho_{A0}k^2\omega^2 \frac{A_{mnk}I_m(rT_{nk})}{T_{nk}I_m'(aT_{nk})}\cos(k\omega t)\cos(m\theta)\cos\left(\frac{n\pi(z+L)}{2L}\right) \\ &+ \sum_{m=1}^{M}\sum_{n=1}^{N}\sum_{k=1}^{K} \rho_{A0}k^2\omega^2 \frac{B_{mnk}I_m(rT_{nk})}{T_{nk}I_m'(aT_{nk})}\cos(k\omega t)\sin(m\theta)\cos\left(\frac{n\pi(z+L)}{2L}\right), \end{aligned} \tag{2.25}$$

where

$$I_m'(aT_{nk}) = \frac{\partial}{\partial\beta}I_m(\beta)|_{\beta=aT_{nk}} \quad \text{and} \quad T_{nk} = \sqrt{\frac{n^2\pi^2}{4L^2} - \frac{k^2\omega^2}{c_{A0}^2}} \tag{2.26}$$

have been defined for convenience.

Taking the reference air pressure to be $p_{ref} = 2\times10^{-5}\,\mathrm{Nm}^{-2}$, it becomes trivial to evaluate the noise level inside the chamber by substituting the above expression into equation (2.10).

2.8 Results

Here, we limit our analysis to a y-gradient design but the x-gradient analysis is analogous. Several simplifications can be made to analyse a z-gradient coil. The dimensions of our illustrative y-gradient coil mimic those capable of full human body scans. The primary and shield coils are of length $L = 1\,\mathrm{m}$ and of radius $a = 0.3\,\mathrm{m}$ and $b = \frac{4}{3}a = 0.4\,\mathrm{m}$, respectively. The two inner target fields are set at radii $c_1 = 0.2\,\mathrm{m}$ and $c_2 = 0.1\,\mathrm{m}$, and are longitudinally asymmetric with $p = -0.7$ and $q = 0.1$ where $z \in [pL, qL]$. The third target field is located at

$c_3 = \frac{3}{2}b = 0.6\,\mathrm{m}$ and extends the full length of the coil. The coil is immersed in a background magnetic field of strength $B_{Z0} = 2\,\mathrm{T}$, and the small variations caused by the gradient fields have a maximum of $B_{grad} = 0.02\,\mathrm{T}$.

2.8.1 MRI design analysis

In minimising the residual (2.19), our primary design concern is to produce an accurate match with the desired target fields. As secondary concerns, we desire the deflection of the coil to be reduced (which will in turn reduce the noise level inside the chamber) and the shape of the current windings on the bore of the coil to be smooth enough to facilitate construction. This requires a delicate balance of the regularisation parameter values. The chosen values must give an acceptable level of conditioning to the block matrix equation (2.21), and they must also produce satisfactory results in terms of achieving our primary and secondary design concerns.

In figure 2.3, we present results showing how different parameter values can affect the system. With λ_P and λ_S held constant it can be seen that when the value of λ is changed from 10^0 to 10^{21}, coil deflection is reduced but at the expense of target field matching. To arrive at optimum values for the regularisation parameters, we empirically searched for values that balanced the influence of the three penalty terms, and settled on the values $\lambda = 10^{21}$, $\lambda_P = 10^{-7}$, and $\lambda_S = 10^{-7}$.

Despite the apparent large change in coil deflection and the change in shape of the B_z profile, the field matching at c_1, c_2, and c_3 was still adequate in the example above. In the inner target region $-c_2 \leq y \leq c_2$, the maximum deviation between the computed B_z field and the target field was 3.6%, and in the outer region $-c_1 \leq y \leq c_1$, it rises to 4.5%. These discrepancies remain within the

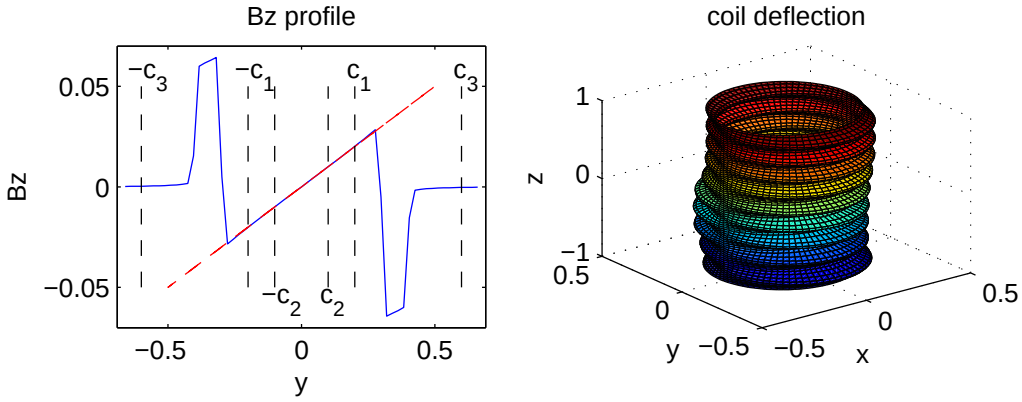

(a) $\lambda = 10^0$

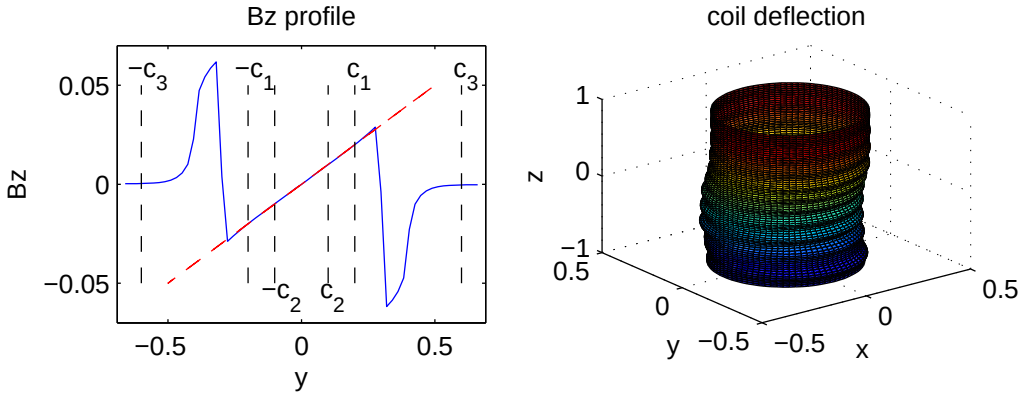

(b) $\lambda = 10^{21}$

Figure 2.3: To the left are profiles of B_z computed as a function of y at $x = 0$ and $z = (p + q)L/2$; the y-gradient target field (dashed line) is overlayed for comparison. To the right are plots giving the maximum coil deflection, overlayed on a cylinder of radius a and scaled by 10^4 for ease of visualisation. Plots are given for (a) $\lambda = 1$ and (b) $\lambda = 10^{21}$, for $\lambda_P = \lambda_S = 10^{-7}$.

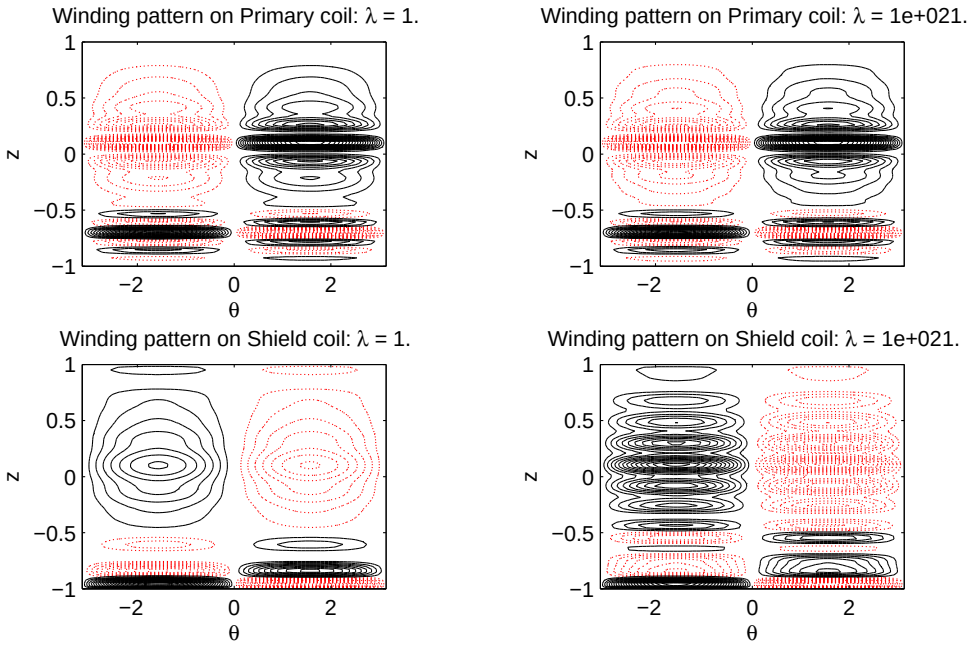

(a) $\lambda = 10^0$ (b) $\lambda = 10^{21}$

Figure 2.4: (a) Primary and Shield winding patterns for $\lambda = 10^0 = 1$, and (b) Primary and Shield windings for $\lambda = 10^{21}$. Dashed windings indicate windings in which the current direction is reversed.

typical limit of 5% maximum gradient deviation, reported in Haacke *et al.* [45]. With target field matching the overriding concern, the reductions in deflection translated to a maximum reduction in SPL of 0.6 dB. Qualitatively, these results compare well with those of Forbes *et al.* [30], but quantitatively the reduction in SPL is not as large.

Contours of the primary and shield stream functions (found in equation (2.2)) for $\lambda = 10^0$ and $\lambda = 10^{21}$ are shown in figure 2.4. The dashed contours in each graph denote reverse windings in which the current is negative. From figure 2.4, we see the required asymmetrical target field is created from densely wrapped, opposing windings located at pL and qL in the z direction.

The horizontal axes in figure 2.4 correspond to the azimuthal angle θ, so each

winding pattern is visualised as wound around a cylinder of the required radius. The direction of the current in the shield roughly opposes the current in the primary coil; thus, each winding pattern forms a Golay coil (see Golay coil section 1.4.3).

As λ increases from 10^0 to 10^{21}, we notice, in contrast to Forbes *et al.* [30], minor changes in the primary winding pattern, which is reflected by the relatively small reduction in simulated acoustic noise. When λ is increased beyond 10^{21} we see sections of the coil containing dense localised opposing windings, similar to Forbes *et al.* [30], which leads to further reductions in simulated acoustic noise; however, a poor replication of the desired target field is produced.

2.8.2 Analysis of the switching frequency ω

Inspection of equation (2.25) reveals that the dependence of the pressure wave amplitude on the switching frequency ω is compounded by the appearance of ω in T_{nk} and the coefficients A_{0nk}, A_{mnk}, and B_{mnk} in equations (2.12). Figure 2.6(a) suggests that, as a general trend, the higher the switching frequency, the louder the noise heard by the patient. In addition, the form of these implicit dependencies suggests that resonances might exist. Indeed, with careful convergence and limit analysis, we are able to predict the location of resonances. For example, when considering the y-gradient, we see that

$$B_{1nk} \;\to\; \infty \qquad \text{when} \qquad \omega_{n,k} \;\to\; \sqrt{\frac{\frac{1}{r_M^2}(\Lambda + 2G) + \frac{G}{r_M^2} + G\left(\frac{n\pi}{2L}\right)^2}{\rho_c k^2}}$$

and a primary resonance exists at $\omega = \omega_{1,1} = 4.418\,\text{kHz}$. At some frequencies, the singularities are removable and resonance does not occur. However, at many

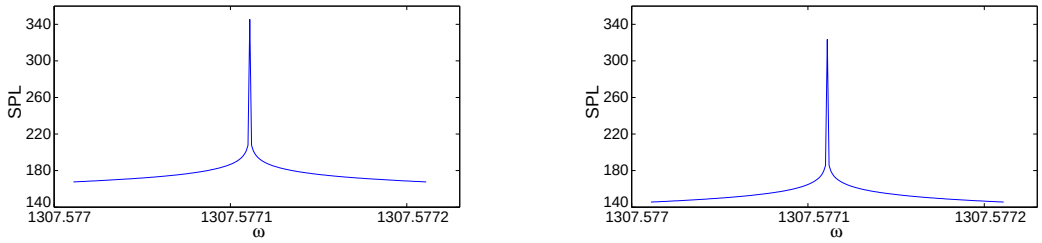

(a) Ramp at $\omega_{9,9}$ (b) Cosine at $\omega_{9,9}$

Figure 2.5: SPL response of the y-gradient coil in the neighbourhood of the resonance at $\omega_{9,9} = 1.308\,\text{kHz}$. (a) uses the Ramp switching function and (b) uses the Cosine switching function.

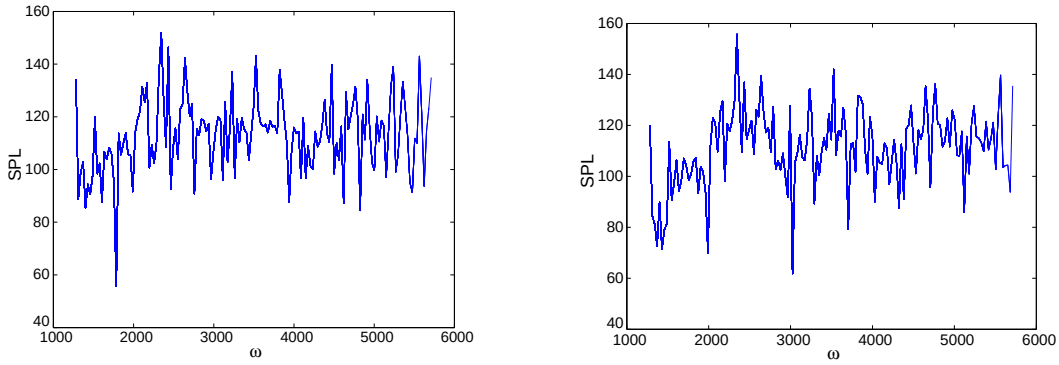

(a) Ramp (b) Cosine

Figure 2.6: SPL-frequency spectrums for the y-gradient coil using (a) the Ramp switching function and (b) the Cosine switching function. SPL values are computed when the gradient coil's field is at a maximum.

frequencies, the singularity can lead to a resonance, resulting in a catastrophically high SPL. Typically, these resonances have an extremely high Q-factor (figure 2.5) and would be difficult to reproduce in a clinical MRI machine.

The form the switching function takes also has an impact on the SPL frequency response of the coil system. Figure 2.6 shows the frequency spectrum of SPL values computed with the coil 'on' for the Ramp and Cosine switching functions. As expected, the Fourier coefficients of the smooth Cosine switching function converge faster resulting in a damping of the average SPL value; for example, the $\omega_{9,9}$ resonance peak at 1.308 kHz reduced the SPL by 22 dB.

2.9 Conclusions

We have presented a Tikhonov regularisation solution to the inverse problem of designing self-shielded gradient coils that produce a desired target field whilst (1) minimizing simulated acoustic noise due to structure movement resulting from Lorentz forces, and (2) encouraging smoothness of the coil winding pattern. A simplified (linearised, one dimensional) model for the coil's behaviour was adopted to facilitate closed-form expressions. Despite the simplifications, qualitative comparisons between our results and the literature were encouraging; see Forbes *et al.* [30].

Not so encouraging was the clinically insignificant maximum SPL reduction of only 0.6 dB for a shielded y-gradient coil. Nevertheless, this work has demonstrated the effects of including realistic MR switching sequences, and accounting for the possibility of resonances, which occur when portions of the switching signal occur on a comparable time scale to the time taken for an elastic wave to traverse the coil longitudinally.

An interesting outcome from the switching function analysis is the suggestion that lower SPL output might be obtainable by considering smoother switching functions. Sequences suggested by Idiyatullin *et al.* [55], although not smooth, lead to theoretically reduced noise outputs whilst also minimising scanning times. Practical switching functions can have a complicated piecewise linear form with long off periods and inverted signals; see Haacke *et al.* [45]. As a Fourier Series will converge faster for a smooth function, changing the linear ramps to cosine ramps may produce a damping of the SPL, as was shown here.

Further extensions of this research are to assume a three dimensional coil deflection model. In the next chapter we test whether the radial deflection is the

primary cause of simulated acoustic noise by considering azimuthal and longitudinal deformation effects. Another addition to our problem is dropping our assumption of a pressure wave along a coil of notionally infinite length. It has been suggested when the pressure wave reaches the open boundaries (at $z = \pm L$) significant effects may arise. We look at the challenging problem of accounting for end effects on the pressure wave in the next chapter.

Chapter 3

An Extended Deformation Model and Pressure Wave Analysis

3.1 Introduction

Chapter 2 presented a linearised one dimensional coil deflection model and showed, using a Tikhonov regularisation approach, that a small noise reduction was achievable. We extend this first attempt by developing a complete three dimensional coil deflection model. Li *et al.* [70] assumed a three dimensional coil deflection model and presented a modal analysis of the structural deformation and acoustic pressure wave. They found, for certain modes, that structural-acoustic mode coupling can occur, which leads to higher than average noise levels in the chamber. A paper published by Mechefske and Wang [85] concludes that, under typical (low) switching frquenices for a gradient coil, the bending modes are predominately made up of linear combinations of the radial vibration and beam type vibrations. Furthermore they assert that it is a direct or indirect result of the coil deformations that leads to acoustic noise.

Further extensions of the work in chapter 2 include consideration of a finite length pressure wave by introducing boundary conditions to model the open ends. Zorumski [120] was one of the first to develop a successful analytical approach. He solved the general problem of radiation from a cylindrical (or annular duct) by impedance matching at the open ends. A complex expression for the pressure wave at the open end of the duct is then derived from an eigenfunction expansion of Helmholtz' equation.

A comprehensive paper by Kuijpers *et al.* [63] presented a semi-analytical solution for the gradient coil acoustic problem, with the model evolving from a simple infinite duct to a finite duct with vibrating walls and infinite baffles. Mechefske *et al.* [86] solved for the Lorentz force in a finite-length cylinder using a finite element model, then solved for the simulated acoustic noise distribution in the chamber with a boundary element model applied to the Kirchhoff-Helmholtz integral equation. Qualitatively, their simulation results compared well against sound pressure level (SPL) measurements within a 4 T whole body scanner, with particularly good quantitative agreement near the isocentre of the chamber. A subsequent paper by Shao and Mechefske [98] considered the finite duct model as a "virtually closed cavity". Their use of Green's functions to solve the Kirchhoff-Helmholtz integral equation resulted in a computationally more efficient algorithm, but discrepancies still existed near the open ends when compared with boundary element method results. In looking to account properly for the open ends, some traction may be gained in treating them as ring sources. The number of publications on acoustic ring sources is small, but Carley [14] recently presented a simple series solution based on Hypergeometric functions.

Incorporating a higher dimensional deflection representation into the model outlined in chapter 2 complicates the expression of the residual system; however, the

actual mathematics and solution process are left much the same. The geometric coil model, switching function, and current density expressions are identical to those used in chapter 2 but are restated in this chapter for completeness. The coil deflection and pressure wave analysis are, however, significantly more complex and are discussed in detail. Results are presented so that a comparison between i) the one dimensional deflection model (presented in chapter 2) and the three dimensional deflection model (presented here), and ii) the infinite pressure wave (which is the homogeneous part of the pressure wave solution derived in this chapter) and the finite pressure wave (which is the total pressure wave presented) can be made.

The material for this chapter has been submitted to the journal Concepts in Magnetic Resonance Imaging Part B: Magnetic Resonance Engineering and is in the peer review stage. It is entitled 'An Extended Deformation Model and Pressure Wave Analysis for a Gradient Coil in an MRI Application' and is authored by James M. Jackson, Michael A. Brideson, Larry K. Forbes and Stuart Crozier.

3.2 The Geometry

A standard gradient coil system is comprised of a solid cylindrical fibreglass shell with six cylindrical copper sheets embedded within. The copper sheets are arranged into x, y, and z-primary coils, an intermediary insulating layer, then x, y, and z-shield coils. The distributed current is contained between etchings in the copper sheets. The magnetic field is obtained from superposition of each coil's field.

To obtain an analytical solution we consider a simplified gradient coil system in

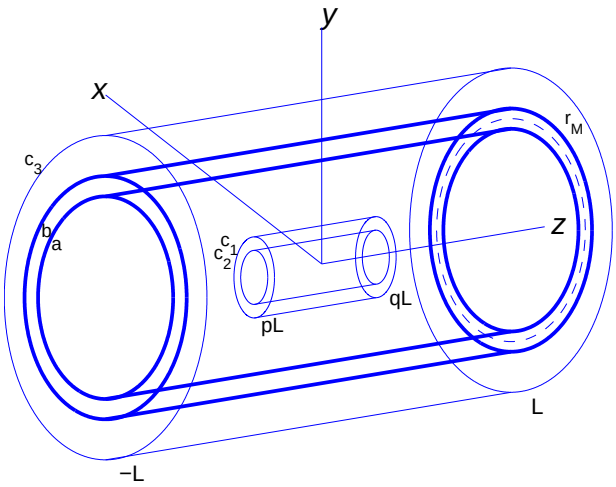

Figure 3.1: Schematic diagram of a self-shielded gradient coil system and the target field regions. The dashed line indicates the midpoint of the primary and shield coil radius, $r_M = a + h/2$.

which the fibreglass shell and insulating layer are ignored. As such, we model the coil system as a homogeneous structure having an associated Young's Modulus E and Poisson's ratio ν. Our formal model is schematically represented in figure 3.1. The chamber has length $2L$, inner (primary) radius a and outer (shield) radius b. This gives a coil of thickness $h = b - a$ and a midpoint radius of $r_M = a + h/2$ which serves as the reference radius for most calculations that follow. We assume all the primary coils lie at the same radius, $r = a$, and similarly, all the shield windings lie at $r = b$.

The standard Cartesian coordinate system has its origin set to the centre of the chamber, the z-axis aligned with the axis of symmetry, the y-axis directed vertically, and the x-axis parallel to the floor. This choice permits an easy interchange with the more natural standard cylindrical polar coordinate system.

Our solution process requires specifying the magnetic field on the surface of three

target cylinders, aligned co-axially with the chamber as depicted in figure 3.1, and is consistent with chapter 2. The gradient magnetic field in the DSV is specified on the two internal target cylinders, while the outer target cylinder facilitates shielding of the magnetic field external to the MRI structure.

To enable imaging of a region not centrally located within the chamber, the two internal target cylinders, of radii c_1 and c_2, are located over an asymmetric interval $pL \leq z \leq qL$. Here, p and q are dimensionless constants where $-1 < p < q < 1$ (with the symmetric case occurring when $p = -q$). On the external target cylinder of radius c_3, we specify the null magnetic field to ensure shielding is as effective as possible.

3.3 Formulation

We assume a 'thin walled' gradient coil model where current flows on both sides of the primary and shield coil. The current density vector has the form $\mathbf{j}(\theta', z') = j_\theta(\theta', z')\hat{\boldsymbol{e}}_\theta + j_z(\theta', z')\hat{\mathbf{e}}_z$ and the spatial distribution of the magnetic induction field, $\mathbf{B}$, is determined from the Biot-Savart Law. We are primarily interested in the axial component of the magnetic induction field which is given by

$$\begin{aligned} B_z(r,\theta,z) &= -\frac{\mu_0 a}{2\pi}\int_{-L}^{L}\int_0^{2\pi} \frac{\left[r\cos(\theta'-\theta)-a\right] j_\theta^P(\theta', z')}{\left[a^2+r^2-2ar\cos(\theta'-\theta)+(z'-z)^2\right]^{\frac{3}{2}}} d\theta' dz' \\ &- \frac{\mu_0 b}{2\pi}\int_{-L}^{L}\int_0^{2\pi} \frac{\left[r\cos(\theta'-\theta)-b\right] j_\theta^S(\theta', z')}{\left[b^2+r^2-2br\cos(\theta'-\theta)+(z'-z)^2\right]^{\frac{3}{2}}} d\theta' dz', \quad (3.1) \end{aligned}$$

where j_θ^P and j_θ^S (Am^{-1}) are the azimuthal current densities on the primary and shield coils respectively and μ_0 is the permeability of free space.

Brideson *et al.* [11] have shown that the current density components can be derived

from the stream function through $j_\theta = \partial\Psi/\partial z$ and $r\, j_z = -\partial\Psi/\partial\phi$, although j_z is not required as it does not contribute to B_z. Forbes *et al.* [30] argue that the stream function on the primary coil takes the form

$$\begin{aligned}\Psi^P(\theta,z) &= -\sum_{n=1}^{N}\frac{2L}{n\pi}P_{0n}^P\cos\left(\frac{n\pi(z+L)}{2L}\right)\\ &+ \sum_{m=1}^{M}\sum_{n=1}^{N}\frac{2L}{n\pi}\left[P_{mn}^P\cos(m\theta)+Q_{mn}^P\sin(m\theta)\right]\sin\left(\frac{n\pi(z+L)}{2L}\right) \quad (3.2)\end{aligned}$$

leading to

$$\begin{aligned}j_\theta^P(\theta,z) &= \sum_{n=1}^{N}P_{0n}^P\sin\left(\frac{n\pi(z+L)}{2L}\right)\\ &+ \sum_{m=1}^{M}\sum_{n=1}^{N}\left[P_{mn}^P\cos(m\theta)+Q_{mn}^P\sin(m\theta)\right]\cos\left(\frac{n\pi(z+L)}{2L}\right). \quad (3.3)\end{aligned}$$

Equations (3.2) and (3.3) have shield analogues with all the P superscripts replaced with S superscripts. The Fourier coefficients P_{0n}^P, P_{0n}^S, P_{mn}^P, P_{mn}^S, Q_{mn}^P, and Q_{mn}^S are as yet unknown and a regularizing approach is used to determine them.

3.4 Switching Function

The switching function for a gradient coil affects the amplitude of the acoustic noise (Yao *et al.* [116]). Gradient coil pairs (primary and shield combinations) are sequentially turned on and off to aid the algorithmic construction of a two dimensional image. Our model assumes a general switching function with the

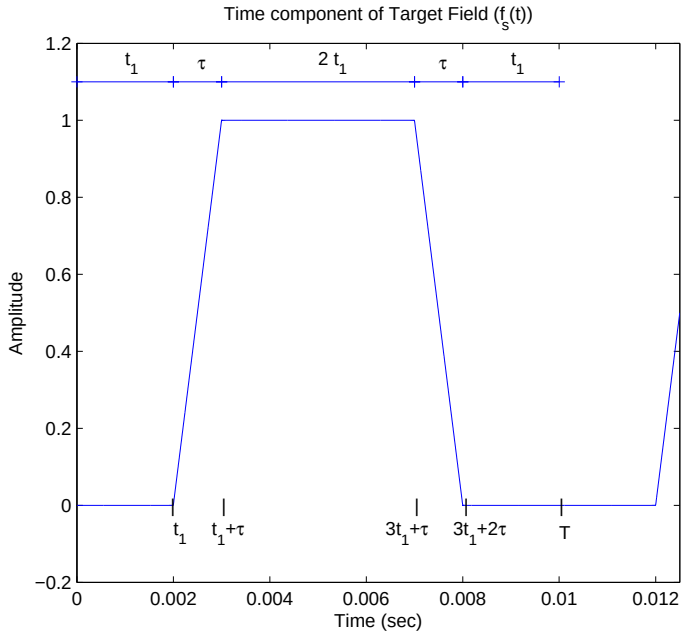

Figure 3.2: Switching Function for $\tau = 1$ ms ($\omega = 6.28$ kHz) and $T = 0.01$ s.

requirement that it can be represented by a Fourier series, such as

$$f_s(t) = W_0 + \sum_{k=1}^{K} W_k \cos\left(\frac{2\pi kt}{T}\right) + X_k \sin\left(\frac{2\pi kt}{T}\right), \tag{3.4}$$

where W_0, W_k and X_k are calculated from the Euler equations.

Following chapter 2 we have adopted a normalised, periodic, piecewise linear, ramp switching function. A complete cycle of the switching function has period T, with a rise time and fall time τ. Figure 3.2 shows the switching function graphically and equation (3.5) gives its algebraic description. The parameter t_1 denotes half the 'on' time, with the coil spending equal time in 'on' and 'off' states. The switching function is given by the expression

$$f_s(t) = \begin{cases} 0, & 0 < t \leq t_1 \\ \frac{1}{\tau}(t - t_1), & t_1 < t \leq t_1 + \tau \\ 1, & t_1 + \tau < t \leq 3t_1 + \tau \\ \frac{1}{\tau}(3t_1 - t) + 2, & 3t_1 + \tau < t \leq 3t_1 + 2\tau \\ 0, & 3t_1 + 2\tau < t \leq 4t_1 + 2\tau = T. \end{cases} \tag{3.5}$$

This is the same as the "ramp" function in equation (2.4) discussed in chapter 2. Following chapter 2 our assumed rise time of $\tau = 1\,\text{ms}$ ensures ω is small enough to discard phase retardation effects and make use of time independent forms of the continuity equation and Maxwell's equations.

3.5 Coil Deflection

The highly nonlinear system of Cauchy momentum equations provides the starting point for modelling the coil deflection. With Lorentz forces providing the only significant body force, Forbes *et al.* [30] simplified the system to the linearised vector form,

$$\rho_c \frac{\partial^2 \mathbf{u}}{\partial t^2} = \frac{1}{h}(\mathbf{j} \times \mathbf{B}) + (\Lambda + G)\nabla(\nabla \cdot \mathbf{u}) + G\nabla^2 \mathbf{u}. \tag{3.6}$$

Here, G and Λ are Lamé coefficients which are calculated from the Poisson's ratio and Young's modulus of the coil material which has density ρ_c. With the displacement vector given in cylindrical coordinates as $\mathbf{u} = u_r \hat{\mathbf{e}}_r + u_\theta \hat{\mathbf{e}}_\theta + u_z \hat{\mathbf{e}}_z$,

equation (3.6) expands in each orthogonal component to give

$$\rho_c \frac{\partial^2 u_r}{\partial t^2} = \frac{2}{h} B_{Z0} j_\theta + (\Lambda + G) \frac{\partial}{\partial r} (\nabla \cdot \mathbf{u}) + G \left(\nabla^2 u_r - \frac{u_r}{r^2} - \frac{2}{r^2} \frac{\partial u_\theta}{\partial \theta} \right) \quad (3.7a)$$

$$\rho_c \frac{\partial^2 u_\theta}{\partial t^2} = \frac{2}{h} B_r j_z + (\Lambda + G) \frac{1}{r} \frac{\partial}{\partial \theta} (\nabla \cdot \mathbf{u}) + G \left(\nabla^2 u_\theta - \frac{u_\theta}{r^2} + \frac{2}{r^2} \frac{\partial u_r}{\partial \theta} \right) \quad (3.7b)$$

$$\rho_c \frac{\partial^2 u_z}{\partial t^2} = -\frac{2}{h} B_r j_\theta + (\Lambda + G) \frac{\partial}{\partial z} (\nabla \cdot \mathbf{u}) + G \nabla^2 u_z .$$

Here, the cylindrical Laplacian is given by $\nabla^2 u_r = 1/r^2 \, \partial^2 u_r / \partial \theta^2 + \partial^2 u_r / \partial z^2$ and the divergence is $\nabla \cdot \mathbf{u} = u_r / r + 1/r \, \partial u_\theta / \partial \theta + \partial u_z / \partial z$. The radial derivatives have been dropped from the Laplacian and divergence by making use of a small displacement approximation. Notice that equations (3.7) generalise the simple one-dimensional model discussed in section 2.5.

In system (3.7), B_{Z0} denotes the z-directed field strength of the primary magnet and B_r is the radial component of the magnetic field produced by the gradient coil. The apparent absence of the gradient coil's B_θ and B_z components is due to cancellation of force components from either side of the current sheet.

The deflection uses the midpoint radius $r = r_M$ as the reference radius (see figure 3.1). Thus, we have modelled a thin walled vibrating cylinder as our MRI scanner.

This set of partial differential equations must be solved simultaneously, but the coupled nature of equations (3.7a) and (3.7b) makes this difficult for analytical methods. Introduction of the continuity equation in its quasi-static form, $\nabla \cdot \mathbf{u} = 0$, leads to $\frac{\partial u_\theta}{\partial \theta} = -u_r - r \frac{\partial u_z}{\partial z}$, and system (3.7) then decouples to

$$\rho_c \frac{\partial^2 u_z}{\partial t^2} - G \left(\frac{1}{r^2} \frac{\partial^2 u_z}{\partial \theta^2} + \frac{\partial^2 u_z}{\partial z^2} \right) = -\frac{2 B_r}{h} j_\theta , \quad (3.8a)$$

$$\rho_c \frac{\partial^2 u_r}{\partial t^2} - G \left(\frac{1}{r^2} \frac{\partial^2 u_r}{\partial \theta^2} + \frac{\partial^2 u_r}{\partial z^2} + \frac{1}{r} u_r \right) = \frac{2 B_{Z0}}{h} j_\theta + \frac{2G}{r} \frac{\partial u_z}{\partial z} , \quad (3.8b)$$

$$\frac{\partial u_\theta}{\partial \theta} = -u_r - r \frac{\partial u_z}{\partial z} , \quad (3.8c)$$

which can be solved in sequential order.

Here j_θ denotes the time varying current density contribution from each plate, i.e. $j_\theta = f_s(t)\left(j_\theta^P + j_\theta^S\right)$ where j_θ^P, j_θ^S and $f_s(t)$ are given in equations (3.3) and (3.5) respectively.

3.6 Pressure Wave and Sound Pressure Level

The deformation of the chamber wall creates a pressure wave in the air inside the chamber which can be heard as acoustic noise. To model the noise, the interaction between the air and inner wall must be determined. As in Forbes *et al.* [30], we apply a linearisation to the governing equations - conservation of mass, conservation of momentum and the isentropic gas relation (which relates the air pressure, p_A, to the density of the air, ρ_A) - and generate a wave equation for the pressure perturbation p_{A1},

$$\frac{\partial^2 p_{A1}}{\partial t^2} = c_{A0}^2 \nabla^2 p_{A1}, \tag{3.9}$$

where c_{A0} is the isentropic speed of sound, as in section 2.6.

3.6.1 Boundary Conditions

Our switching function, f_s, is assumed to repeat continuously and our measurements begin after enough time has passed to ensure all initial effects are negligible. An explicit requirement is that the air inside the chamber must move with the deflecting shell in the radial direction (derived from the conservation of momentum

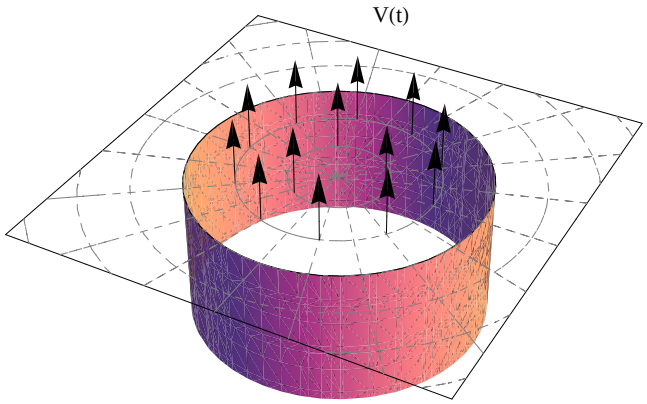

Figure 3.3: A geometric description of the air flow. We consider an infinite baffle at $z = 0$ and axial symmetry in the flow of air i.e. $V(t) = \int_0^{2\pi} \frac{\partial}{\partial t} u_z(\theta, 0, t)\, d\theta$.

equation), giving

$$\frac{\partial p_{A1}}{\partial r} = -\rho_{A0} \frac{\partial^2 u_r}{\partial t^2} \qquad \text{on} \quad r = a. \tag{3.10}$$

We impose a weaker 'semi-stick' condition between the air and the shell deflecting in the azimuthal and longitudinal directions. This assumption loses no generality because a shell deflecting azimuthally/longitudinally will not move the air and therefore not contribute to any pressure changes. Thus, equation (3.9) can be solved subject to condition (3.10) to give the air pressure perturbation inside an MRI chamber that is notionally of infinite length.

To adapt this model to a finite length coil, we treat each of the coil ends as a semi-infinite duct with an air baffle covering the end. Adopting a linear acoustic model and assuming axi-symmetric flow, $V(t)$, out of the chamber (figure 3.3) we can derive an appropriate boundary condition at the duct end. A detailed derivation of the end condition is given in Appendix A, with the final result repeated here

for reference:

$$p_{A1}(a,0,t) = \frac{1}{2}\rho_{A0}\, c_{A0}\, V(t) - \frac{\rho_{A0}\, c_{A0}^2}{\pi} \int_{t-\frac{2a}{c_{A0}}}^{t} V(\tau) \frac{1}{\sqrt{4a^2 - c_{A0}^2(t-\tau)^2}}\, d\tau, \quad \text{for large } t. \tag{3.11}$$

This term is then translated and applied to both ends of the chamber (at $z = \pm L$). We now solve the pressure wave problem (3.9) subject to conditions (3.10) and (3.11). Once the pressure perturbation, p_{A1}, has been found, the sound pressure level (SPL) within the chamber is calculated from

$$\text{SPL} = 20 \log_{10} \left(\frac{|p_{A1}|}{p_{ref}} \right). \tag{3.12}$$

The reference pressure, p_{ref}, is taken to be $2 \times 10^{-5}\,\text{Nm}^{-2}$, and the sound pressure level is measured in decibels (dB(A)).

3.7 Solution Process

The nonhomogeneous term in equation (3.8a) leads to nonlinearity in the Fourier coefficients. We can force linearity by setting $B_r \equiv 0$. Thus, the solution to the homogeneous form of (3.8a) is the complementary function,

$$u_z(z,t) = \sum_{k=1}^{K} \cos(k\omega t) \left(\Omega_{0k} \cos(\alpha_{0k} z) + \Theta_{0k} \sin(\alpha_{0k} z) \right), \tag{3.13}$$

where $\alpha_{0k} = \sqrt{\rho_c k^2 \omega^2 / G}$. The θ-dependence in u_z is ignored to match the axisymmetric flow out of the chamber.

Using (3.3) for j_θ^P and the equivalent form for j_θ^S, equations (3.8b) and (3.8c) can

now be solved for u_r and u_θ respectively. We assume $u_r(\theta, z, t)$ mimics the form of the time varying current density; i.e. $u_r(\theta, z, t) = f_u(t)(j_\theta^P + j_\theta^S)$, where $f_u(t)$ is a periodic temporal function given by

$$f_u(t) = \sum_{k=0}^{K} \xi_k \cos\left(\frac{2\pi k t}{T}\right).$$

This represents an even Fourier series, similar in form to the switching function $f_s(t)$ but with different coefficients. To solve equation (3.8c) we further assume $u_\theta(\theta, z, t)$ mimics the form of u_r. The expanded form for u_r and u_θ becomes

$$\begin{aligned} u_{(r,\theta)} &= \sum_{n=1}^{N} \Bigg[\sin\left(\frac{n\pi(z+L)}{2L}\right) \Bigg\{ {}_1H_{0n0}^{(r)} + \sum_{m=1}^{M} \left({}_2H_{mn0}^{(r,\theta)} \sin(m\theta) + {}_3H_{mn0}^{(r,\theta)} \cos(m\theta) \right) \\ &+ \sum_{k=1}^{K} \left({}_1H_{0nk}^{(r)} + \sum_{m=1}^{M} \left({}_2H_{mnk}^{(r,\theta)} \sin(m\theta) + {}_3H_{mnk}^{(r,\theta)} \cos(m\theta) \right) \right) \cos(k\omega t) \Bigg\} \\ &+ \cos\left(\frac{n\pi(z+L)}{2L}\right) \Bigg\{ {}_4H_{0n0}^{(r)} + \sum_{m=1}^{M} \left({}_5H_{mn0}^{(r,\theta)} \sin(m\theta) + {}_6H_{mn0}^{(r,\theta)} \cos(m\theta) \right) \\ &+ \sum_{k=1}^{K} \left({}_4H_{0nk}^{(r)} + \sum_{m=1}^{M} \left({}_5H_{mnk}^{(r,\theta)} \sin(m\theta) + {}_6H_{mnk}^{(r,\theta)} \cos(m\theta) \right) \right) \cos(k\omega t) \Bigg\} \Bigg], \end{aligned} \tag{3.14}$$

where u_r has coefficients ${}_jH_{mnk}^{r}$ and u_θ has coefficients ${}_jH_{mnk}^{\theta}$ $\forall\ m, n, k$ and $j = 1, 2, \ldots, 6$. Expressions for the coefficients are found by substituting the respective forms of (3.14) into equations (3.8b) and (3.8c) and equating linearly independent terms. These expressions can then be defined in terms of the Fourier coefficients of the switching function (equation (3.4)) and the Fourier coefficients of both the primary coil current density (equation (3.3)) and the equivalent shield coil current density. Implicit boundary conditions requiring 2π-periodicity in θ lead

to simplifications in some expressions, with a few of the coefficients shown below:

$$\left.\begin{aligned} {}_1H^z_{0nk} &= \frac{-2B_r W_k \left(P^P_{0n} + P^S_{0n}\right)}{h\left(Gn^2\pi^2/4L^2 - \rho_c k^2\omega^2\right)} \\ {}_1H^r_{0nk} &= \frac{2B_{Z0} W_k \left(P^P_{0n} + P^S_{0n}\right)}{h\left(Gn^2\pi^2/4L^2 - \rho_c k^2\omega^2 - G/{r_M}^2\right)} \\ {}_5H^\theta_{mnk} &= \frac{-\,{}_6H^r_{mnk}}{m} \\ {}_3H^\theta_{mnk} &= \frac{1}{m}\left({}_2H^r_{mnk} - {}_5H^z_{mnk}\frac{n\pi r_M}{2L}\right). \end{aligned}\right\} \tag{3.15}$$

3.7.1 The Residual System

With a desired magnetic field defined at the target radii, we apply the Biot-Savart law (equation (3.1)) to compute the current density distribution. Solving this for the current density is a highly ill-conditioned inverse problem requiring additional assumptions to increase the likelihood of obtaining a unique solution. These assumptions are introduced through penalty functions, and the combined system is then solved using Tikhonov regularisation (refer to Neittaanmaki *et al.* [89]).

Firstly, the Fourier series expressions for the current densities are substituted into equation (3.1) giving

$$\begin{aligned} B_z(r,\theta,z) &= -\mu_0 \sum_{n=1}^{N} \left(P^P_{0n} U_{0n}(r,z;a) + P^S_{0n} U_{0n}(r,z;b)\right) \\ &- \mu_0 \sum_{m=1}^{M}\sum_{n=1}^{N} \left[P^P_{mn}\cos(m\theta) + Q^P_{mn}\sin(m\theta)\right] U_{mn}(r,z;a) \\ &- \mu_0 \sum_{m=1}^{M}\sum_{n=1}^{N} \left[P^S_{mn}\cos(m\theta) + Q^S_{mn}\sin(m\theta)\right] U_{mn}(r,z;b)\,. \end{aligned} \tag{3.16}$$

The functions U_{0n} and U_{mn} $(m \geq 1)$ relate the source and field points and are

evaluated numerically using a 2D trapezoidal rule. They are defined as

$$\begin{aligned} U_{0n}(r,z;a) &= \frac{a}{\pi}\int_{-L}^{L}\int_{0}^{\pi}\frac{\left[r\cos\theta' - a\right]\sin\left(\frac{n\pi(z'+L)}{2L}\right)\,d\theta'\,dz'}{\left[a^2+r^2-2ar\cos\theta'+(z-z')^2\right]^{3/2}} \\ U_{mn}(r,z;a) &= \frac{a}{\pi}\int_{-L}^{L}\int_{0}^{\pi}\frac{\left[r\cos\theta' - a\right]\cos(m\theta')\cos\left(\frac{n\pi(z'+L)}{2L}\right)\,d\theta'\,dz'}{\left[a^2+r^2-2ar\cos\theta'+(z-z')^2\right]^{3/2}}\,. \end{aligned}$$

The principal goal in our design process is to match the magnetic field B_z to the target fields B_{TF} at inner radii c_1 and c_2, and outer radius c_3. The corresponding residual terms are

$$E_1 = \int_{pL}^{qL}\int_{-\pi}^{\pi}\left[B_{TF}(c_1,\theta,z) - B_z(c_1,\theta,z)\right]^2 c_1\,d\theta\,dz\,, \tag{3.17}$$

$$E_2 = \int_{pL}^{qL}\int_{-\pi}^{\pi}\left[B_{TF}(c_2,\theta,z) - B_z(c_2,\theta,z)\right]^2 c_2\,d\theta\,dz\,, \tag{3.18}$$

$$E_3 = \int_{-L}^{L}\int_{-\pi}^{\pi} B_z^2(c_3,\theta,z)\,c_3\,d\theta\,dz\,, \tag{3.19}$$

where $B_{TF}(c_3,\theta,z) = 0$. The shielding condition only considers the z-directed magnetic field as B_r and B_θ are orders of magnitude smaller than the combined z-directed magnetic field; see Forbes *et al.* [34]. In the three residual terms, B_z is calculated from equation (3.16).

By themselves, the three residual terms (3.17)–(3.19) do nothing to improve the conditioning of the system, so additional constraints must be considered. These represent secondary design concerns, of which we consider two for this model: smoothness of current winding patterns and acoustic noise. From a construction point of view, it is desirable to minimise the number of sharp turns in the winding patterns. Replicating Forbes *et al.* [34], penalty functionals related to the curvature of the respective streamfunctions (equation (3.2)) on the primary and shield

coils are constructed:

$$F_1 = \int_{-L}^{L}\int_{-\pi}^{\pi} \left|\nabla^2\Psi^P(\theta,z)\right|^2 \, a\, d\theta\, dz\,, \tag{3.20}$$

$$F_2 = \int_{-L}^{L}\int_{-\pi}^{\pi} \left|\nabla^2\Psi^S(\theta,z)\right|^2 \, b\, d\theta\, dz\,. \tag{3.21}$$

In considering the acoustic effect, equations (3.10) and (3.12) tell us that a reduction in the deflection of the coil will lead to a reduction in the noise level inside the chamber. This naturally leads to the additional penalty term

$$F_3 = \int_0^T\int_{-L}^{L}\int_{-\pi}^{\pi} \|\underset{\sim}{\boldsymbol{u}}\|^2 \, r_M\, d\theta\, dz\, dt = \int_0^T\int_{-L}^{L}\int_{-\pi}^{\pi} \left[u_r^2+u_\theta^2+u_z^2\right] \, r_M\, d\theta\, dz\, dt. \tag{3.22}$$

Combining the functionals (3.17) - (3.22) we construct the total residual functional

$$R = E_1 + E_2 + E_3 + \lambda_P F_1 + \lambda_S F_2 + \lambda_U F_3, \tag{3.23}$$

and minimise it with respect to the primary coil Fourier coefficients P_{0n}^P, P_{mn}^P, Q_{mn}^P, and the equivalent shield coefficients P_{0n}^S, P_{mn}^S, Q_{mn}^S. The nonnegative regularisation parameters λ_P, λ_S and λ_U are dimensionless weights whose values are determined by numerical experimentation; the parameters play a similar role to Lagrange multipliers in an optimisation process. The relative contribution of each residual term can be manipulated by changing the value of its associated regularisation parameter. Empirically determined optimum values represent a trade off between improving the conditioning of the system, noise reduction, winding smoothness, and target field matching.

Regularizing for a y-gradient, for example, leads to the $2N$ simultaneous equations

$$\frac{\partial R}{\partial Q_{1n}^{P}} = 0, \qquad \frac{\partial R}{\partial Q_{1n}^{S}} = 0, \qquad \forall\ n. \tag{3.24}$$

Following Forbes *et al.* [30, 32] this can be written as a linear tridiagonal block matrix system, similar to (2.21) in chapter 2.

$$\begin{bmatrix} \Sigma_{1y}^{aa} & \Sigma_{1y}^{ab} \\ \Sigma_{1y}^{ba} & \Sigma_{1y}^{bb} \end{bmatrix} \begin{bmatrix} Q_{1n}^{P} \\ Q_{1n}^{S} \end{bmatrix} = \begin{bmatrix} \Pi_{1y}^{a} \\ \Pi_{1y}^{b} \end{bmatrix}, \tag{3.25}$$

or succinctly as $\Sigma\, Q = \Pi$. Then, $Q = \Sigma^{-1}\, \Pi$ and the Fourier coefficients Q_{1n}^{P} and Q_{1n}^{S} are immediately obtained. Obviously, the invertibility of Σ (measured by its condition number) will be controlled by the parameter values λ_P, λ_S, and λ_U.

A point to note is that this problem can be generalised further by considering a λ_{Shield} regularisation parameter to accompany the shield term (E_3) in the residual system (3.23). This would allow the effects of the shielding to be weighted more strongly in favour of producing a null field if λ_{Shield} was given a large positive weighting. The unit weighting the shielding term is currently receiving suggests that in this design the shielding is considered to be just as important as replicating the target field in the DSV. This is only a minor loss of generailty, however, an extra degree of freedom is missed by requiring the shielding term to have a unit weighting. Slightly larger noise reductions may be obtained if the manufacturer is prepared to allow stray fields to extend beyond the outer target radius (c_3).

3.7.2 Solving for the Pressure Wave

Once determined, the Fourier coefficients are inserted into the coil deflection coefficients (examples of which are given in equations (3.15)). To find the sound pressure level inside the coil the pressure perturbation, p_{A1}, must be determined by solving equation (3.9) subject to the boundary conditions (3.10) and (3.11). This system can be solved by seeking a representation of the form

$$p_{A1} = \psi_1(r,\theta,z,t) + \psi_2(r,z,t),$$

as it yields the following decoupled systems for ψ_1 and ψ_2:

$$\left.\begin{aligned} \frac{\partial^2\psi_1}{\partial t^2} &= c_{A0}^2\left(\frac{\partial^2\psi_1}{\partial r^2}+\frac{1}{r}\frac{\partial\psi_1}{\partial r}+\frac{1}{r^2}\frac{\partial^2\psi_1}{\partial\theta^2}+\frac{\partial^2\psi_1}{\partial z^2}\right) \\ \frac{\partial\psi_1}{\partial r} &= -\rho_{A0}\,\frac{\partial^2 u_r}{\partial t^2} \quad \text{on} \quad r=a \\ \psi_1 &= 0 \quad \text{on } r=a,\ z=\pm L, \end{aligned}\right\} \tag{3.26}$$

$$\left.\begin{aligned} \frac{\partial^2\psi_2}{\partial t^2} &= c_{A0}^2\left(\frac{\partial^2\psi_2}{\partial r^2}+\frac{1}{r}\frac{\partial\psi_2}{\partial r}+\frac{\partial^2\psi_2}{\partial z^2}\right) \\ \frac{\partial\psi_2}{\partial r} &= 0 \quad \text{on} \quad r=a \\ \psi_2 &= \Gamma_{\pm}(t) \quad \text{on } r=a,\ z=\pm L, \end{aligned}\right\} \tag{3.27}$$

where boundary condition (3.11) is written $p_{A1}(a,\pm L,t)\equiv\Gamma_{\pm}(t)$ for convenience. Boundary value problem (3.26) was considered in chapter 2 with solution

$$\begin{aligned} \psi_1(r,\theta,z,t) &= \sum_{n=1}^{N}\sum_{k=1}^{K}\frac{\rho_{A0}\ k^2\ \omega^2}{T_{nk}\ I_1'(aT_{nk})}\ {}_5H_{1nk}^r \\ &\quad \times I_1(rT_{nk})\ \cos(k\omega t)\ \sin(\theta)\ \sin\left(\frac{n\pi(z+L)}{2L}\right). \end{aligned} \tag{3.28}$$

Here $I_m(x)$ denotes the modified Bessel function of the first kind of order m, as defined by Abramowitz and Stegun [1], and

$$T_{nk} = \sqrt{\frac{n^2\pi^2}{4L^2} - \frac{k^2\omega^2}{c_{A0}^2}} \qquad \text{and} \qquad I_m^{'}(aT_{nk}) = \frac{\partial}{\partial\nu} I_m(\nu)\bigg|_{\nu=aT_{nk}},$$

as in equation (2.26) for the simplified model of the previous chapter. In solving boundary value problem (3.27), the time dependent boundary condition requires that $V(t)$ (the flow out of the tube) be determined first. For simplicity we define

$$V_{\pm}(t) = \sum_{k=1}^{K} \delta_{k_{\pm}} \sin(k\omega t), \tag{3.29}$$

where the coefficients δ_k are determined from the conservation of mass relation over the closed surface of the chamber, $\oiint \nabla \cdot \mathbf{v}\, dS = 0$. We now define $\Gamma(t)$ as a Fourier series,

$$\Gamma_{\pm}(t) = \sum_{k=1}^{K} \dot{A}_{k_{\pm}} \cos(k\omega t) + \dot{B}_{k_{\pm}} \sin(k\omega t),$$

with the Fourier coefficients $\dot{A}_{k_{\pm}}$ based on $\delta_{k_{\pm}}$ and Weber functions, and $\dot{B}_{k_{\pm}}$ based on $\delta_{k_{\pm}}$ and Bessel functions; see Zhang and Jin [119].

The derivative boundary condition in (3.27) can be satisfied by forcing $\psi_2 \sim J_0(r\beta_{1,k}/a)$ where $\beta_{1,k}$ denotes the k^{th} zero of the Bessel function $J_1(x)$. We also require the temporal variation to match that of the switching function, such that the solution becomes

$$\begin{aligned}\psi_2(r,z,t) \;=\; & \sum_{k=1}^{K} J_0\left(\frac{j_{1,k}}{a} r\right) \left(\left(\Upsilon_{1k}\cos(\lambda_k z) + \Upsilon_{2k}\sin(\lambda_k z)\right)\cos(k\omega t) \right. \\ & \left. + \; \left(\Upsilon_{3k}\cos(\lambda_k z) + \Upsilon_{4k}\sin(\lambda_k z)\right)\sin(k\omega t) \right), \end{aligned} \tag{3.30}$$

where

$$\Upsilon_{1k} = \frac{\dot{A}_{k_+} + \dot{A}_{k_-}}{2\cos(\lambda_k L)\, J_0(j_{1,k})} \quad \text{and} \quad \Upsilon_{2k} = \frac{\dot{A}_{k_+} - \dot{A}_{k_-}}{2\sin(\lambda_k L)\, J_0(j_{1,k})}\,,$$

and Υ_{3k} and Υ_{4k} have analogous forms using $\dot{B}_{k_+}$ and $\dot{B}_{k_-}$ respectively. Also, for convenience we have defined $\lambda_k = \sqrt{k^2\omega^2/c_{A0}^2 - j_{1,k}^2/a^2}$.

Equations (3.28) and (3.30) now sum to give the pressure perturbation p_{A1} in the chamber, and equation (3.12) is used to compute the noise associated with the distortion of the gradient coil.

3.8 Results

For the results presented in this chapter, the following settings have been used to model those of a notional MRI $y-$gradient coil. The primary radius was set at $a = 0.3\,\mathrm{m}$ with shield radius $b = 0.4\,\mathrm{m}$, thereby giving a structure of thickness $h = 0.1\,\mathrm{m}$; its length was $L = 1\,\mathrm{m}$. Being modelled as a copper tube, the density is $\rho_c = 8.99\times10^3\,\mathrm{kgm}^{-3}$, Young's modulus $E = 1.3\times10^{10}\,\mathrm{Nm}^{-2}$, and Poisson's ratio $\nu = 0.2$. From the latter two properties all other relevant elasticity parameters can readily be determined.

The radius of each target cylinder (defined in figure 3.1) has been arbitrarily set to $\{c_1, c_2, c_3\} = \{0.2, 0.1, 0.6\}\,\mathrm{m}$. The two internal target cylinders are located asymmetrically over the interval $pL \le z \le qL$ with $p = -0.7$ and $q = 0.1$.

The coil is immersed in an axially directed background magnetic field of strength $B_{Z0} = 2\,\mathrm{T}$. The gradient field produces a linear variation in B_z of $100\,\mathrm{mT/m}$ with switching frequency $\omega = 23\,\mathrm{kHz}$.

3.8.1 Coil Design: y-gradient

The primary design requirements for a shielded gradient coil are to produce a highly linear magnetic field within the DSV and minimal field external to the structure. Haacke *et al.* [45] cites 95% as the lower limit for DSV gradient homogeneity for imaging purposes.

Ideally, to design a quiet coil we desire the coil deflection regularisation parameter, λ_U, to be as large as possible. Similarly, smoother windings on the primary and shield coils will result from larger values of λ_P and λ_S. Through the regularisation process, however, any improvement in secondary effects comes at the cost of gradient homogeneity. As such, we seek parameter values that provide a balance of secondary improvements whilst maintaining a suitable level of field homogeneity and adequate sheilding.

Figure 3.4 demonstrates the agreement between the simulated axial magnetic field, B_z, and the desired target field, B_{TF}, for two values of λ_U. Here, λ_P and λ_S have been empirically found and fixed at 10^{-7}. The profiles are given for $x = 0$, $z = (p + q)L/2$. With $\lambda_U = 1$, figure 3.4(a) depicts the resultant field when a minimal attempt has been made to reduce the simulated acoustic noise level. Conversely, figure 3.4(b) displays the field produced when $\lambda_U = 10^{19}$, the largest value λ_U can take and still produce sufficient gradient homogeneity. Differences in shielding effectiveness are negligible at $r = c_3$.

Despite the significant difference in the two parameter values, the optimised system only produced a 0.5 dB improvement in noise level. Higher noise reductions were observed but had to be discarded due to inadequate gradient homogeneity; e.g. a 10 dB reduction was obtained with $\lambda_U = 10^{21}$ but gradient homogeneity was at 81%.

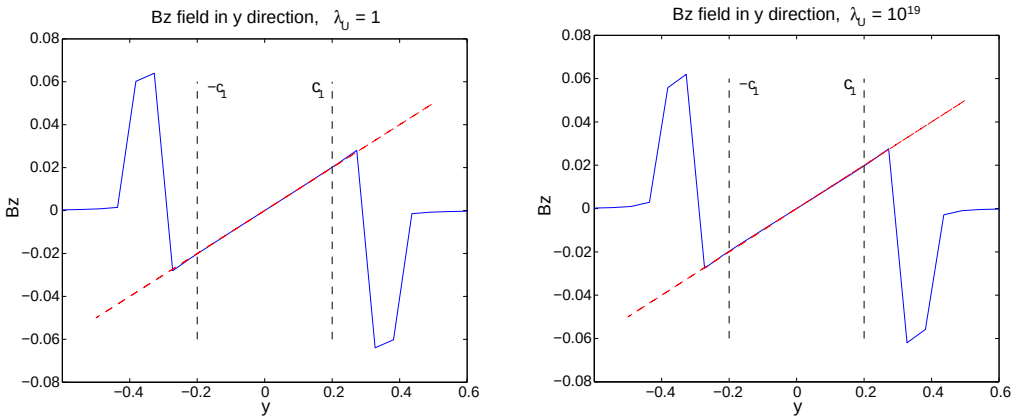

(a) The target field match for $\lambda_U = 10^0$ (b) The target field match for $\lambda_U = 10^{19}$

Figure 3.4: Red line: the target field. Blue line: the actual field. Figure shows the trade off of the matching of the target field over the target region $-c_1$ to c_1 for two different λ_U values.

3.8.2 1D and 3D Coil Deflection model comparison

Results that solely consider the u_r component (a 1D model) of the chamber's deflection can be found in chapter 2 and will be hereafter referred to as the 1D model. The model for the coil in this chapter mirrors that for the 1D model but is extended to allow for 3D coil deflections. In general, the 3D model leads to greater coil displacement which in turn leads to louder simulated acoustic noise. However, when the added constraint of a high level of gradient field homogeneity is required, noise reductions are comparable to those for the 1D model.

The boundary value problem (3.26) represents the governing equations for the infinite length pressure wave perturbation, ψ_1, and boundary value problem (3.27) represents the governing equations for the pressure perturbation, ψ_2, from a ring source - here, modelling each end of the finite length coil. The infinite pressure wave has no u_θ or u_z dependence, indicating that in order to minimise the simulated acoustic noise arising from the homogeneous solution for the pressure perturbation (ψ_1), it is necessary to minimise *only* the coil deflection in the radial

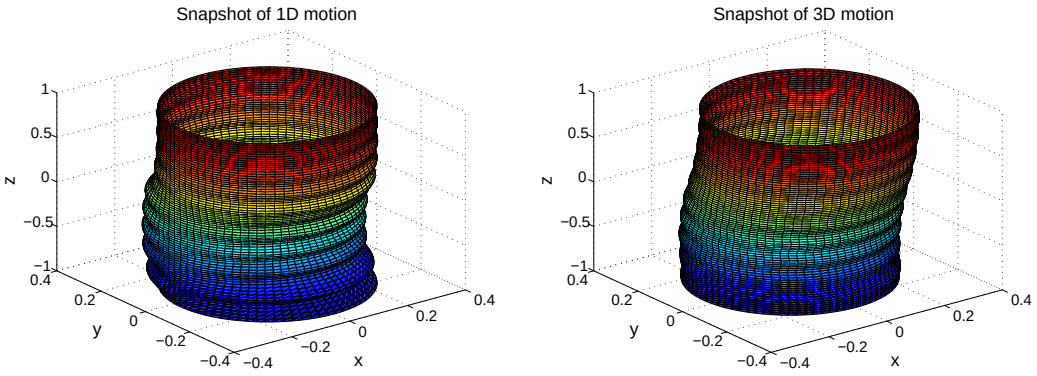

(a) Coil Deflection for 1D model (b) Coil Deflection for 3D model

Figure 3.5: A depiction of the coil deflection using (a) the 1D deflection model (scaled by 10^4) and (b) the 3D deflection model (scaled by $10^{3.2}$).

direction.

Inspection of equation (3.28) shows that ψ_1 has resonances when the Fourier coefficients ${}_5H^r_{1nk} \to \infty$. This also corresponds to a resonance in the radial deflection component and thus by Mechefske *et al.* [87] and chapter 2 a large noise amplitude will be heard. The θ-component of the coil deflection will similarly have resonances when ${}_jH^\theta_{1nk} \to \infty$, however, these do not correspond to a resonance in the pressure wave and will not affect the noise level output.

The difference in coil deflections predicted with the two models can be seen in figure 3.5; to aid visualisation, the coil deflections (in the $\hat{\boldsymbol{r}}$, $\hat{\boldsymbol{\theta}}$ and $\hat{\boldsymbol{z}}$ directions) are amplified. In this case the 1D deflections are magnified by 10^4 whereas the 3D deflections are magnified by $10^{3.2}$. Component-wise for the 3D model, $\|u_z\| \approx 0$, while $\|u_r\| = 0.0012 = \|u_\theta\| \neq 0$. In contrast, for the 1D model $\|u_r\| = 0.00014$. The deflection in the 3D case is clearly greater, hence, the magnitude of the noise predicted by the 3D model is significantly louder, as confirmed.

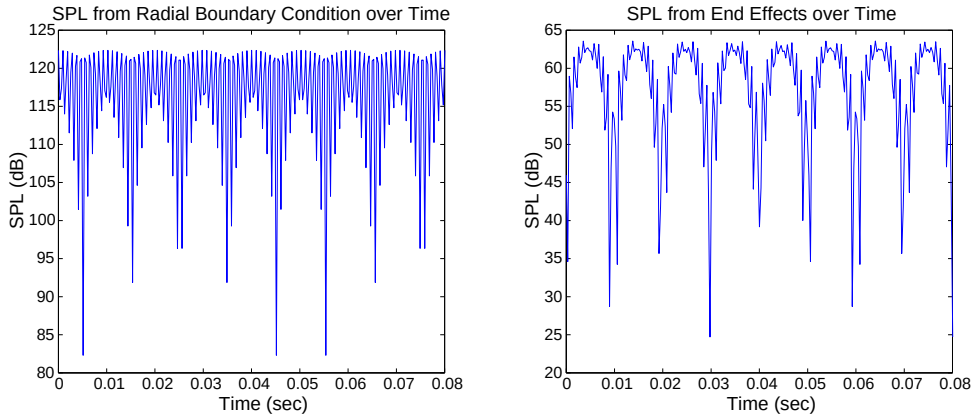

(a) ψ_1 over time

(b) ψ_2 over time

Figure 3.6: This figure graphs (a) the noise associated with the chamber deflecting in the radial direction (ψ_1) and (b) the noise associated with the end effect conditions (ψ_2).

3.8.3 End Effects

The end effects have been modelled by assuming an axisymmetric, time dependent flow rate out of the chamber. Initially it was thought an axisymmetric flow would be appropriate as a general case, however, the cyclic θ-dependence associated with higher order azimuthal gradient fields negates any net axisymmetric flow out of the chamber in our model, giving $V(t) \equiv 0$ and therefore $\psi_2 \equiv 0$. As a consequence, this end effects model is only applicable for z-gradient coils.

Figure 3.6(a) gives the noise output associated with the infinite pressure wave (ψ_1) and figure 3.6(b) gives the noise output associated with the end effects only (ψ_2). The maximum SPL of ψ_1 is $\approx 122.4\,\text{dB}$, whereas the maximum SPL of ψ_2 is $63.6\,\text{dB}$. Thus, not surprisingly, the noise from the radial deformation of the chamber dominates the noise effects resulting from the pressure wave reflecting at the open boundaries. Adding the two components together produces a noise level $0.03\,\text{dB}$ (on average) higher than ψ_1 on its own.

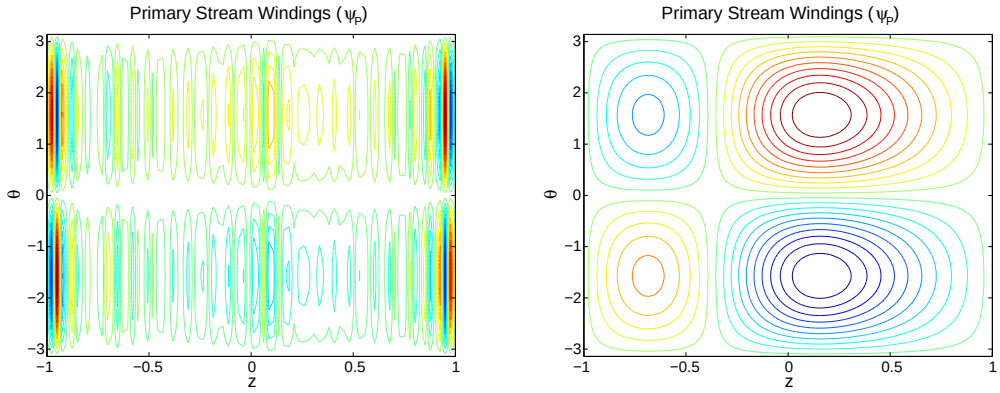

(a) $\lambda_U = \lambda_P = \lambda_S = 0$ (b) $\lambda_U = 0$ and $\lambda_P = \lambda_S$ are large

Figure 3.7: (a) shows coil distribution pattern when all regularisation parameters (λ's) are zero. (b) shifts the emphasis to smooth current distribution patterns.

3.8.4 The Matrix Σ and its Affects on Results

The condition of matrix Σ is largely determined by the paramter values λ_P, λ_S, and λ_U. As mentioned previously the Tikhonov regularisation approach we have adopted involves a trial and error process in search of an optimum set of lambda values. A poor choice of λ values can result in an unfeasible solution, in this case an unbuildable coil.

Figure 3.7 shows the resulting coil winding patterns for 'extreme' λ choices. In the case where no attempt to regularise the system (3.25) has been taken, we set all λ's to be 0 (see figure 3.7(a)). We note the current winding pattern produced by inverting matrix Σ, solving for each Fourier coefficeint (e.g. Q_{1n}^P) and substituting into the expression for the stream function (3.2) is unsuitable for MRI use. The windings specified are extremely dense and large opposing currents exist on the extremeties of the coil. Although this is a mathematical solution to system (3.25) it does not constitute a solution that can be engineered. Choosing another 'extreme' set of regularisation parameters where the smoothness of the winding patterns have been given utmost importance does, on this occasion, yeild a build-

able coil from an engineering point of view (see figure 3.7(b)). This confirms the choice of λ's having a two fold effect: one, simply to allow an accurate solution of system (3.25) and two, adding weight to the regularisation term associated with the regularisation parameter. The windings associated with figure 3.7(b) do not, however, produce reductions in acoustic noise, and our problem thus requires further searching for an appropriate regularisation parameter set.

3.9 Discussion and Conclusion

This chapter describes one process of designing a gradient coil to reduce simulated acoustic noise output generated by the Lorentz forces. A Tikhonov regularisation method has been used to overcome the ill-conditioned nature of the inverse problem successfully. The major design requirements of producing a linear field in the DSV and small external magnetic fields to the coil have been met. Reducing the deflection of the coil and hence the simulated acoustic noise has been achieved as a secondary design issue to a small extent. A relatively small drop of 0.5 dB was the optimum achievement (from a base of 134.7 dB) while still satisfying the primary design issues.

A linearised coil deflection system for each orthogonal deflection component (3.6) was solved in its most general form. The nature of system (3.6) suggested numerical solutions would be required but an application of the Continuity equation avoided this problem. Closed form solutions were obtained for each coil deflection component and the pressure perturbation. The model presented in this chapter gives a complete discription of the cylindrical deflection components and acoustic effects of a typical gradient coil. A corollary of the results is that large amplitude acoustic noise appears to be a negative but necessary result of a gradient coil that

produces a linear field.

The 'thin-walled' nature of our gradient coil model is a first step approximation to a genuine gradient coil which typically falls into the 'thick-walled' class, see Mechefske and Wang [85]. For our 'thin-walled' model shear deformation effects are obviously ignored, however, this should not be the case in general. Mechefske and Wang [85] have demonstrated that at least for low switching frequencies shear deformations can be ignored under a 'thick-walled' model.

The validity of the assumptions for the coil deflection model found in chapter 2 are confirmed by the results presented here. The form of the infinite pressure wave is identical to the 1D deflection model pressure wave seen in chapter 2. Similar sound pressure level results were produced in the 3D case. This predicts that a necessary requirement for minimising the simulated acoustic noise output generated by the Lorentz forces is minimising the radial coil deflection component.

Also demonstrated was the insignificant effects of applying open boundary conditions on the pressure wave. Quantitatively, the finite length pressure wave produced essentially the same simulated noise amplitude as the infinite pressure wave case. The extra mathematical and computational effort required to correct the infinite pressure wave by less than 1% is in this authors opinion not worth while. However, this work may be useful to other researchers employing numerical methods, who may be able to incorporate the open boundary effects more simply into their code.

Limitations to the acoustic noise model presented in chapters 2 and 3 are its ability to be generalised to multiple coil vibration combinations. It is believed that combined vibration effects from multiple coils (e.g. x and y gradients together or gradient and RF coils) complicate the vibrational and acoustic fields significantly.

In addition to a more complex acoustic field pattern the coupled vibrations may negatively affect the image acquisition stage as well.

Future work will consider a braced gradient coil following Lin [72] but is not in the scope of this thesis. This paper confirms the braces will only need to be 'ring' clamps that force nodes in the radial deformation component to reduce the noise. A model for the coil deflection with forced nodes to model braced positions potentially involves a more complex partial differential equation system which may not allow analytical solutions however.

Chapter 4

Achieving Quiet Coils through Image Processing

4.1 Introduction

So far, our attempts to reduce the acoustically significant noise have been relatively unsuccessful. Only small reductions in noise have been gained while forcing the gradient coil to produce an adequately homogeneous linear field. In this chapter we abandon the restriction that the gradient coil need produce a linear field. As long as the field produced by the gradient coil provides unambiguous spatial information about the imaging region (i.e. is 1 : 1 over the imaging region), then its role is not defeated. Haacke *et al.* [45] suggested that useful images ought to be obtainable with coils that generate non-linear fields, and various techniques for doing so are presented by Janke *et al.* [59], Langlois *et al.* [66] and Bernstein *et al.* [4] for example. Wang *et al.* [110] and Gunter *et al.* [44] made use of a phantom image to calibrate the non-linear distortions of the field, using complex three-dimensional structures from which they could calculate the true location of

a point within the reconstructed image. Other researches such as Hennig *et al.* [49] have developed a theoretical method to encode using non-cartesian directed gradients. Their paper suggests it is possible to select circular slices whithin the DSV by applying a radially directed gradient field in combination with regular cartesian gradients. Further research into using non-linear gradients has resulted in advanced techniques designed to produce accelerated scanning times. The article by Stockmann *et al.* [100] details a method called 'O-space imaging' whereby they assert that a radially directed gradient is more efficient in terms of providing more encoding in the angular direction than in the radial direction and is suitable for the natural cylindrical nature of a typical MRI scanner. The radially directed gradient is used in combination with a standard linear gradient to shift the encoding area off centre to gain resolution over regions where the Z2 gradient would be 0 (i.e. the centre of the DSV). One advantage discussed in the paper is that increasing the ring density (number of Z2 slices) leads to significant improvements in resolution, in contrast to cartesian acquisitions. More recently, Forbes, Brideson and While [31] devised a simple correction technique, also based on the use of a phantom, in which the distortion effects due to field non-linearity can in principle be cancelled away exactly, and this technique appears to show promise in recovering good quality images even in the presence of reasonably strong non-linearity.

In this chapter, a method is presented for designing quiet self-shielded gradient coils. Our model follows that of chapter 2 which has been confirmed as acceptable based on the results of chapter 3. However, in this chapter, the noise reduction becomes the primary goal, with the requirement that the gradient coil produce a linear field being only a secondary concern. The algorithm of Forbes, Brideson and While [31] (referred to hereafter as the FBW algorithm) is then used to ex-

tract high quality images from these quiet coils, and is based on the use of a phantom. The term 'quality' must be clarified, 'quality' has a specific meaning in image reconstruction relating to the propogation of noise throughout the formation process. Our model has not considered the effects of noise due to non-linear field effects. We do, however, use the word 'quality' to denote a subjective measure of whether an image is recognisable or not and under this context we have already used the term 'quality' in the abstract and introductory sections. This technique corrects, in principle, purely for the distortion due to non-linear field effects. However, it cannot account for noise in the original signal due to other causes. Some sample images are shown to illustrate the robustness of this design.

The material for this chapter has been published as the article [58]: J. Jackson, L. Forbes, P. While, and M. Brideson. Could Image Processing Enable Reduced simulated acoustic noise during MRI Scans? *Concepts Magn Reson B Magn Reson Eng*, 39(B):191-205, 2011.

4.2 Mathematical Formulation

The approach for designing the gradient coil is essentially that of chapter 2 and again a brief summary is given for completeness.

4.2.1 The Geometry

We model our gradient coil system as a set of six coils, comprising three primary coils all located at radius $r = a$, and 3 shield coils all lying at radius $r = b > a$. Each coil is modelled as a cylindrically shaped copper sheet with current flowing on both sides. One gradient coil pair is considered to be a primary coil and shield

coil in combination. A depiction of our model for one gradient coil pair is given in figure 2.1 (or 3.1). The chamber has length $2L$, inner (primary) radius a and outer (shield) radius b. Hence, the coil has thickness $h = b - a$ and a midpoint radius of $r_M = a + h/2$. We also assume the coil material has an associated Young's Modulus E and Poisson's ratio ν.

We have adopted the standard cartesian coordinate system, with the origin located at the centre of the chamber and the z-axis aligned with the axis of symmetry. Naturally, the shape of the coil lends itself to the standard cylindrical coordinate system, as in chapters 2 and 3.

The two internal target cylinders (located at radii c_1 and c_2) aid in giving the magnetic field in the DSV its appropriate gradient form, while the external target cylinder (located at $r = c_3$) enforces the shielding constraint. To enable imaging of a region not centrally located within the chamber, the two internal target cylinders are specified over an asymmetric interval $pL \leq z \leq qL$. Here, p and q are dimensionless constants where $-1 < p < q < 1$ (with the symmetric case occurring when $p = -q$). Results are presented in this chapter for both symmetric and asymmetric designs.

4.2.2 Magnetic Field and Current Distribution

The magnetic field is calculated from the Biot - Savart law once the current distribution is known. We are interested solely in the z-directed component, B_z, of the magnetic induction field, $\mathbf{B}$, which is related to the magnetic field strength, $\mathbf{H}$, simply by $\mathbf{B} = \mu_0\mathbf{H}$. Assuming our current distribution has the form $\mathbf{j} = j_\theta(\theta', z')\hat{\boldsymbol{e}}_\theta + j_z(\theta', z')\hat{\mathbf{e}}_z$, and using the fact that equal current is contained between contours of the stream function (see Brideson *et al.* [11]), Forbes *et al.*

[30] argued that the primary coil stream function takes the form

$$\begin{aligned}\Psi^P(\theta,z) &= -\sum_{n=1}^{N}\frac{2L}{n\pi}P_{0n}^P\cos\left(\frac{n\pi(z+L)}{2L}\right)\\ &+ \sum_{m=1}^{M}\sum_{n=1}^{N}\frac{2L}{n\pi}\left[P_{mn}^P\cos(m\theta)+Q_{mn}^P\sin(m\theta)\right]\sin\left(\frac{n\pi(z+L)}{2L}\right)\end{aligned} \quad (4.1)$$

The shield stream function takes the form of equation (4.1) but with all P superscripts replaced with S superscripts. Use of the continuity equation $\nabla\cdot\mathbf{j}=0$ then allows computation of j_θ, j_z, and hence B_z. The Fourier coefficients are as yet unknown and we use a regularisation approach to determine them, which will be described shortly.

4.2.3 Coil Deflection and Noise

Yao *et al.* [117] demonstrated that to reduce noise output from a gradient coil one must reduce the coil distortion in the radial direction. We have adopted this idea, and take from Jackson *et al.* [57], following Boresi and Chong [9] p262, our deformation model to be

$$\rho_c\frac{\partial^2 u_r}{\partial t^2}+\frac{1}{r_M^2}(\Lambda+2G)u_r-G\nabla^2 u_r=\frac{2B_{Z0}}{h}(j_\theta^P+j_\theta^S), \quad (4.2)$$

where u_r is the coil displacement in the radial direction, ρ_c is the density of the scanner medium (copper), and Λ and G are Lamé coefficients found from the Young's modulus and Poisson's ratio of the coil. Notice that a small displacement approximation has been made, in which all radial derivatives are ignored. Thus, ∇^2 has its typical cylindrical form without the radial derivative components i.e. $\nabla^2 u_r = 1/r^2\partial^2 u_r/\partial\theta^2+\partial^2 u_r/\partial z^2$. The reference radius for our deflection analysis is taken to be $r=r_M$ and our coil is moddeled as a 'thin walled' vibrating cylinder

of radius r_M.

Calculating the resulting pressure wave from the coil deflection effects is a difficult problem and we adopt a linearisation approach in order to solve for the pressure perturbation analytically. The linearised pressure perturbation, p_{A1}, satisfies the wave equation, (2.8), and is subject to the boundary condition (2.9) of the coil. For simplicity, we assume an infinite-domain pressure wave model and can therefore ignore the effects of the open boundaries at $z = \pm L$. The only imposed boundary condition is that the air inside the chamber have the same radial speed as the inner wall of the gradient coil. Hence, our pressure perturbation problem again becomes

$$\frac{\partial^2 p_{A1}}{\partial t^2} = c_{A0}^2 \nabla^2 p_{A1} \tag{4.3}$$

$$\frac{\partial p_{A1}}{\partial r} = -\rho_{A0} \frac{\partial^2 u_r}{\partial t^2} \quad \text{on} \quad r = a, \tag{4.4}$$

as in the previous chapters. Here c_{A0} is the speed of sound and ρ_{A0} is the density of air inside the chamber, as in chapters 2 and 3. The noise level inside the chamber can now be found using

$$\text{SPL} = 20 \log_{10} \left(\frac{|p_{A1}|}{p_{ref}} \right), \tag{4.5}$$

where the noise level is measured in decibels (dB(A)) and p_{ref} is taken to be 2×10^{-5} Nm^{-2}, as previously.

4.2.4 Method of Solution

Solving for the coil deflection and pressure wave follows directly from chapter 2. The coil deflection is assumed to have a similar Fourier series representation to the

azimuthal current density. The coefficients of the coil deflection are then found in terms of the current density Fourier coefficients (still unknown) by equating linearly independent terms. Solving the pressure perturbation system (equations (4.3) and (4.4)) is also based on Fourier series representations.

The regularisation process is similar to equation (2.19); however, in this chapter we are primarily interested in minimizing the simulated acoustic noise. We therefore create a residual system where the residual term involves minimizing the coil deflection (4.7), and the regularisation terms are related to: field matching (4.8), shielding (4.9), winding pattern smoothing (4.10) and (4.11), and power maximisation (4.12). The residual system thus takes the form

$$R = E_1 + \lambda_1 F_1 + \lambda_2 F_2 + \lambda_3 F_3 + \lambda_P F_4 + \lambda_S F_5 - \lambda_{Power} F_6, \tag{4.6}$$

where each term is given below and terms $E_1 - F_5$ are discussed in chapter 2, and take the forms

$$\begin{aligned}
E_1 &= \int_0^T \int_{-L}^{L} \int_{-\pi}^{\pi} u_r^2(\theta, z, t)\, r_M d\theta\, dz\, dt, && (4.7)\\
F_j &= \int_{pL}^{qL} \int_{-\pi}^{\pi} \left(H_{TF}(c_j, \theta, z) - H_z(c_j, \theta, z)\right)^2 c_j\, d\theta\, dz, \quad \text{for } j = 1, 2 && (4.8)\\
F_3 &= \int_{-L}^{L} \int_{-\pi}^{\pi} H_z^2(c_3, \theta, z)\, c_3\, d\theta\, dz\,, && (4.9)\\
F_4 &= \int_{-L}^{L} \int_{-\pi}^{\pi} |\nabla^2 \Psi^P(\theta, z)|^2\, a\, d\theta\, dz, && (4.10)\\
F_5 &= \int_{-L}^{L} \int_{-\pi}^{\pi} |\nabla^2 \Psi^S(\theta, z)|^2\, b\, d\theta\, dz, && (4.11)\\
F_6 &= \frac{\rho_r}{h} \left(\int_{-L}^{L} \int_{-\pi}^{\pi} \|\mathbf{j}^P\|^2 a d\theta dz + \int_{-L}^{L} \int_{-\pi}^{\pi} \|\mathbf{j}^S\|^2 b d\theta dz \right). && (4.12)
\end{aligned}$$

The regularisation term F_6 in (4.12) is an expression of the coils' power usage, found in Jin [60], p117. The regularisation parameters (the λ values) must be

determined through experimentation to achieve an optimum. Each term has a quadratic dependence on the Fourier coefficients and this process is known as Tikhonov regularisation [105]. As each λ is increased it adds more weight to its corresponding regularisation term. We seek a current distribution that will: minimise the simulated acoustic noise, match the target field, produce smooth winding patterns, and use a moderate amount of power by minimizing the residual system with respect to the unknown Fourier coefficients P_{0n}^{P} etc. Notice that the sign in front of λ_{Power} is negative in (4.6), and this indicates that when λ_{Power} is increased, the coil solution will require increased power. Typically a gradient coil is desired to use a minimum amount of power; however, we found that minimizing both noise and power results in a gradient coil of insufficient field strength, thus negating the purpose of the gradient coil, which is to spatially encode nuclei in the target region. We compensate for this by requiring that the gradient coil uses a moderate amount of power. Optimisation of the residual system (4.6) with respect to the Fourier coefficients yields a tri-diagonal block matrix equation similar to equations (2.21) and (3.25). An accurate solution of the Fourier coefficients (from the block matrix equation) will result if the λ terms have been chosen large enough to condition the system adequately.

4.3 Results

Here we limit our analysis to a y-gradient design by noting the x-gradient analysis is analogous. The problem presented can actually be simplified to analyse a z-gradient coil, but this is not discussed further here. The dimensions of our illustrative y-gradient coil mimic those capable of full human body scans. The primary and shield coils have a half length of $L = 1\,\mathrm{m}$ and radius $a = 0.3\,\mathrm{m}$ and

$b = \frac{4}{3}a = 0.4\,\mathrm{m}$ respectively. The two inner target fields are set at radii $c_1 = 0.2\,\mathrm{m}$ and $c_2 = 0.1\,\mathrm{m}$, and are longitudinally symmetric with $p = -q = -0.3$ where $z \in [pL, qL]$. The third target field is located at $c_3 = \frac{3}{2}b = 0.6$ m and extends the full length of the coil. The coil is immersed in a background magnetic field of strength $B_{Z0} = 2\,\mathrm{T}$ and the small variations caused by the gradient fields have a gradient strength of $B_{grad} = 100\,\mathrm{mT/m}$. We have modelled the switching of the gradient coils as a repeating piecewise (trapezoidal) linear 'ramp' wave discussed in detail in section 3.4.

4.3.1 A Minimum Power Coil compared to a Minimum Noise Coil

A minimum power coil is presented as a reference coil due to its commonality in MRI (see Turner [108]). To produce a minimum power coil we simply ignore the residual term E_1 and set $\lambda_1 = \lambda_2 = \lambda_3 = 1$, $\lambda_P = \lambda_S = 0$, and $-\lambda_{Power}$ as large as possible while ensuring the induced field remains within a 5% deviation from the target field. In our case we take $\lambda_{Power} = -10^3$. The requirements for a minimum noise coil are more difficult to specify. The regularisation process becomes an intricate balancing act between λ values to achieve an optimum solution. Typically, it is a requirement that an induced gradient field be within a 5% maximum deviation from the target field. We relax this condition considerably and later describe how to recreate a usable image given the non-linear field produced. The shielding and smoothness of the winding patterns, however, are still important and must be weighted accordingly. We also increase the power used by the minimum noise coil to ensure the field produced by the minimum noise coil has adequate strength. Our minimum noise coil has the following regularisation parameter configuration:

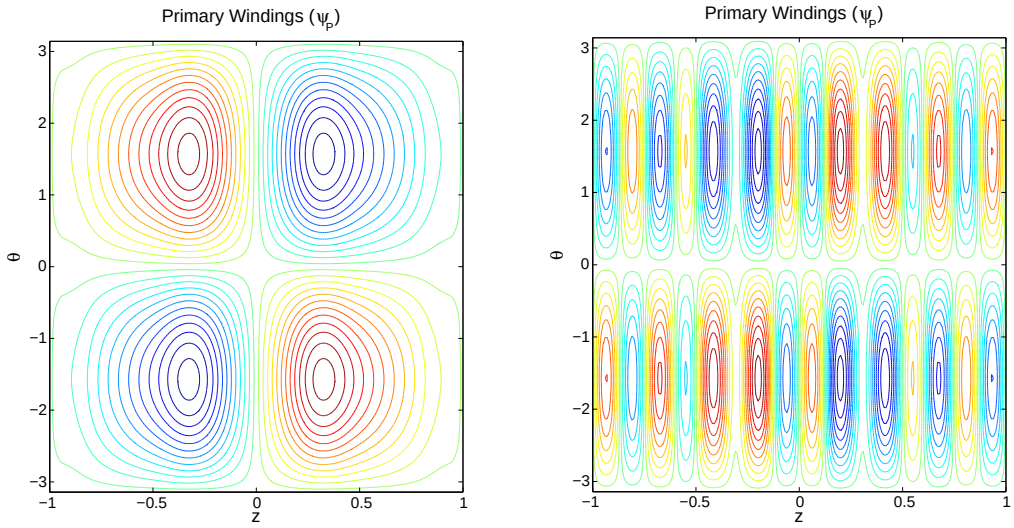

(a) Minimum Power Coil (b) Minimum Noise Coil

Figure 4.1: Comparison of the primary windings between a) the well known minimum power coil configuration and b) the minimum noise coil.

$\lambda_1 = \lambda_2 = 10^{-25.2}$, $\lambda_3 = 10^{-24.9}$, $\lambda_P = \lambda_S = 10^{-32}$, and $\lambda_{Power} = 10^{-22.2}$. These values were chosen by experiment to reduce the simulated acoustic noise. The winding patterns on the primary coil for the minimum power coil and minimum noise coil are presented in figure 4.1.

The windings for the minimum power coil are undoubtedly smoother and easier to build; however, the simulated acoustic noise output between the two coils is of most significance here. Figure 4.2 shows the simulated acoustic noise produced from the minimum power and minimum noise coils. The minimum noise coil produces 49 dB less peak noise than the minimum power coil. A reduction of 49 dB in noise is unparalleled in MRI literature. Mansfield *et al.* [77] employed a force balancing approach to reduce noise actively, gaining reductions up to 30 dB. The passive technique of Edelstein *et al.* [23] used a copper sheet to shield a gradient coil acoustically, and this achieved maximum reductions of 25 dB.

Our premise is that we are reducing the deflection of the coil in the radial di-

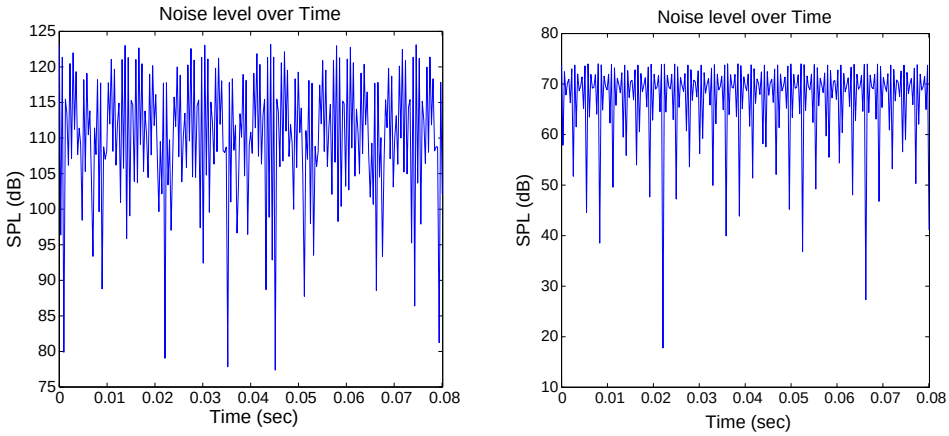

(a) Minimum Power Coil (b) Minimum Noise Coil

Figure 4.2: Comparison of the simulated acoustic noise output between a) the minimum power coil and b) the minimum noise coil. As seen, the reduction in maximum noise is a large 49 dB for the minimum noise coil.

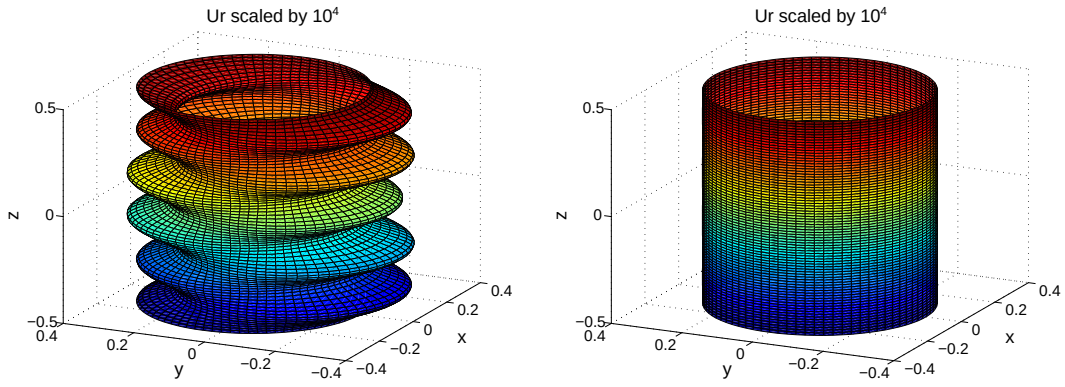

(a) Minimum Power Coil (b) Minimum Noise Coil

Figure 4.3: Comparison of the radial coil deflection of the chamber for a) the minimum power coil and b) the minimum noise coil. As seen, the radial deformation is significantly reduced in the minimum noise coil. The small displacements have been magnified by 10^4 for ease of visualisation.

rection in order to reduce the simulated acoustic noise output. In figure 4.3 we can see a disparity between the distortion of the minimum power coil and the minimum noise coil. This is reflected in figure 4.2, where the noise level output is significantly lessened for the minimum noise coil. Quantitatively the 2-norm of the radial coil displacement is 2.54×10^{-4} and 1.15×10^{-6} for the minimum power and minimum noise coils respectively, which supports further the claim of reduced noise output.

The fields along the y-axis produced by the minimum power coil and minimum noise coil are seen in figure 4.4. The minimum power coil has less than 5% inhomogeneity from the target field. On the other hand, the minimum noise coil produces a very non-linear field. Using present day technology and practices the field seen in figure 4.4(b) would be deemed unusable for image construction purposes. However, the recent FBW algorithm [31] offers the possibility that even the very non-linear field of figure 4.4(b) may be capable of yielding images of acceptable image quality and acquired with greatly reduced noise levels. This is now investigated in detail for the minimum noise coil.

The magnetic field generated by the y-gradient minimum-noise coil was calculated on the $x-y$ plane, orthogonal to the direction of the main magnetic field (oriented along the z-axis). As discussed above, the x-gradient situation is a congruent problem simply involving a 90° rotation in the $x-y$ plane. In order to make the field spatially encoding, an average was taken of the x and y-gradient fields to produce an overall field B_z.

The linear part of this non-linear gradient field is first estimated by least-squares fitting, over a square in the $x-y$ plane inscribed within the outer target cylinder of radius c_1 depicted in figure 2.1. This square is thus located within the region

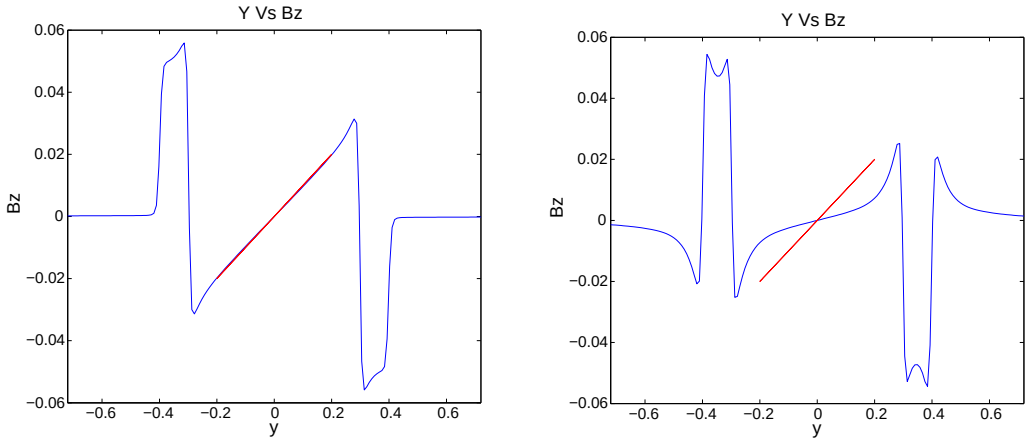

(a) Minimum Power Coil (b) Minimum Noise Coil

Figure 4.4: Comparison of the B_z fields produced between a) the minimum power coil and b) the minimum noise coil. The red line indicates the target field. The minimum power coil has a maximum deviation of less than 5%. In contrast, the minimum noise coil has a maximum deviation of over 55%.

$|x| < c_1/\sqrt{2}$, $|y| < c_1/\sqrt{2}$. This linear component of the field has the form

$$B_{Z\text{ linear}} = xG_X + yG_Y, \tag{4.13}$$

where the x and y-gradient strengths are estimated from the non-linear field B_z using the least-squares formulae

$$\begin{aligned} G_X &= \frac{3}{c_1^4}\int_{-c_1/\sqrt{2}}^{c_1/\sqrt{2}}\int_{-c_1/\sqrt{2}}^{c_1/\sqrt{2}} xB_z(x,y)\,dx\,dy \\ G_Y &= \frac{3}{c_1^4}\int_{-c_1/\sqrt{2}}^{c_1/\sqrt{2}}\int_{-c_1/\sqrt{2}}^{c_1/\sqrt{2}} yB_z(x,y)\,dx\,dy. \end{aligned} \tag{4.14}$$

These fields over the inscribed square within the target zone on the $x-y$ plane are illustrated in figure 4.5. The gradients were calculated to be $G_X = 0.0245$ and $G_Y = 0.0240\,\mathrm{T/m}$ respectively, using (4.14). The curvature in the non-linear field is evident in the diagram, particularly in the corners of the inscribed square, and the field lies above or below the plane over different portions of the central

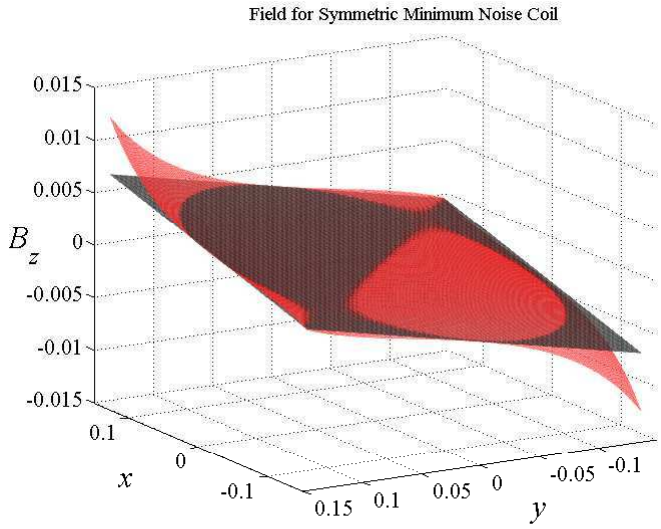

Figure 4.5: Magnetic Field within the inscribed square in the outer target cylinder, on the $x - y$ plane. The non-linear field B_z is shown in red, and its linearised component $B_{z\ \mathrm{linear}}$ obtained by least-squares fitting is the plane shown in black.

section of the square.

As a means of testing how well the non-linear field in figure 4.5 is capable of generating a faithful replication of an image, we have imposed an optical photograph over the inscribed square $|x| < c_1/\sqrt{2}$, $|y| < c_1/\sqrt{2}$, and used the density of the optical image as a proxy for the magnetic spin density $m(x, y)$ in an actual MRI scan. In the usual spin-echo process of magnetic resonance imaging, the measured signal M_T obtained from illuminating the sample with an RF signal at frequency ω is found from the Bloch equation in the form

$$M_T = \iint m(x, y) \exp\left(-i \int \omega \, dt\right) dx \, dy \tag{4.15}$$

and further details are available in the texts by Vlaadingerbroeck and den Boer [109] and Haacke *et al.* [45]. The gradient field is spatially encoded according to

the Larmor relation $\omega = \gamma B_z$ in which the field B_z can be represented in the form

$$B_z = xG_X + yG_Y + \mathcal{N}(x, y). \tag{4.16}$$

This generalises the linear approximation in (4.13), since the function $\mathcal{N}(x, y)$ represents all the non-linear components of the field. When equation (4.16) is substituted into (4.15), and sampling at each frequency is assumed to occur over the time interval Δt, it follows that what is obtained from the imaging process is the *distorted* signal

$$M_T^d\left(k_x, k_y\right) = \iint m(x, y)C(x, y)\exp\left(-i[xk_x + yk_y]\right)\, dx\, dy, \tag{4.17}$$

where the distortion function due to non-linearity is represented by the term

$$C(x, y) = \exp\left(-i\gamma\mathcal{N}(x, y)\Delta t\right) \tag{4.18}$$

and the two wavenumbers are

$$k_x = \gamma G_X \Delta t \quad \text{and} \quad k_y = \gamma G_Y \Delta t. \tag{4.19}$$

When the inverse Fourier Transform of the signal (4.17) is taken, the original image is not recovered, but instead, the *distorted* image

$$m^d(x, y) = \frac{1}{(2\pi)^2}\iint M_T^d\left(k_x, k_y\right)\exp\left(i[xk_x + yk_y]\right)\, dk_x\, dk_y \tag{4.20}$$

is obtained, due to the effects of field non-linearity. Now suppose that a phantom sample with *known* spin density $p(x, y)$ is imaged in the same non-linear field. It will give a distorted signal analogous to that in (4.17), and the Inverse Fourier

Transform similar to (4.20) will then produce a distorted image $p^d(x, y)$ instead of the original. According to the FBW algorithm [31], an undistorted image of the original spin density function $m(x, y)$ can then be obtained from the formula

$$m(x, y) = p(x, y)\frac{m^d(x, y)}{p^d(x, y)}. \tag{4.21}$$

This procedure is now investigated using an optical image and for the minimum-noise coil. A photographic image has been chosen to represent the spin density function $m(x, y)$, in part because the authors do not have access to an MRI whole-body imaging system, and also because the photo serves as a severe test of the capacity of this new quiet coil to generate useful images from its non-linear magnetic field. Previous work by Tieng *et al.* [103] and Eggers *et al.* [24] has provided simulated validation of image processing techniques that restore clarity to an image without the use of a phantom. The work by Tieng *et al.* [103], however, does require that the non-linearity of the field be measurable. Eggers *et al.* [24] on the other hand, discretise the imaging region and develop several computational methods (of varying efficiency) for overcoming the ill-conditioned non-linear field imaging problem.

The original optical image is shown in figure 4.6. It was taken from a photograph sampled at every fifth point in both the x and y-coordinates to produce a density map over a 320×240 matrix, and then imposed over the coordinate grid $-c_1/\sqrt{2} < x < c_1/\sqrt{2}$, $-c_1/\sqrt{2} < y < c_1/\sqrt{2}$. Care must be taken in choosing the window in the Fourier Transform space $\left(k_x, k_y\right)$ over which the frequencies are to be sampled; this is equivalent to choosing the time interval Δt over which each frequency is acquired, and in the present chapter, we have therefore chosen to sample over the frequency domain $-\gamma\Delta t G_X < k_x < \gamma\Delta t G_X$, $-\gamma\Delta t G_Y < k_y < \gamma\Delta t G_Y$, in which γ is the nuclear gyromagnetic ratio as before, with value taken from

Figure 4.6: The photographic image of Ellie The Cat imposed over the square region inscribed within the outer target region. This is an effective 0.0768 Megapixel image, and will serve as a proxy for the magnetic spin density function $m(x, y)$.

$\gamma/2\pi = 42.6 \times 10^6$ Hz/Tesla. It is necessary to experiment somewhat with the time interval Δt in order to obtain sufficient resolution in the re-constructed image, while at the same time avoiding numerical errors in the evaluation of the integrals in equations (4.17) and (4.20). This has some parallels with some of the techniques for k-space sampling discussed by Blaimer *et al.* [7].

The signal $M_T^d\big(k_x, k_y\big)$ obtained from the image in figure 4.6 using the non-linear field in figure 4.5 has been computed from equation (4.17). Good resolution has been obtained with the choice $\Delta t = 2.5/2\pi$ milliseconds, which defines the window in k-space as described above. The real part of this transform is presented in figure 4.7. The Fourier Transform of a purely linear field would normally appear as a narrow peak in the centre of the region, but the strong influence of field non-linearity here is responsible for the diffused signal evident particularly in the foreground of this picture. The non-linear distortion function in equation (4.17)

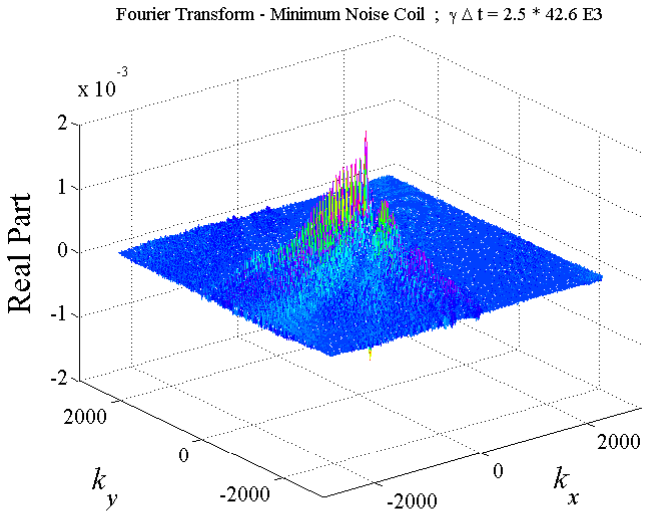

Figure 4.7: The Fourier Transform of Ellie The Cat obtained from the non-linear field produced by the minimum noise coil.

was calculated from equation (4.18)

$$C(x,y) = \exp\left[-i\gamma\Delta t\big(B_z - B_{z\,\mathrm{linear}}\big)\right],$$

using the linear component of the magnetic field calculated in equation (4.13) by least-squares fitting.

Figure 4.8(a) shows the distorted image $m^d(x,y)$ in equation (4.20) calculated for this case. It bears little resemblance to the original image in figure 4.6, and would not be useful for any purpose at all. This is entirely to be expected, and of course is the reason that such care is normally taken to ensure that the background magnetic field is linear to a high degree of homogeneity. Indeed, the patterns of interference lines in figure 4.8(a) coincide precisely with the maxima and minima in the field B_z produced by this coil, so that it is evident that the entire image is dominated by non-linear field effects.

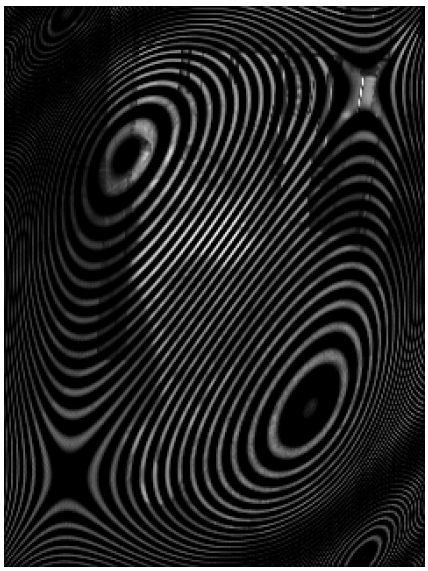

(a) Minimum Noise Uncorrected

(b) Minimum Noise Clean Image

Figure 4.8: Comparison of the re-constructed images of Ellie The Cat using a) The uncorrected Inverse Fourier Transform and b) the FBW algorithm. A simple Gaussian phantom was used for the corrected image in b).

The image in figure 4.8(b), on the other hand, recovers a great deal of the detail present in the original picture in figure 4.6, down to very small length scales. It was obtained using the FBW algorithm [31] given in equation (4.21), making use of the simple Gaussian phantom function

$$p(x, y) = \exp\Big[-\left(x^2 + y^2\right)/a^2\Big], \tag{4.22}$$

in which the width parameter a was chosen to be $a = c_1/2$. We experimented with this choice (4.22) to a limited extent, but no discernible effect was seen in the image in figure 4.8(b), and indeed Forbes *et al.* [31] argue that the FBW technique (4.21) is insensitive to the choice of phantom provided that $p(x, y) > 0$, at least in principle. There is still appreciable ghosting and distortion at the top left and bottom right corners of this image, and this is clearly associated with the highly curved portions of the non-linear magnetic field at those corners, visible in figure 4.5. It may be possible to reduce these effects further by the choice of

a different phantom to that in equation (4.22), but this has not been pursued here; nevertheless, within the inner target zone (a circle of radius $c_2 = 0.1\,\mathrm{m}$ in figure 4.8(b)) the recovered image bears an obvious resemblance to the original. A difference map between the original and re-constructed image shows that for this field, the pointwise difference is less than 0.1% over the inner target zone of radius c_2.

4.3.2 Asymmetric Minimum Noise Coil

A generalisation of the symmetric target field case has been considered. Results are presented for a minimum noise coil with the interior target fields being located in the z-direction over the interval $[pL,qL]$ where $p = -0.7$ and $q = 0.1$. As an illustration of the robustness of this method of design, results are presented that give smoother winding patterns (compared to the symmetric case, see figure 4.1(b)) for a smaller reduction in noise for the asymmetric gradient coil described. Two designs are shown that sacrifice the matching of the target field (similarly to that shown in 4.4(b)) for different levels of winding smoothness and noise reduction. The noise level generated by such an asymmetric coil that has no coil deflection minimisation is simulated to be 130 dB, which we take as our peak reference noise level. In comparison the noise produced from the coil depicted in figure 4.9(a) is 87 dB, a reduction of 43 dB. The windings in figure 4.9(b) appear smoother than that of 4.9(a) and as such a smaller reduction in noise is obtained. For Design 2, the noise output was calculated to be 100 dB, a reduction of 30 dB, which is still significant.

Figure 4.10 shows the Design 1 distorted image $m^d(x, y)$ from equation (4.20), and the corrected image obtained by the FBW algorithm and Gaussian phantom

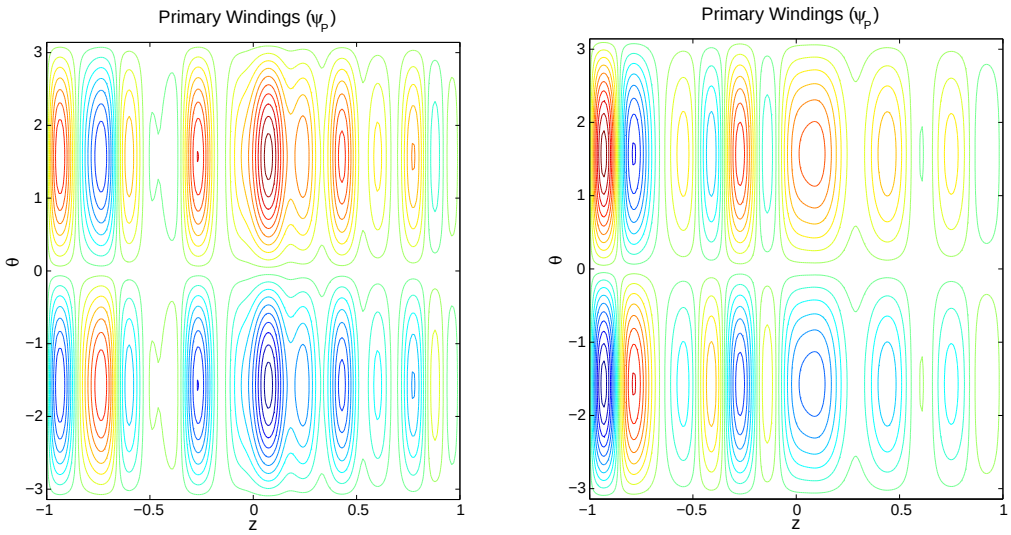

(a) Asymmetric Noise Reduction: Design 1 (b) Asymmetric Noise Reduction: Design 2

Figure 4.9: Two different sets of λ values that produce different winding patterns (and noise levels) for an asymmetric gradient design.

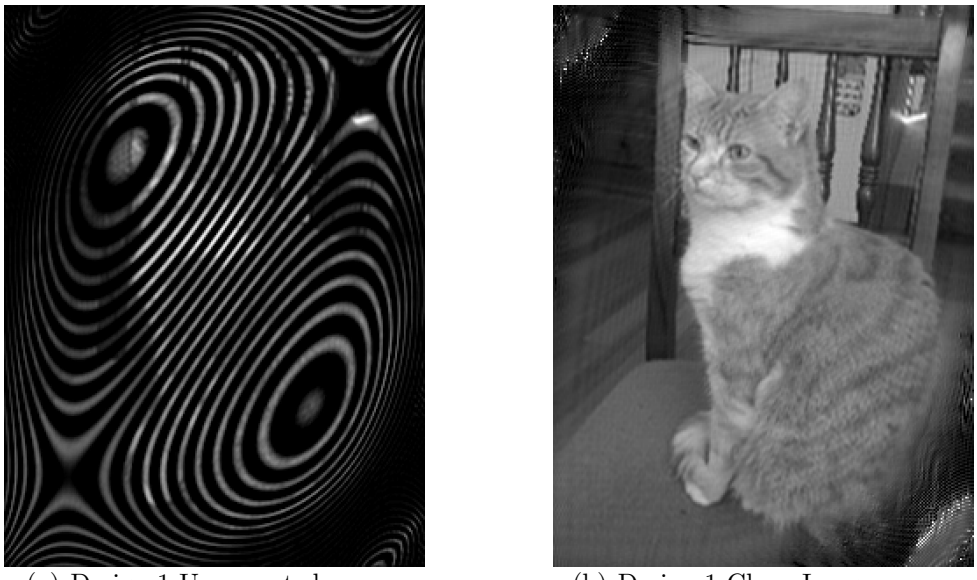

(a) Design 1 Uncorrected (b) Design 1 Clean Image

Figure 4.10: Comparison of the re-constructed images of Ellie The Cat for the field produced by the coil windings in Design 1, using a) The uncorrected Inverse Fourier Transform and b) the FBW algorithm. A simple Gaussian phantom was used for the corrected image in b).

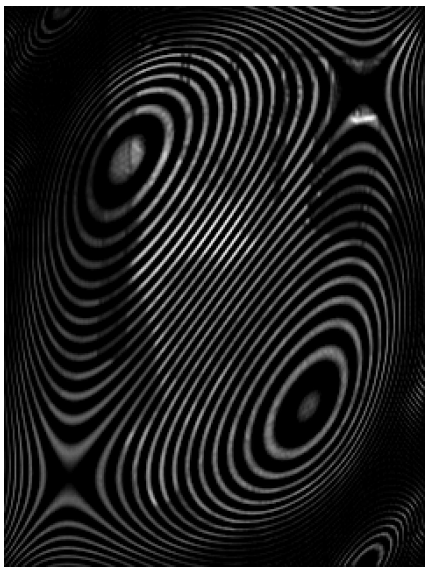

(a) Design 2 Uncorrected

(b) Design 2 Clean Image

Figure 4.11: Comparison of the re-constructed images of Ellie The Cat for the field produced by the coil windings in Design 2, using a) The uncorrected Inverse Fourier Transform and b) the FBW algorithm. A simple Gaussian phantom was used for the corrected image in b).

function (4.22). In this case, the sampling time interval was increased slightly to $\Delta t = 3/2\pi$ milliseconds, in order to improve resolution for this very asymmetric field by expanding the sampling domain in the Fourier k-space. Again, the uncorrected image in figure 4.10(a) is dominated by the non-linear features of the gradient field, and would not be useful for almost any practical purpose. By contrast, the corrected image in 4.10(b) recovers a reasonably high level of accurate detail, at least within the inner target zone (picturing a circle of radius $c_2 = 0.1\,\mathrm{m}$ on this diagram). It is evident, however, that the image in figure 4.10(b) is of a slightly inferior quality to that for the symmetric minimum noise coil in figure 4.8(b). This is perhaps to be expected, due to the very asymmetric location of the target zones in Design 1.

The corresponding comparison between the uncorrected and corrected images for the field produced by Design 2 is given in figure 4.11. For this design, the domain in the Fourier k-space was increased slightly wider, by changing the sampling time

interval to $\Delta t = 4/2\pi$ milliseconds in order to retain resolution of the detail in the re-constructed image in figure 4.11(b). Again, the uncorrected image in figure 4.11(a) is highly affected by the non-linearity of the magnetic field generated by the gradient coils, and is of little value, but the cleaned image obtained with the FBW algorithm in figure 4.11(b) is able to recover detail to a high degree of accuracy at least within the inner target zone. There is significant distortion about the top left and bottom right corners of the diagram, however, and this was not able to be removed. The corrected images for both Design 1 and Design 2 in figures 4.10(b) and 4.11(b) were both obtained with the simple phantom in equation (4.22), and it is not known if an alternative phantom might improve these re-constructed images.

4.3.3 Length Considerations

Results are now presented for a symmetric coil of half length, $L = 0.5\,\mathrm{m}$. Shown in figure 4.12 is the primary winding pattern (4.12(a)) and noise output (4.12(b)) for a half length minimum noise coil. The shorter length minimum noise coil has a similar winding pattern to that of the full length symmetric coil (refer to figure 4.1(b)); however, the current required for the half length coil is considerably higher, as shown in table 4.1. When setting comparable λ values, the reductions in noise for the half length coil (compared with the half length minimum power coil which produced 124 dB) are 13 dB less than that of the full length minimum noise coil.

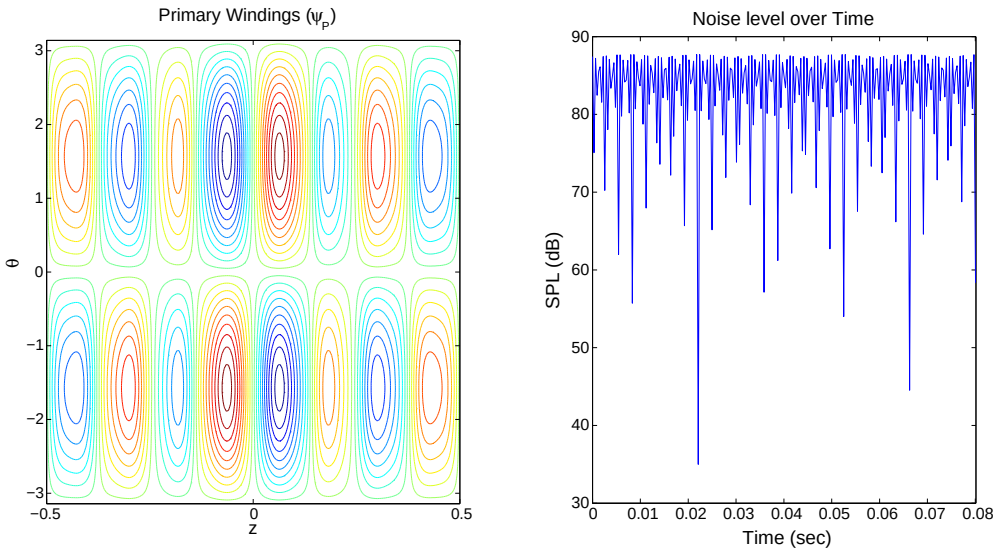

(a) Primary Winding Pattern

(b) SPL

Figure 4.12: A minimum noise design for a symmetric half length ($L = 0.5\,\mathrm{m}$) gradient coil. The primary winding pattern is shown in (a), and the corresponding noise level is given in (b).

4.3.4 Performance

The current (A) that each design uses is presented in table 4.1 and is inversely proportional to the coil's efficiency, η. Table 4.1 also presents a measure of each coil's performance defined by Chronik and Rutt [19] (the η^2/L factor). Note that

Designs	Current (A)	Performance (η^2/L)	Noise (dB)
Min Power (Sym)	2770	0.758×10^{-5}	123
Min Noise (Sym)	1640	0.778×10^{-5}	74
Design 1 (Asym)	1920	1.36×10^{-5}	87
Design 2 (Asym)	1520	2.15×10^{-5}	100
Half Length (Sym)	3110	0.328×10^{-5}	88

Table 4.1: This table summarises the current used and coil performance for each coil design presented. All values are given in standard units.

for the minimum power and minimum noise symmetric coils this parameter is comparable and as such this demonstrates that noise reduction is being traded

for field homogeneity and not coil performance.

4.4 Discussion

For the minimum noise coil an extreme example is presented to illustrate the versatility of this technique. As noise is measured on a log scale (see Bies and Hansen [6]) a reduction of approximately 50 dB in sound pressure level corresponds to a reduction in pressure perturbation of 2.5 orders of magnitude. The extreme minimum noise case does, however, force the gradient coil to be manufactured with dense localised windings and strong opposing current nearby. From an engineering perspective such a coil is difficult to manufacture. Referring to table 4.1, it is important to note that the performance of both coils is similar and meet acceptable modern design standards; see Zhang *et al.* [118]. The values calculated are less than half an order of magnitude from the optimised power coils presented by Zhang *et al.* Thus, our coil exchanges field linearity for noise reduction without compromising performance. Field linearity has been regarded as an essential requirement in the design of a gradient coil, and the uncorrected images shown in figures 4.8(a), 4.10(a) and 4.11(a) demonstrate how an image is rendered completely useless by magnetic field inhomogeneity. However, the use of a phantom in the FBW algorithm of Forbes *et al.* [31] enables good quality images to be recovered in spite of field non-linearity. This suggests that coils could now be designed that deliver large reductions in acoustic noise, but still permit images of practical use in medical diagnosis from their non-linear fields. Whether this optimistic outlook carries over from the simulation to real-world remains to be tested.

The determination of the magnetic fields produced in this chapter differs from

chapters 2 and 3. In chapters 2 and 3 the magnetic fields were calculated simply by applying the continuous current distributions to the Biot-Savart Law through the Fourier coefficients. In the previous chapters this was acceptable as the winding patterns generated did not produce the same degree of oscillations and thus the integral in the Biot-Savart Law was well behaved and a discretised coil approach would closely resemble the continuous winding patterns. In this chapter, however, a discrete approach has been taken. Each winding pattern has been contoured and discretised into small arcs of current. The magnetic field emanating from each arc has then been calculated and the resulting field is the sum of fields produced from each arc. This approach takes an extra step towards modelling a realistic coil made of grooves etched into a copper sheet from a continuous current distribution. The placement of each discrete wire becomes critical to ensure each oscillation in the continuous current distribution is captured and a realistic representation of the continuous winding patterns designed are obtained from the discretisation process.

As stated in the introduction of this chapter the term 'image quality' has been used throughout this chapter as a subjective measure of a usable image for clinical purposes. This differs from its technical definition relating to noise in an image as a result of the imaging process. Here, no quantitative measure has been given to the 'quality' of images recovered using the FBW algorithm. A quantitative measure for the image quality was considered but no algorithm or parameter was deemed appropriate for this assesment. Future work will involve adding simulated noise into the original image (in this case figure 4.6) and then carefully analysing how the noise propogates throughout the FBW reconstruction algorithm. This will allow calculation of a meaningful quantitative value for image quality.

Localised dense opposing windings appear to be an unavoidable result of noise

reduction in gradient coil design. Noise reduction is predicated on reducing the Lorentz forces that cause the chamber to deform. Conceptually, dense opposing windings will produce localised Lorentz forces that will cancel each other locally, thus leading to a smaller net force on the chamber, less deflection, and less noise.

All designs presented have been calculated using 30 modes ($N = 30$) of the harmonic series found in equation (4.1). All winding patterns had suitably converged with this number of terms. In addition the grid size and spacing of each design was also considered and stable solutions were retained. This suggests our model is producing genuine non-trivial stable winding patterns that are at least theoretically accurate.

The current output of each gradient coil is included in table 4.1 to reflect the significance of the power term in the regularisation process. Without the power term (i.e. setting λ_{Power} to 0) the field strength of the gradient coil vanishes. Since a gradient field must produce a unique field strength at each point, to enable spatial encoding of the sample, the role of the gradient coil is clearly negated with a null field. It is important, therefore, to establish that the coil specifications meet certain power requirements.

We now compare the fields produced from the two full length symmetric coils being considered. As the performance of the coils is so similar, figure 4.4 demonstrates the extent to which target field matching has been traded off, in order to produce the minimum noise coil. Figure 4.4 shows the field for the minimum power coil, which is homogeneous to within 5%, and the field for the minimum noise coil, which has a maximum field error of over 55%. As is evident from the diagrams, a strong non-linear field component is present over the target region in figure 4.4(b). The field flattens out around $y = 0$ but importantly still has sufficient strength to encode the imaging region effectively, as is evident from the

reconstructed images in figures 4.8(b), 4.10(b) and 4.11(b) generated by the FBW algorithm [31].

More time was spent searching for optimum regularisation parameters in the asymmetric case. Two of the best illustrative designs found are presented in figure 4.9. The noise reduction associated with Design 1 (seen in 4.9(a)) is 13 dB larger than that of Design 2 (figure 4.9(b)); however, the winding patterns for Design 1 are clearly more complex than Design 2. The choice of the λ parameters was directed towards noise reduction for Design 1, whereas the λ emphasis was directed more towards the smoothing of the winding patterns in Design 2. The fields produced by both asymmetric coils are similar to that seen in 4.4(b) and table 4.1 indicates Design 2 has a marginally better performance than Design 1. Thus, figure 4.9 displays the trade off between noise reduction and winding smoothness (for slightly better performance). Considering the fact that Design 2 still reduces the noise by 30 dB, this demonstrates that there is a large flexibility to this design approach. Very smooth winding patterns can be found that reduce the noise by 10 - 20 dB, which is anticipated to have a very significant effect on the level of discomfort experienced by patients.

The role that the coil length plays in acoustic noise reduction (refer to figure 4.12) is worth noting. As observed, to reduce noise, sections of the coil must contain dense opposing windings. For a shorter coil, there simply is much less available space for the dense opposing windings to fit. Thus, the noise reduction for a shorter coil will not be as large, which is confirmed in figure 4.12. The performance (refer to table 4.1) of the symmetric half length coil is appreciably worse than that of the full length minimum noise coil. The reduced performance is a result of reduced efficiency for the shorter coil, due to the extreme (more so than the full length of coil) dense opposing winding. Thus, the degradation in

noise reduction is compounded with poorer performance for shorter coil designs.

Imaging in the presence of non-linear fields may lead to peripheral nerve stimulation (PNS) [88], with the gradient field potentially becoming dangerously large towards the edges of the chamber. The field produced by the minimum noise coil, seen in figure 4.4(b), shows that the gradient field is clearly steeper towards the outer limits of the chamber than the relatively constant 100 mT/m gradient of the minimum power coil. This may become an issue if the patient is moving when the coils are being switched. Quantitative calculations of gradient strength switching are beyond the scope of this thesis but from an engineering perspective should be considered as a priority to ensure that the quiet coils designed produce minimal PNS. The effects of the non-linear fields are to lessen the gradient field strength in the inner regions of the chamber, which may also detrimentally affect image resolution.

All presented coils have theoretical efficiency and inductance values that would be acceptable for practical purposes. The performance of each coil is thus more or less typical of today's modern standard gradient coils; refer to Zhang *et al.* [118] and While *et al.* [115].

This is a theoretical feasibility study. We do not have the facilities for manufacturing. A construction and rigorous testing phase was not completed due to the limited resources available. However, designs following the work in this thesis at a later date may verify the simulated results predicted. The large simulated amperage required (refer to table 4.1) would be difficult to produce even with the best amplifiers today. Another downside of the winding patterns designed is the aforementioned compactness of the windings. A gradient coil consists of current flowing through grooves of cross-sectional area approximately 2 mm x 2 mm ettched into a primary and sheild copper sheet. A groove linking each winding

is essential to allow current to flow from winding to winding, hence each current distribution forms a sprial of grooves carved into the copper sheets of defined radius. This step is discussed in detail in Peeren [92] and illustrates the practical issues between a simulated continuously distributed current winding and a manufactured coil to be used in clinical imaging procedures. Current flowing in the same direction is neccesarily connected to similarly designed portions of the coil. The aforementioned tightly wrapped nature of the acoustically optimised winding patterns is likely to make construction difficult and even mapping the grooves required on the copper sheet might become an advanced design task.

4.5 Conclusion

We have presented a robust method for reducing the simulated acoustic noise output by a gradient coil in a whole body MRI application. Using a Tikhonov regularisation process to design coil windings, the noise is reduced significantly by minimizing the coil's deflection in the radial direction. An unavoidable result of this is the non-linearity of the field produced inside the imaging region. This non-linearity, however, is mitigated by an image processing technique described in Forbes *et al.* [31] and discussed here in relation to the new coil designs presented.

Further encouraging signs were obtained by a consideration of the inductance and efficiency values obtained for the coil designs. These L and η values lie within the acceptable range for modern gradient coils (see Zhang *et al.* [118]) despite involving designs that generate dense windings in localised areas. Intuitively, it is to be expected that the shorter coils offer less option for noise reduction, since they effectively have a lower capacity to reduce coil distortion through repeated winding sections containing opposing currents. This was confirmed in this study.

In future work the methods of this chapter should be available to optimise gradient coil designs, focussing on a variety of performance criteria, rather than considering the field linearity in isolation. Requiring the field to be linear to within 5% is very restrictive; however, as demonstrated here, it is possible to relax the rigidity of this requirement while still obtaining useful simulated images, and it is easy to imagine clinical protocols that might require a known phantom to be imaged routinely, so that these alternative coil designs can be exploited. This may offer gradient coil engineers more flexibility to design devices that incorporate key aspects of patient comfort.

Chapter 5

Summary and Conclusions

This thesis has been devoted to the advancement of a theoretical design for quiet gradient coils. This is an important field of research since the effects of large noise amplitude can cause discomfort and hearing impairment to patients and nearby personnel. Larger noises are becoming more and more of an issue for MRI engineers as modern scanners are built with increasingly larger field strengths; see Jing-Huei *et al.* [61].

The method developed is based on Tikhonov regularisation and successfully accounts for the ill-conditioned inverse problem of determining windings that produce a specified linear field. The method involves selecting appropriate penalty constraints, such as an integrated coil deflection term in company with other terms to reduce noise levels and sufficiently condition the ill-posed system. Applications of the described method are broad and cover gradient models where the length and width can change, the switching frequency ranges, and whether the coil is shielded or not, among other variations.

This thesis has been ordered accordingly to represent the logical extensions added

to each model. A description of the fundamental concepts behind MRI was presented in chapter 1. This chapter started with a short historical account of the events that led to the development of MRI, then moved onto a discussion of the physical principles involved, a look at basic coil winding patterns, and finally a brief description as to the role of key hardware components, with particular emphasis placed on the gradient coils. The problem of large noise generated by the gradient coils is discussed (along with surrounding issues) and the importance of reducing these effects becomes clear. The first chapter is intended to acquaint the reader with the necessary background information required to understand the more significant contributions of this thesis.

Chapters 2, 3, and 4 constitute a substantial part of the original work developed throughout the doctoral research program. Firstly, in chapter 2, a simple model is put forward that illustrates the problem of pro-active acoustic noise reduction. The main difficulty to overcome is that of determining the winding pattern on a gradient coil that produces a linear field leads to an ill-conditioned system. This is achieved using Tikhonov regularisation with a high degree of success. The natural penalty function that minimises the deformation of the chamber in order to reduce the simulated acoustic noise is adopted, as well as winding smoothing penalty functions, and together they combine adequately to ensure an accurate solution of the ill-conditioned system. Genuine periodic switching of the gradient coils is considered along with associated resonance effects. The importance of the switching function and associated switching frequency with respect to noise output is highlighted. Comparatively small noise reductions of 0.6 dB were achieved, yet this simple model forms a solid base to build upon.

A natural extension to the model presented in chapter 2 is the consideration of a full three dimensional coil deformation model and finite length pressure wave.

These expansions are considered explicitly in chapter 3 in detail. The approach of designing the gradient winding patterns is analogous to that of chapter 2; however, the emphasis of chapter 3 is placed on the effects of the coil distorting in the azimuthal and longitudinal directions as well as the consequences of the open end boundary conditions on the pressure wave. Considerably more complex mathematical and computational techniques were required to solve the three dimensional deflection and finite length pressure wave problems. Ultimately, however, the effects of a three dimensional deformation model and finite length pressure wave were found to be insignificant for a range of parameters, thus confirming the model in chapter 2 as acceptable. Reductions in noise were of similar magnitude to that of the model in chapter 2, but important insight was gained by considering a more complete gradient coil model.

Lastly, a robust technique for dramatically reducing the simulated acoustic noise output is presented in chapter 4. It was found that significant reductions in noise were achievable only by sacrificing field linearity. Thus, in the Tikhonov regularisation process, the regularisation parameters were chosen primarily to reduce the deflection of the coil (and hence acoustic noise) at the expense of replicating the target field. The resulting nonlinearities of the magnetic field are typically detrimental to the acquired image; however, use of the FBW algorithm restores clarity (especially over the central part) to the image successfully. Applications of the resulting method were to the one-dimensional model presented in chapter 2, which was confirmed as satisfactory from the work detailed in chapter 3. Somewhat extreme examples of field nonlinearity were considered, and the method was shown to be capable of reducing the simulated acoustic noise and recovering good images. Reductions up to 49 dB in simulated acoustic noise were obtained and the trade off between field linearity, winding smoothness, and noise reduction was

demonstrated.

More research into the scope of designs that the FBW algorithm allows needs to be undertaken as mentioned in the concluding remarks of chapter 4. Gradient coils that are no longer required to produce a linear field have the potential to accomplish many desirable design features simultaneously such as reducing power and inductance, minimizing peripheral nerve stimulation, and lowering heat generated, for example.

The gradient coil is given a simple structural design and may not replicate a modern clinical coil to a high degree of accuracy, however, under the geometry used (refer to figure 2.1) complete analytical solutions for the coil's deflection components and acoutsic noise output were obtained. It is believed that more complex coil models will require numerical methods for computing SPL's produced from a vibrating gradient coil. Analytical solutions were obtained from derived equations which encompass both electromagnetic and mechanical aspects of an MRI scanner. As previously justified, the most siginficant body force acting on a gradient coil is the Lorentz force and other elastic properties of the gradient coil have been incorporated neatly into the deflection modelling. The model we have used to simulate our gradient coil appears to have an unavoidable problem of producing loud acoustic noise. The field strength we have assumed the primary magnet to have (2 T), along with an acoustically optimised current distribution that produces a transverse gradient of respectable strength, together, produce a Lorentz force of sufficient magnitude to distort the chamber enough to generate a large amplitdue pressure wave. This leads to loud acoustic noise and without using image processing techniques to enable the linearity of the gradient field to be sacrificed becomes a problem.

Limitations to the designs produced in chapter 4 may become evident in the

manufacturing stage. The dense reverse winding sights may need to be diminished somewhat in order to facilitate construction. In addition, localised Lorentz forces resulting from dense reverse windings, which have been ignored, may become significant and add (in some areas) to the deformation of the coil and therefore the acoustic noise. The solutions derived entail a delicate balance of (in our case four) regularisation parameters to achieve extreme noise reductions. Unfortunately there is no way around this time consuming manual experimentation stage in the design process.

A rigorous experimental testing of the coils designed will need to be undertaken to confirm the theory presented. Nevertheless, the method presented in chapter 4 accomplishes the goal of reducing the simulated acoustic noise output spectacularly. The robustness of the developed method allows a wide design range of gradient coils to be engineered, that force the acoustic noise output to be well below the threshold of pain. It is envisaged that this work will contribute to the advancement of knowledge of quiet gradient coils and noise simulation.

Appendix A

Deriving the Open End Boundary Condition

A.1 Formulating the Boundary Problem

In this section, an extensive derivation of the open end boundary condition for the pressure perturbation (equation (3.11)) presented in chapter 3 is given. Concerns for brevity and conciseness forced a complete justification to be omitted from the body of the thesis. The problem is to derive an appropriate boundary condition for the pressure wave reaching the open (air) boundary of the chamber (at $r = a$, $z = \pm L$). This allows us to determine how much of the pressure wave is reflected, and how much acoustic noise the reflected wave contributes to the interior of the chamber. Refer to figure A.1 for a geometrical description of our assumed end effect condition.

The boundary condition for a semi-infinite duct with axial symmetric flow is considered in detail here. Assuming the geometrical model seen in figure A.1,

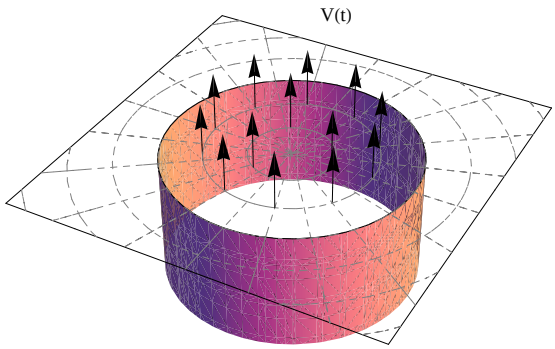

Figure A.1: A depiction of our assumed axial-symmetric flow ($V(t)$) out of a semi-infinite duct with an infinite baffle.

we formulate the problem by using linearised acoustic theory. Starting with the linearised form of the conservation of momentum and mass equations, and the isentropic gas equation we have

$$\begin{aligned}
&\frac{\partial v_r}{\partial t} + \frac{1}{\rho_0}\frac{\partial p_{A1}}{\partial r} = 0, \\
&\frac{\partial v_z}{\partial t} + \frac{1}{\rho_0}\frac{\partial p_{A1}}{\partial z} = 0, \\
&\frac{\partial \rho_{A1}}{\partial t} + \rho_0\left(\frac{\partial v_r}{\partial r} + \frac{v_r}{r} + \frac{\partial v_z}{\partial z}\right) = 0, \\
&p_{A1} = c_{A0}^2 \rho_1,
\end{aligned} \tag{A.1}$$

where v_r and v_z are small air speeds induced from the coil deflection components u_r and u_z.

Our axi-symmetric half plane model (seen in figure A.1) has the following mathematical formulation.

On $z = 0$,

$$v_z = \begin{cases} 0, & r > a \\ V(t), & r < a \end{cases}, \tag{A.2}$$

and at $z = \infty$,

$$p_{A1} = 0, \quad v_r = 0, \quad v_z = 0.$$

Rearranging and combining the linearised conservation equations (A.1) in terms of the pressure perturbation, p_{A1}, we get the axi-symmetric wave equation

$$\frac{\partial^2 p_{A1}}{\partial t^2} = c_{A0}^2 \left(\frac{\partial^2 p_{A1}}{\partial r^2} + \frac{1}{r}\frac{\partial p_{A1}}{\partial r} + \frac{\partial^2 p_{A1}}{\partial z^2} \right). \tag{A.3}$$

Now we consider the Hankel transform of order 0. Let the Hankel transform of order 0 of $f(r)$ be denoted by $F_0(k)$, and defined by

$$\widehat{F}_0(k) = \int_0^\infty r f(r) J_0(kr) dr,$$
$$\text{so} \qquad \widehat{P}_{A1_0}(k, z, t) = \int_0^\infty r p_{A1}(r, z, t) J_0(kr) dr.$$

Taking the axi-symmetric wave equation (A.3), and multiplying it by $rJ_0(kr)$ and integrating with respect to r on both sides (this is equivalent to taking the Hankel transform of order 0 of the problem), we obtain

$$\frac{\partial^2 \widehat{P}_{A1_0}}{\partial t^2} = c_{A0}^2 \left(-k^2 \widehat{P}_{A1_0} + \frac{\partial^2 \widehat{P}_{A1_0}}{\partial z^2} \right), \tag{A.4}$$

after applying some simplifications using Bessel function identities found in Abramowitz and Stegun [1].

Next, we denote the Laplace transform in time of $f(t)$ as $\overline{F}(s)$, with the following standard definition

$$\begin{aligned} & \overline{F}(s) = \int_0^\infty f(t)e^{-st}dt, \\ \text{giving} \qquad & \overline{\widehat{P}}_{A1_0}(k,z,s) = \int_0^\infty \widehat{P}_{A1_0}(k,z,t)e^{-st}dt, \\ \text{and therefore} \qquad & \overline{\widehat{P}}_{A1_0}(k,z,s) = \int_0^\infty \int_0^\infty r p_{A1}(r,z,t)J_0(kr)dre^{-st}dt. \end{aligned}$$

Taking the Laplace transform (in time) of the Hankel transformed wave equation (A.4) gives

$$s^2\overline{\widehat{P}}_{A1_0} - s\widehat{P}_{A1_0}\Big|_{t=0} - \frac{\partial \widehat{P}_{A1_0}}{\partial t}\Big|_{t=0} = c_{A0}^2\left(-k^2\overline{\widehat{P}}_{A1_0} + \frac{\partial^2\overline{\widehat{P}}_{A1_0}}{\partial z^2}\right).$$

Our results are calculated at a time significantly far along so that we can ignore initial effects. Hence we can assume the pressure wave starts off so that $\widehat{P}_{A1_0}\Big|_{t=0} = \partial\widehat{P}_{A1_0}/\partial t\Big|_{t=0} = 0$, which allows us to simplify the above equation. Finally, the twice transformed wave equation becomes

$$s^2\overline{\widehat{P}}_{A1_0} = c_{A0}^2\left(-k^2\overline{\widehat{P}}_{A1_0} + \frac{\partial^2\overline{\widehat{P}}_{A1_0}}{\partial z^2}\right)$$

which is rearranged to give

$$\frac{\partial^2\overline{\widehat{P}}_{A1_0}}{\partial z^2} = \left(\frac{s^2 + c_{A0}^2k^2}{c_{A0}^2}\right)\overline{\widehat{P}}_{A1_0}. \tag{A.5}$$

We require solutions that vanish as $z \to \infty$; hence, the solution to the ordinary differential equation (A.5) becomes

$$\overline{\widehat{P}}_{A1_0}(k,z,s) = A(k,s)e^{\left(-z\frac{s^2+c_{A0}^2k^2}{c_{A0}^2}\right)}, \quad \text{for } z > 0. \tag{A.6}$$

This is the general form of the twice transformed pressure perturbation, p_{A1}.

In order to solve for the coefficient, $A(k,s)$, we need an expression for the twice transformed boundary condition, on $z = 0$. Using the z-component of the momentum conservation expression we get

$$\frac{\partial p_{A1}}{\partial z} = -\rho_{A0}\frac{\partial v_z}{\partial t}, \quad \text{for } z \geq 0,$$

and applying our boundary condition equation (A.2) gives

$$\left.\frac{\partial p_{A1}}{\partial z}\right|_{z=0} = \begin{cases} 0, & r > a \\ -\rho_0 V'(t), & r < a \end{cases},$$

which is our boundary condition on $z = 0$ in terms of the pressure perturbation. Taking the Hankel transform of order 0 (as previously) of the above expression we get

$$\int_0^\infty r \left.\frac{\partial p_{A1}}{\partial z}\right|_{z=0} J_0(kr)dr = -\rho_{A0}V'(t)\int_0^a rJ_0(kr)dr$$

which results in

$$\frac{\partial \widehat{P}_{A1_0}}{\partial z}(k,0,t) = -\rho_{A0}V'(t)\frac{a}{k}J_1(ka),$$

after evaluating the Bessel integral on the right hand side in closed form. Similarly, as before, we next take the Laplace transform in time of the above equation involving $\widehat{P}_{A1_0}(k,0,t)$. Assuming $V(0) = 0$, and defining $\overline{V}(s) = \int_0^\infty V(t)e^{-st}dt$,

we get

$$\begin{aligned}
&\frac{\partial}{\partial z}\int_0^\infty \widehat{P}_{A1_0}(k,0,t)e^{-st}dt = -\rho_{A0}\frac{a}{k}J_1(ka)\int_0^\infty V'(t)e^{-st}dt \\
\Rightarrow\quad &\left.\frac{\partial\overline{\widehat{P}}_{A1_0}}{\partial z}\right|_{z=0} = -\rho_{A0}\frac{a}{k}J_1(ka)\left(\left[V(t)e^{-st}\right]_{t=0}^\infty + s\int_0^\infty V(t)e^{-st}dt\right) \\
\Rightarrow\quad &\left.\frac{\partial\overline{\widehat{P}}_{A1_0}}{\partial z}\right|_{z=0} = -\rho_{A0}\frac{a}{k}J_1(ka)s\overline{V}(s). \qquad \text{(A.7)}
\end{aligned}$$

Applying boundary condition (A.7) to equation (A.6), we determine the coefficient $A(k,s)$ to be

$$A(k,s) = \rho_{A0}c_{A0}\frac{a}{k}J_1(ka)\frac{s\overline{V}(s)}{\sqrt{s^2+c_{A0}^2k^2}}.$$

So, our final expression for the twice transformed pressure perturbation is

$$\overline{\widehat{P}}_{A1_0}(k,z,s) = \rho_{A0}c_{A0}\frac{a}{k}J_1(ka)\overline{V}(s)\frac{s}{\sqrt{s^2+c_{A0}^2k^2}}\ e^{-z\frac{\sqrt{s^2+c_{A0}^2k^2}}{c_{A0}}}. \qquad \text{(A.8)}$$

Thus, we have found the solution of the twice transformed pressure wave. To find the pressure perturbation on $r = a$, $z = 0$, the inverse Laplace transform and inverse Hankel transform must be applied in successive order.

A.2 Inverting the Transformed Pressure Wave

This is a difficult problem. The complicated nature of the twice transformed pressure perturbation, (A.8), makes inverting the expression hard to compute in closed form. However, we are only interested in evaluating the pressure at the open ends of the chamber, which in our model is the plane $z = 0$. Looking solely

at the plane $z = 0$, in (A.8) we get

$$\overline{\widehat{P}}_{A1_0}(k, 0, s) = \rho_{A0} c_{A0} \frac{a}{k} J_1(ka) s\overline{V}(s) \frac{1}{\sqrt{s^2 + c_{A0}^2 k^2}}.$$

We begin by using the inverse Laplace transform. From Gradshteyn and Ryzhik [42] we use the known result $\ell\{J_0(c_{A0}kt)\} = 1/\sqrt{s^2 + c_{A0}^2 k^2}$, which allows us to write

$$\ell\left\{\overline{\widehat{P}}_{A1_0}(k, 0, s)\right\} = \rho_{A0} c_{A0} \frac{a}{k} J_1(ka) \ell\left\{\overline{V}'(t)\right\} \ell\{J_0(c_{A0}kt)\}.$$

So, we can take the inverse Laplace transform by using the Convolution Theorem. We can now write the Hankel transform of our solution to the pressure wave as

$$\widehat{P}_{A1_0}(k, 0, t) = \rho_{A0} c_{A0} \frac{a}{k} J_1(ka) \int_0^t V'(\tau) J_0(c_{A0}k(t - \tau)) d\tau.$$

Finally, we invert the Hankel transform to get

$$\begin{aligned} & p_{A1}(r, 0, t) = \rho_{A0} c_{A0} \int_0^\infty \frac{a}{k} k J_1(ka) \int_0^t V'(t) J_0(c_{A0}k(t - \tau)) d\tau J_0(kr) dk \\ \Rightarrow \quad & p_{A1}(r, 0, t) = \rho_{A0} c_{A0} a \int_0^\infty V'(\tau) \int_0^\infty J_1(ka) J_0(kr) J_0(c_{A0}k(t - \tau)) dk d\tau. \end{aligned}$$

The expression for p_{A1} given, above, is the boundary condition that we enforce at the open air boundary of the coil, on $r = a$, $z = 0$. Thus, we evaluate $p_{A1}(r, 0, t)$ at $r = a$ to obtain,

$$p_{A1}(a, 0, t) = \rho_{A0} c_{A0} a \int_0^\infty V'(\tau) \int_0^\infty J_1(ka) J_0(ka) J_0(c_{A0}k(t - \tau)) dk d\tau. \quad \text{(A.9)}$$

We now take equation (A.9), and evaluate the integrals, to obtain a more usable

form for the boundary condition.

A.3 Manipulation of the Boundary Condition

The form of p_{A1}, given in (A.9), is a complicated expression. Using integration formulae from Gradshteyn and Ryzhik [42] we can evaluate the complicated triple Bessel function integral with respect to k using a Weber-Schafheitlin discontinuous integral.

Firstly, we use integration by parts to evaluate the τ-integral. Consider that

$$\int_0^t V'(t)J_0(c_{A0}k(t-\tau))d\tau = V(t) - c_{A0}k\int_0^t V(\tau)J_1(c_{A0}k(t-\tau))d\tau,$$

which leads to

$$\begin{aligned} p_{A1}(a,0,t) &= \rho_{A0}c_{A0}aV(t)\int_0^\infty J_1(ka)J_0(ka)dk \\ &- \rho_{A0}c_{A0}^2 a\int_0^t V(\tau)\int_0^\infty kJ_1(ka)J_0(ka)J_1(c_{A0}k(t-\tau))dkd\tau \\ &= \frac{1}{2}\rho_{A0}c_{A0}V(t) \\ &\quad -\rho_{A0}c_{A0}^2 a\int_0^t V(\tau)\int_0^\infty kJ_1(ka)J_0(ka)J_1(c_{A0}k(t-\tau))dkd\tau \end{aligned} \tag{A.10}$$

Furthermore, Gradshteyn and Ryzhik [42] provide the expression (p.718)

$$\int_0^\infty kJ_0(ka)J_1(ka)J_1(c_{A0}k(t-\tau))dk = \begin{cases} \frac{1}{\sqrt{2\pi}ac_{A0}(t-\tau)}(\sin v)^{-1/2}P_{1/2}^{1/2}(\cos v), & 0 < c_{A0}(t-\tau) < 2a, \\ 0, & c_{A0}(t-\tau) > 2a, \end{cases}$$

where $\cos v = c_{A0}(t-\tau)/2a$ and $P_{1/2}^{1/2}(\cos v) = \sqrt{2/\pi}(\sin v)^{-1/2}\cos v$, such that equation (A.10) can be simplified to

$$p_{A1}(a,0,t) = \frac{1}{2}\rho_{A0}c_{A0}V(t) - \rho_{A0}c_{A0}^2 a\int_0^t V(\tau)G(t-\tau)d\tau,$$

$$\text{where} \qquad G(t-\tau) = \begin{cases} \frac{1}{a\pi}\frac{1}{\sqrt{4a^2 - c_{A0}^2(t-\tau)^2}}, & t-\tau < \frac{2a}{c_{A0}} \\ 0, & t-\tau > \frac{2a}{c_{A0}}. \end{cases}$$

After carefully analysing the domain of $G(t-\tau)$, we finally arrive at a split definition for the pressure perturbation on $r = a$, $z = 0$.

$$p_{A1}(a,0,t) = \begin{cases} \frac{1}{2}\rho_{A0}c_{A0}V(t) - \frac{\rho_{A0}c_{A0}^2}{\pi}\int_0^t V(\tau)\frac{1}{\sqrt{4a^2 - c_{A0}^2(t-\tau)^2}}d\tau, \text{ if } t < \frac{2a}{c_{A0}} \\ \frac{1}{2}\rho_{A0}c_{A0}V(t) - \frac{\rho_{A0}c_{A0}^2}{\pi}\int_{t-\frac{2a}{c_{A0}}}^t V(\tau)\frac{1}{\sqrt{4a^2 - c_{A0}^2(t-\tau)^2}}d\tau, \text{ if } t > \frac{2a}{c_{A0}}. \end{cases}$$

This allows us to determine how much of the pressure wave has been reflected.

In our case, we only consider the long term effects of the pressure wave. Taking the values $a = 0.3\,\text{m}$ and $c_{A0} = 343\,\text{ms}^{-1}$, our interest is solely in the case $t > 2a/c_{A0}$. Thus, the applied boundary condition we use is

$$p_{A1}(a,0,t) = \frac{1}{2}\rho_{A0}c_{A0}V(t) - \frac{\rho_{A0}c_{A0}^2}{\pi}\int_{t-\frac{2a}{c_{A0}}}^t V(\tau)\frac{1}{\sqrt{4a^2 - c_{A0}^2(t-\tau)^2}}d\tau,$$

for large t.

Appendix B

Electromagnetic Theory

The study of electromagnetism (EM) underpins the physics behind the NMR process. A brief overview of basic EM theory will be given in this section; however, the reader is directed to texts such as Jackson [56] for an extensive coverage of this topic. Starting with Maxwell's equations, we have

$$\nabla \cdot \mathbf{D} = \rho \qquad \text{(Gauss' Law)} \tag{B.1}$$

$$\nabla \cdot \mathbf{B} = 0 \qquad \text{(no magnetic monopoles)} \tag{B.2}$$

$$\nabla \times \mathbf{E} = -\frac{\partial \mathbf{B}}{\partial t} \qquad \text{(Faraday's Law)} \tag{B.3}$$

$$\nabla \times \mathbf{H} = \mathbf{J} + \frac{\partial \mathbf{D}}{\partial t} \qquad \text{(Ampere's Law).} \tag{B.4}$$

Taking the divergence of Ampere's Law and substituting it into Gauss's Law we obtain the Continuity equation

$$\frac{\partial \rho}{\partial t} + \nabla \cdot \mathbf{J} = 0. \tag{B.5}$$

The relationship between electric field vector terms (i.e. terms relating to bound

and unbound charge), and the magnetic field vector terms (i.e. terms relating to bound and unbound current) are given by

$$\mathbf{D} = \epsilon_0 \mathbf{E} + \mathbf{P} \quad (= \epsilon \mathbf{E}), \tag{B.6}$$

$$\mathbf{H} = \frac{1}{\mu_0}\mathbf{B} - \mathbf{M} \quad \left(= \frac{\mathbf{B}}{\mu}\right), \tag{B.7}$$

where ϵ_0 is the relative permittivity of free space and μ_0 is the relative permeability of free space.

B.1 Derivation of the Biot - Savart Law

The Biot - Savart Law is used to compute the magnetic induction field, $\mathbf{B}$, at any point in space given a current density, $\mathbf{J}$. Starting from Maxwell's equations (B.3,B.4) in a source free, time independent form, we have

$$\nabla \cdot \mathbf{B} = \mathbf{0}, \tag{B.8}$$

$$\nabla \times \mathbf{B} = \mu_0 \mathbf{J}. \tag{B.9}$$

Equation (B.8) allows us to define a vector potential, $\mathbf{A}$, for $\mathbf{B}$, where

$$\mathbf{B} = \nabla \times \mathbf{A}. \tag{B.10}$$

Upon using the appropriate form of the vector triple cross product, we can substitute (B.10) into equation (B.9) and get

$$\nabla (\nabla \cdot \mathbf{A}) - \nabla^2 \mathbf{A} = \mu_0 \mathbf{J}. \tag{B.11}$$

We have specified the *curl* of $\mathbf{A}$; however, we are still free to choose its divergence. In order to simplify (B.11) we simply take a Coulomb gauge (see Jackson [56]) where

$$\begin{aligned} & \nabla \cdot \mathbf{A} = 0 \\ \Rightarrow \quad & \nabla^2 \mathbf{A} = -\mu_0 \mathbf{J}. \end{aligned} \tag{B.12}$$

Equation (B.12) is known to be the vector Poisson equation, which has a well known solution (see Stratton [101]) of the form

$$\mathbf{A}(\mathbf{r}) = \frac{4\pi}{\mu_0} \int \int \int_V \frac{\mathbf{J}(\mathbf{r}')}{R} dV',$$

where $R = || \mathbf{r}' - \mathbf{r} ||$, and a 'dash' denotes a source variable. To find the magnetic field produced from the vector potential $\mathbf{A}$, we apply (B.10) and get

$$\mathbf{B}(\mathbf{r}) = \nabla \times \mathbf{A}(\mathbf{r}) = \frac{\mu_0}{4\pi} \int \int_S \nabla \times \left(\frac{\mathbf{J}}{R} \right) dS',$$

in which $\mathbf{J}$ is a surface current density which is typically most appropriate for MRI use. Using Stokes Theorem, we can write the Biot - Savart Law in its common form using a line current, I, as

$$\mathbf{B} = \frac{\mu_0 I}{4\pi} \int \frac{d\mathbf{l}' \times \mathbf{R}}{R^3}.$$

BIBLIOGRAPHY

[1] M. Abramowitz and I. Stegun. *Handbook of Mathematical Functions*. Dover Publications, Inc., 1965.

[2] D. Alsop and T. Connick. Optimisation of Torque Balanced Asymmetric Head J Gradient Coils. *Magn Reson Med*, 35:875–88, 1996.

[3] W. Anderson. Apparatus for Improving the Homogeneity of a Magnetic Field. Patent, 1965. Patent number: 3199021.

[4] M. Bernstein, X. Zhou, J. Polzin, K. King, A. Ganin, N. Pelc, and G. Glover. Concomitant Gradient Terms in Phase Contrast MR: Analysis and Correction. *Magn Reson Med*, 39:300–8, 1998.

[5] M. Bersntein, K. King, and X. Zhou. *Handbook of MRI Pulse Sequences*. Elsevier Academic Press, 2004.

[6] D. Bies and C. Hansen. *Engineering Noise Control: Theory and Practise*. Taylor and Francis, 2009.

[7] M. Blaimer, F. Breuer, M. Mueller, R. Heidemann, M. Griswold, and P. Jakob. SMASH, SENSE, PILS, GRAPPA: How to choose the Optimal Method. *Topics Magn Reson Imaging*, 15:223–36, 2004.

[8] F. Bloch, W. Hansen, and M. Packard. Nuclear Induction. *Phys Rev*, 69:127, 1946.

[9] A. Boresi and K. Chong. *Elasticity in Engineering Mechanics*. Elsevier, 1987.

[10] R. Bowtell and A. Peters. Analytic Approach to the Design of Transverse Gradient Coils with Co-axial Return Paths. *Magn Reson Med*, 41:600–8, 1999.

[11] M. Brideson, L. Forbes, and S. Crozier. Determining Complicated Winding Patterns for Shim Coils Using Stream Functions and the Target-Field Method. *Concepts Magn Reson B Magn Reson Eng*, 14:9–18, 2002.

[12] M. Brown and R. Semelka. *MRI: Basic Principles and Applications*. Wiley-Blackwell, 4th edition, 2010.

[13] P. Callaghan. *Principles of Nuclear Magnetic Resonance Microscopy*. Oxford University Press, 1991.

[14] M. Carley. Series Expansion for the Sound Field of a Ring Source. *J Acoust Soc Am*, 128(6):1–6, 2010.

[15] J. Carlson, K. Derby, K. Hawryszko, and M. Weideman. Design and Evaluation of Shielded Gradient Coils. *Magn Reson Med*, 26:191–206, 1992.

[16] H. Carr. Steady-State Free Precession in Nuclear Magnetic Resonance. *Phys Rev*, 112(5):1693–1701, 1958.

[17] H. Carr and E. Purcell. Effects of Diffusion on Free Precession in Nuclear Magnetic Resonance Experiments. *Phys Rev*, 94(3):630–8, 1954.

[18] B. Chapman and P. Mansfield. Quiet Gradient Coils: Active Acoustically and Magnetically Screened Distributed Transverse Gradient Designs. *Meas Sci Technol*, 6:349–54, 1995.

[19] B. Chronik and B. Rutt. Constrained Length Minimum Inductance Gradient Coil Design. *Magn Reson Med*, 39:270–8, 1998.

[20] K. Coyne. MRI: A Guided Tour. http://www.magnet.fsu.edu/... education/tutorials/magnetacademy/mri/fullarticle.html, 1995.

[21] R. Damadian. Apparatus and Method for Detecting Cancer in Tissue. Patent, 1972. Patent number: 3789832.

[22] L. Delves and J. Mohamed. *Computatioal Methods for Integral Equations*. Cambriage Univ. Press, 1985.

[23] W. Edelstein, T. Kidane, V. Taracila, T. Baig, T. Eagan, Y. Cheng, R. Brown, and J. Mallick. Active-Passive Gradient Shielding for MRI Acoustic Noise Reduction. *Magn Reson Med*, 53:1013–7, 2005.

[24] H. Eggers, T. Knopp, and D. Potts. Field Inhomogeneity Correction Based on Gridding Reconstruction for Magnetic Resonance Imaging. *IEEE T Med Imaging*, 26(3):374–84, 2007.

[25] R. Eisberg and R. Resnick. *Quantum Physics of Atoms, Molecules, Solids, Nuclei, and Particles*. John Wiley & Sons, Inc., 2nd edition, 1985.

[26] R. Ernst. Two Dimensional Gyromagnetic Resonance Spectroscopy. Patent, 1977. Patent number: 4045723.

[27] A. Filler. The History, Development and Impact of Computed Imaging in Neurological Diagnosis and Neurosurgery: CT, MRI, and DTI. *Nature Precedings*, 5:1–69, 2009.

[28] D. Fishbain, M. Goldberg, and E. Labbe. Long-Term Claustrophobia Following MRI. *Am J Phys*, 145:1038–9, 1988.

[29] B. Fisher, N. Dillion, T. Carpenter, and L. Hall. Design by Genetic Algorithm of a Z - Gradient set for Magnetic Resonance-Imaging of the Human Brain. *Meas Sci Technol*, 6(7):904–9, 1995.

[30] L. Forbes, M. Brideson, S. Crozier, and P. While. An Analytical Approach to the Design of Quiet Cylindrical Asymmetrical Gradient Coils in MRI. *Concepts Magn Reson B Magn Reson Eng*, 31B(4):218–36, 2007.

[31] L. Forbes, M. Brideson, and P. While. A Theoretical Method for the Use of a Phantom to Enhance Image Construction in MRI. *Concepts Magn Reson B Magn Reson Eng*, 39B(2):98–108, 2011.

[32] L. Forbes and S. Crozier. A Novel Target-Field Method for Finite-Length Magnetic Resonance Shim Coils, Part 1: Zonal Shims. *J Phys D Appl Phys*, 34:3447–55, 2001.

[33] L. Forbes and S. Crozier. A Novel Target-Field Method for Finite-Length Magnetic Resonance Shim Coils, Part 2: Tesseral Shims. *J Phys D Appl Phys*, 35:839–49, 2002.

[34] L. Forbes and S. Crozier. A Novel Target-Field Method for Finite-Length Magnetic Resonance Shim Coils, Part 3: Shielded Zonal and Tesseral Coils. *J Phys D Appl Phys*, 36:68–80, 2003.

[35] D. Gadian. *NMR and its Applications to Living Systems*. Oxford University Press, 2nd edition, 1995.

[36] M. Garrett. Axially Symmetric Systems for Generating and Measuring Magnetic Fields. Part 1. *J Appl Phys*, 22(9):1091–107, 1951.

[37] A. Garroway, P. Grannell, and P. Mansfield. Image Formation using Nuclear Magnetic Resonance. Patent, 1977. Patent number: 4021726.

[38] P. Glover. Interaction of MRI Field Gradients with the Human Body. *Phys Med Biol*, 54:R99–115, 2009.

[39] M. Golay. Feild Homogenizing Coils for Nuclear Spin Resonance Instrumentation. *Rev Sci Instrum*, 29(4):313–5, 1958.

[40] M. Golay. Field Homogenization for a Reference Sample in a Lock-On Nuclear Magnetic Resonance Apparatus. Patent, 1970. Patent number: 3510832.

[41] M. Golay. Magnetic Field Control Apparatus. Patent, 1970. Patent number: 3515979.

[42] I. Gradshteyn and I. Ryzhik. *Table of Integrals, Series, and Products*. Academic Press, 6th edition, 2000.

[43] G. Grant and R. Harris. *Encylopedia of Nuclear Magnetic Resonance*, volume 1. John Wiley and Sons, 1996.

[44] J. Gunter, M. Bernstein, B. Borowski, C. Ward, P. Britson, J. Felmlee, N. Schuff, M. Weiner, and C. Jack. Measurement of MRI Scanner Performance with the ADNI Phantom. *Med Phys*, 36:2193–205, 2009.

[45] E. Haacke, R. Brown, M. Thompson, and R. Venkatesan. *Magnetic Resonance Imaging: Physical Principles and Sequence Design*. Wiley-Liss, 1st edition, 1999.

[46] J. Hadamard. *Lectures on Cauchy's Problem in Linear Partial Differential Equations*. Yale University Press, 1932.

[47] R. Hashemi, W. Bradley Jr, and C. Lisanti. *MRI The Basics*. Lippincott Williams and Wilkins, 2nd edition, 2004.

[48] C. Hayes. The Development of the Birdcage Resonator: A Historical Perspective. *NMR Biomed*, 22:908–18, 2009.

[49] J. Hennig, A. Welz, G. Schultz, J. Krovink, Z. Liu, O. Speck, and M. Zaitsev. Parallel Imaging in Non-Bijective, Curvilinear Magnetic Field Gradients: A Concept Study. *Magn Reson Mater Phy*, 21(1):5–14, 2008.

[50] S. Hidalgo-Tobon. Theory of Gradient Coil Design Methods for Magnetic Resonance Imaging. *Concept Magn Reson A*, 36A:223–42, 2010.

[51] H. Hill and R. Richards. Limits of Measurement in Magnetic Resonance. *J Phys E*, 2(1):977–83, 1968.

[52] J. Hornak. *The Basics of MRI*. Interactive Learning Software, 1996.

[53] D. Hoult. *The Application of High Field Nuclear Magnetic Resonance*. PhD thesis, Oxford University, 1973.

[54] M. Ichiki, R. Syma, and I. Young. A Micromechanical Expanding Coil Mechanism for *in vivo* Magnetic Resonance Imaging. *J Micromech Microeng*, 15:771–7, 2005.

[55] D. Idiyatullin, C. Corum, J.-Y. Park, and M. Garwood. Fast and Quiet MRI using a Swept Radiofrequency. *J Magn Reson*, 181:342–9, 2006.

[56] J. Jackson. *Classical Electrodynamics*. John Wiley & Sons, Inc., 3rd edition, 1999.

[57] J. Jackson, M. Brideson, L. Forbes, and S. Crozier. Tikhonov Regularization Approach to Acoutsic Noise Reduction in an Asymmetric, Self-Shielded

MRI Gradient Coil. *Concepts Magn Reson B Magn Reson Eng*, 37B(3):167–79, 2010.

[58] J. Jackson, L. Forbes, P. While, and M. Brideson. Could Image Processing Enable Reduced Acoustic Noise during MRI Scans? *Concepts Magn Reson B Magn Reson Eng*, 39B:191–205, 2011.

[59] A. Janke, H. Zhao, G. Cowin, G. Galloway, and D. Doddrell. Use of Spherical Harmonic Deconvolution Methods to compensate for Nonlinear Gradient Effects on MRI Images. *Magn Reson Med*, 53:115–22, 2004.

[60] J. Jin. *Electromagnetic Analysis and Design in Magnetic Resonance Imaging.* CRC Press, 1st edition, 1999.

[61] L. Jing-Huei, B. Rudd, L. Mingfeng, and T. Lim. Sound Reduction Techniques for MRI. *Recent Pat Eng*, 2:72–9, 2008.

[62] E. Kreyszig. *Advanced Engineering Mathematics.* John Wiley & Sons, Inc., 8th edition, 1999.

[63] A. Kuijpers, S. Rienstra, G. Verbeek, and J. Verheij. The Acoustic Radiation of Baffled Finite Ducts with Vibrating Walls. *J Sound Vib*, 216(3):461–93, 1998.

[64] V. Kuperman. *Magnetic Resoance Imaging: Physical Principles and Applications.* Academic Press, 2000.

[65] S. Labros, M. Petropoulos, and A. Morich. Novel Gradient Coil Set with Canceled Net Thrust Force for Nuclear Magnetic Resonance Applications. *IEEE T Magn*, 31:3536–59, 1995.

[66] S. Langlois, M. Designes, J. Constans, and M. Revenu. MRI Geometric Distortion: A Simple Approach to Correcting the Effects of Non-linear Gradient Fields. *J Magn Reson Imaging*, 9:821–31, 1999.

[67] J. Larmor. On the Theory of the Magnetic Influence on Spectra; and on the Radiation from Moving Ions. *Philos Mag Series 5*, 44(271):503–12, 1897.

[68] P. Lauterbur. Image Formation by Induced Local Interactions: Examples Employing Nuclear Magnetic Resonance. *Nature*, 242:190–1, 1973.

[69] M. Levitt. *Spin Dynamics: Basics of Nuclear Magnetic Resonance*. John Wiley & Sons, Ltd, 2nd edition, 2001.

[70] G. Li and C. Mechefske. Structural-acoustic Modal Analysis of Cylindrical Shells: Application to MRI Scanner Systems. *Magn Reson Mater Phy*, 22:353–64, 2009.

[71] Z. Liang and P. Lauterbur. *Principles of Magnetic Imaging: A Signal Processing Perspective*. IEEE Press, 2000.

[72] T. Lin, P. O'Shea, and C. Mechefse. Reducing MRI Gradient Coil Vibration with Rib Stiffners. *Concepts Magn Reson B Magn Reson Eng*, 35(B):198–209, 2009.

[73] G. Liu and X. Han. *Computational Inverse Techniques in Nondestructive Evaluation*. CRC Press, 2003.

[74] P. Mansfield and B. Chapman. Active Magnetic Screening of Coils for Static and Time-Dependant Magnetic Field Generation in NMR Imaging. *J Phys E Sci Instrum*, 19(7):540–5, 1986.

[75] P. Mansfield and B. Chapman. Active Magnetized Screening of Gradient Coils in NMR Imaging. *J Magn Reson*, 66:573–6, 1986.

[76] P. Mansfield, B. Chapman, R. Bowtell, P. Glover, R. Coxon, and P. Harvey. Active Acoustic Screening: Reduction of Noise in Gradient Coils by Lorentz Force Balancing. *Magn Reson Med*, 33:276–81, 1995.

[77] P. Mansfield, P. Glover, and R. Bowtell. Active Acoustic Screening: Design Principles for Quiet Gradient Coils in MRI. *Meas Sci Technol*, 5:1021–5, 1994.

[78] P. Mansfield and P. Grannell. NMR Diffraction in Solids. *J Phys C Solid State*, 6:L422–7, 1973.

[79] P. Mansfield, B. Haywood, and R. Coxon. Active Acoustic Control in Gdraient Coils for MRI. *Magn Reson Med*, 46:807–11, 2001.

[80] P. Mansfield and P. Morris. *NMR Imaging in Biomedicine*. Academic Press, 1982.

[81] L. McKeehan. Combinations of Circular Currents for Producing Uniform Magnetic Fields. *Rev Sci Instrum*, 7:150–2, 1936.

[82] L. McKeehan. Combinations of Circular Currents for Producing Uniform Magnetic Fields. *Rev Sci Instrum*, 7:178–9, 1936.

[83] D. McRobbie, E. Moore, M. Graves, and M. Prince. *MRI: From Picture to Proton*. Cambridge University Press, 2003.

[84] C. Mechefske and W. Li. Spatial Measurements and Estimation of Acoustic Noise in a 4T MRI Scanner. *IJAV*, 9(2):69–74, 2004.

[85] C. Mechefske and F. Wang. Theoretical, Numerical, and Experimental Modal Analysis of a Single-Winding Gradient Coil Insert Cylinder. *Magn Reson Mater Phy*, 19:152–66, 2006.

[86] C. Mechefske, Y. Wu, and B. Rutt. MRI Gradient Coil Cylinder Sound Field Simulation and Measurement. *J Biomed Eng*, 124:1–6, 2002.

[87] C. Mechefske, G. Yao, W. Li, C. Gazdzinski, and B. Rutt. Model Analysis and Acoustic Noise Characterization of a 4 T MRI Gradient Coil Insert. *Concepts Magn Reson B Magn Reson Eng*, 22B:37–49, 2004.

[88] National Health and Medical Research Council. *Safety Guidelines for Magnetic Resonance Diagnosis Facilities*, 34th edition, 1991. Radiation Health Series.

[89] P. Neittaanmaki, M. Rudnicki, and A. Savini. *Inverse Problems and Optimal Design in Electricity and Magnetism*. Clarendon Press, 1996.

[90] F. Nelson. Means and Apparatus for Improving the Homogeneity of Magnetic Fields. Patent, 1958. Patent number: 2858504.

[91] M. NessAiver. *All you really need to know About MRI Physics*. Simply Physics, 1996.

[92] G. Peeren. Stream Function Approach for determining Optimal Surface Currents. *J Comput Phys*, 191:305–21, 2003.

[93] S. Pissanetzky. Minimum Energy MRI Gradient Coils of General Geometry. *Meas Sci Technol*, 3(7):667–73, 1992.

[94] E. Purcell, H. Torrey, and P. Pound. Resonance Absorption by Nuclear Magnetic Moments in a Solid. *Phys Rev*, 69:37–8, 1946.

[95] I. Rabi, S. Millman, and P. Kusch. The Molecular Beam Resonance Method for Measuring Nuclear Magnetic Moments. The Magnetic Moments of $_3\mathrm{Li}^6$, $_3\mathrm{Li}^7$, and $_9\mathrm{F}^{19}$. *Phys Rev*, 55:526–35, 1939.

[96] J. Rigden. Quantum States and Precession: The Two Discoveries of NMR. *Rev Mod Phys*, 58(2):433–48, 1986.

[97] F. Romeo and D. Hoult. Magnet Field Profiling: Analysis and Correcting Coil Design. *Magn Reson Med*, 1(1):44–65, 1984.

[98] W. Shao and C. Mechefske. Acoustic Analysis of a Finite Cylindrical Duct based on Green's Functions. *J Sound Vib*, 285:979–88, 2005.

[99] E. Shaw. Design and Construction of an Electromagnet for investigation of the Magnetic Properties of Atoms and Molecules. *Rev Sci Instrum*, 2:611–7, 1931.

[100] J. Stockmann, P. Ciris, G. Galiana, L. Tam, and R. Constable. *O*-space Imaging: Highly Efficient Parallel Imaging using Second-Order Nonlinear Fields as Encoding Gradients with no Phase Encoding. *Magn Reson Med*, 64(2):447–56, 2010.

[101] J. Stratton. *Electromagnetic Theory*. McGraw-Hill Book Company, Inc., 1941.

[102] B. Thaller. *The Dirac Equation*. Springer - Verlag, 1992.

[103] Q. Tieng and V. Vegh. Magnetic Resonance Imaging in Nonlinear Fields with Nonlinear Reconstruction. *Concepts Magn Reson B Magn Reson Eng*, 38(B):128–40, 2011.

[104] A. Tikhonov. Regularization of Incorrectly Posed Problems. *Soviet Mathematical Dolk*, 4:1624–7, 1963.

[105] A. Tikhonov. Solutions of Incorrectly Formulated Problems and the Regularization Method. *Soviet Mathematical Dolk*, 4:1035–8, 1963.

[106] R. Turner. A Target Field Approach to Optimal Coil Design. *J Phys D Appl Phys*, 19:L147–51, 1986.

[107] R. Turner. Minimum Inductance Coils. *J Phys E Sci Instrum*, 21:948–52, 1988.

[108] R. Turner. Gradient Coil Design: A Review of Methods. *Magn Reson Imaging*, 11:903–20, 1993.

[109] M. Vlaardingerbroek and J. den Boer. *Magnetic Resonance Imaging Theory and Practice*. Springer, 3rd edition, 1996.

[110] D. Wang, D. Doddrell, and G. Cowin. A Novel Phantom and Method for Comprehensive 3-Dimensional Measurement and Correction of Geometric Distortion in Magnetic Resonance Imaging. *Magn Reson Imaging*, 22:529–42, 2004.

[111] F. Wang and C. Mechefske. Dynamic Analysis of a Multi-layered Gradient Coil Insert in a 4 T MRI Scanner. *Concepts Magn Reson B Magn Reson Eng*, 31:237–54, 2007.

[112] F. Wang and C. Mechefske. Vibration Analysis of a Thin-Walled Gradient Coil Model. *J Sound Vib*, 311:554–66, 2008.

[113] H. Weinstock and T. Erber. Training of Brakhausen Emission in Nickel and Iron. *J Appl Phys*, 63(8):3952–4, 1988.

[114] P. While, L. Forbes, and S. Crozier. A Time-Harmonic Target-Field Method for Designing Unshielded RF Coils in MRI. *Meas Sci Technol*, 16:997–1006, 2005.

[115] P. While, L. Forbes, and S. Crozier. Designing Gradient Coils with Reduced Hot Spot Temperatures. *J Magn Reson*, 203:91–9, 2009.

[116] G. Yao, C. Mechefske, and B. Rutt. Characterization of Vibration and Acoustic Noise in a Gradient-Coil Insert. *Magn Reson Mater Phys*, 17:12–27, 2004.

[117] G. Yao, C. Mechefske, and B. Rutt. Vibration Analysis and Measurement of a Gradient Coil Insert in a 4 T MRI. *J Sound Vib*, 285:743–58, 2005.

[118] B. Zhang, C. Gazdzinski, B. Chronik, H. Xu, S. Conolly, and B. Rutt. Simple Design Guidelines for Short MRI Systems. *Concepts Magn Reson B Magn Reson Eng*, 25B:53–9, 2005.

[119] S. Zhang and J. Jin. *Computation of Special Functions*. John Wiley & Sons Inc, 1996.

[120] W. Zorumski. Generalized Radiation Impedances and Reflection Coefficients of Circular and Annular Ducts. *J Acoust Soc Am*, 54(6):1667–73, 1973.